

Design and Development of Flight Controller for Kite-based Wind Power Generation Systems

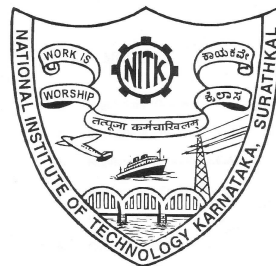
Thesis

Submitted in partial fulfillment of the requirement for the award of the degree of

DOCTOR OF PHILOSOPHY

by

ROYSTAN VIJAY CASTELINO



DEPARTMENT OF ELECTRICAL AND ELECTRONICS ENGINEERING
NATIONAL INSTITUTE OF TECHNOLOGY KARNATAKA
SRINIVASNAGAR, MANGALORE - 575025

JANUARY, 2024

DECLARATION

by the Ph.D. Research Scholar

I hereby *declare* that the Research Thesis entitled “**Design and Development of Flight Controller for Kite-based Wind Power Generation Systems**” which is being submitted to the **National Institute of Technology Karnataka, Surathkal** in partial fulfillment of the requirement for the award of the Degree of **Doctor of Philosophy in Electrical and Electronics Engineering** is a *bonafide report of the research work carried out by me*. The material in this Research Thesis has not been submitted to any University or Institution for the award of any degree.



.....
ROYSTAN VIJAY CASTELINO, 187045
Department of Electrical and Electronics Engineering

Place: NITK-Surathkal
Date: January 08, 2024

CERTIFICATE

by the Ph.D. Research Scholar

This is to *certify* that the Research Thesis entitled "**Design and Development of Flight Controller for Kite-based Wind Power Generation Systems**" submitted by **Roystan Vijay Castelino** (Register Number: 187045) as the record of the research work carried out by him, is *accepted as the Research Thesis submission* in partial fulfillment of the requirements for the award of degree of **Doctor of Philosophy**.



Dr Yashwant Kashyap
(Research Guide)



Dr. Dattatraya Narayan Gaonkar
(Chairman-DRPC, EEE dept.)

PROFESSOR AND HEAD

**DEPARTMENT OF ELECTRICAL AND ELECTRONICS ENGINEERING
NATIONAL INSTITUTE OF TECHNOLOGY KARNATAKA
SRINIVASNAGAR, SURATHKAL, MANGALORE - 575 025, INDIA**

Acknowledgments

It gives me immense pleasure and great satisfaction to express my heartfelt gratitude to those who made this dissertation possible.

Firstly, I thank *almighty God* for always giving me strength.

I want to express my sincere gratitude to *Dr. Yashwant Kashyap* for his guidance, unending support, and encouragement and for having been my Ph.D. supervisor. He has been a constant source of inspiration throughout this journey. I feel proud to have worked under his guidance.

I thank *National Institute of Technology Karnataka, Surathkal (NITK)* for allowing me to do research and *Ministry of Human Resource Department, Government of India* for awarding a research scholarship.

I thank my research progress assessment committee (RPAC) members, *Dr. Manjunatha Sharma K* and *Dr Sandeep Kumar*, for their constructive feedback and guidance.

Thanks also go to former HODs, *Prof. B Venkatesa Perumal, Prof. Shubhanga K N, Prof. Gururaj S Punekar*, and HOD, *Dr. Dattatraya Narayan Gaonkar*, for providing the necessary resources in the department to carry out my research.

I want to extend my deepest gratitude to my mother, father, and brothers for their love and patience, which kept me on this journey. Their faith and unconditional love towards me are the reason for my achievements.

Finally, I would like to thank my brothers, Roshan and Rohith who have been with me from the beginning of this process. Thank you for your support and guidance throughout my work.

Roystan Vijay Castelino

Abstract

Wind power can significantly contribute to transitioning from fossil fuels to renewable energies. Airborne Wind Energy (AWE) technology is one of the approaches to tapping the power of high-altitude wind. Kite Power System (KPS) is a type of AWE technology which uses tethered kites to harness the power in the wind at higher altitudes. The main advantage of KPS over Conventional Wind Turbines (CWT) is that the KPS eliminates the need for a structure and rotating blades, significantly reducing the size and materials needed. Also, kites can reach much higher altitudes than CWT, which can harness the power from much stronger winds. The study of the dynamics of KPS is fundamental in researching and developing a commercial-scale system. Unlike CWTs, where the blades rotate in a circular motion, the kites are controlled to follow figure-eight trajectories in the crosswinds. The kites harness power from the wind and transfer the aerodynamic force through the tethers to the ground. The reeling-out tether rotates the generator at the ground station to generate electric power. As the tether length is finite, the kite is depowered and reeled in at the end of the limit by consuming a fraction of generated power. The cycle of operation repeats and is called as pumping cycle kite power system. KPS is one of the solutions contributing towards clean and green energy production in the renewable energy mix, which is the sole motivation of this research work. The KPS has challenges that must be addressed to develop it as a commercially viable product.

The power from the kites depends on the tether force of the kite in the figure-eight trajectory. The tether force of a kite depends on the wind velocity and the kite's orientation to the wind vector in the figure-eight trajectory. This research presents an experimental measurement of the pulling force of an Airush Lithium 12 m² kite with a constant tether length of 24 m in a coastal region. The position and orientation data of the kite is obtained from the sensors mounted on the kite. The flight dynamics of the kite are studied using multiple field tests under steady and turbulent wind conditions. In this research, a physical model (PM), Artificial Neural Network (ANN) and Long Short-Term Memory (LSTM) deep neural network algorithms are proposed to estimate the tether force of the kite with experimental validation. The performance of the proposed methods is studied using Root Mean Square Error (RMSE), Mean Absolute Error (MAE), and R^2 evaluation methods.

The potential of KPS can be realized by scaling the model to a commercial-scale power generation device. Testing an actual KAWECS or a location with suitable wind conditions is only sometimes a trusted opportunity for conducting research. A KAWECS emulator is developed based on a Permanent Magnet Synchronous Machine (PMSM) drive coupled with a generator to mimic the kite's behaviour in wind conditions. The KPS is simulated using a MATLAB-SIMULINK environment with various power ranges and wind conditions. The satellite wind speed data at 10 m and 50 m above ground with field data of the kite's figure-

of-eight trajectories are used to emulate the kite's characteristics in the dynamic wind conditions.

Another challenge in the KPS is the steering controller, which controls and flies a kite in figure-eight crosswind motion. The kite consists of two power lines and two control lines, the power lines are connected together, and the kite delivers most of the force through the power lines. The left and right control lines are used to steer the kite by a differential movement of both lines. The kite steer controller mimics the differential movement of the kite control lines to steer the kite. The force exerted on the control lines by the kite is essential in designing the kite steering actuators. A kite steering controller's design and development methodology is explained and validated using experimental analysis under steady and turbulent wind conditions. The power consumed to control the kite and the power generation aspects of the KPS is also analyzed. The results of this research will promote the use of KAWECS as it can provide reliable and seamless energy flow, enriching wind energy exploitation under various installation environments.

Contents

Acknowledgements	i
Abstract	iii
List of Figures	vii
List of Tables	xiii
List of Abbreviations	xv
List of Symbols	xvi
1 Introduction	1
1.1 Background	1
1.2 Kite-based Wind Power Generation	2
1.3 Literature Survey	3
1.3.1 Estimation of Tether Force	4
1.3.2 Application of Machine Learning	4
1.3.3 Simulation of Kite Power System	4
1.3.4 Kite Steer Controller	5
1.4 Motivation for the Work	6
1.5 Problem Statement	6
1.6 Identified Research Gaps	7
1.7 Research Objectives	7
1.8 Outline of the Thesis	7
2 Kite Tether Force Estimation	9
2.1 Introduction	9
2.2 Problem Description	10
2.2.1 Kite Constraints	10
2.2.2 Kite Dynamics	12
2.2.3 Kite Field Test Conditions	12
2.3 Tether Force Estimation Methods	13
2.3.1 Wind Window and Crosswind Power	13
2.3.2 Kite Kinematics and Aerodynamic Force	13
2.3.3 Experimental Setup	14
2.3.3.1 Kite Telemetry System	16
2.3.3.2 On-Air Kite Unit	18
2.3.3.3 On-Ground Kite Unit	19
2.3.3.4 Force Measurement Unit	19

2.3.3.5	Field Data Collection	19
2.3.4	Kite Tether Force Estimation	20
2.3.4.1	Kite Inclination Effects	21
2.3.4.2	Kite Tether Force Estimation using Physical Model (PM)	23
2.3.4.3	Kite Force Estimation Using Deep Neural Networks	24
2.3.4.4	Artificial Neural Network (ANN)	24
2.3.4.5	Long Short-Term Memory (LSTM)	25
2.4	Results	26
2.4.1	PM Simulation Results	26
2.4.2	Tether Force Validation	28
2.4.2.1	Physical Model (PM) Validation	29
2.4.2.2	Artificial Neural Network (ANN) Model Validation	29
2.4.2.3	Long Short-Term Memory (LSTM) Model Validation	30
2.4.2.4	Comparison and Validations of Models	31
	2.4.2.4.1 RMSE Method:	32
	2.4.2.4.2 MAE Method:	32
	2.4.2.4.3 R^2 Method:	33
2.5	Summary	35
3	Simulation of Kite Power System	37
3.1	Introduction	37
3.2	KPS Emulator Modelling	38
3.2.1	Kite Dynamics	38
3.2.2	PMSM Modelling	42
3.2.3	Simulation Model	44
3.2.4	Emulator Model	45
3.2.5	Comparison with Conventional Wind Turbine	47
3.3	Simulation Results and Discussion	48
3.3.1	No-load Test	49
3.3.2	On-load Test	49
3.3.3	Field Test Data Analysis	53
3.3.4	Simulation using the satellite data	54
3.3.5	Verification using experimental data	57
3.3.6	Discussion and Applications	59
3.4	Summary	59
4	Design of Kite Steer Controller	61
4.1	Introduction	61
4.2	Modelling and Control of the Kite	62
4.2.1	Kite Dynamics	62
4.2.2	Kite control method	65
4.2.3	Design of Kite Steer Controller (KSC)	66
4.2.4	Design of Position Controlled Actuators	67
4.3	Method of the kite Steer Controller	67
4.3.1	Roll Pitch Zone (RPZ) Control Method	69

4.3.2	Implementation of the KSC	72
4.3.3	Field Test and Data Analysis	74
4.4	Results and discussions	75
4.4.1	Manual Kite Control Test	76
4.4.2	RPZ Control Experimental Validation	79
4.4.3	Comparative Analysis	83
4.4.4	Power simulation results	83
4.5	Summary	85
5	Conclusion and Future Scope	87
5.1	Conclusion	87
5.2	Contributions	88
5.3	Future Scope of Work	89
	Bibliography	91
	Publications based on the thesis	102

List of Figures

1.1	Kite power generation technique: kite travels in a figure-eight trajectory, which pulls the tether wound on the drum and rotates the generator to produce electric power	3
2.1	Kite’s position and orientation represented in the spherical coordinate system and the forces experienced by the kite [Oehler and Schmehl, 2019]. (a) Kite’s orientation and position. (b) Angle of attack of the kite.	11
2.2	Wind window: an imaginary boundary in which the kite can be flown to produce power; the red area indicates the maximum power zone, the yellow area shows the moderate power zone, and the green area indicates the low power zone.	13
2.3	Kite reference frame [van der Vlugt et al., 2019]: The left figure shows the position of the kite at point K in a three-dimensional plane with the forces acting on the kite. The right figure shows the orientation of the kite in terms of the Euler form.	14
2.4	Experimental setup: (a) pictorial representation of the system used for estimating the tether force with a block diagram of the system, (b) Actual experimental setup used in the experimental tests.	15
2.5	Airush Lithium 12 m ² Kite.	16
2.6	Sensor system on the kite: (a) block diagram of the system, (b) PCB implementation of the sensor system, (c) PCB enclosed within the box for protection, (d) Sensor system installed on the kite using velcro.	17
2.7	Sensor system on the ground: (a) Block diagram of the kite data receiver system on the ground, (b) Implementation of the sensor data receiver circuit in the PCB, (c) Back side of the PCB with LCD, (d) Wind speed and direction sensors at the testing site.	18
2.8	Measurement of tether force using lad-cell, (a) shows the pictorial representation of the setup, (b) shows the actual setup mounted on the wooden board in which the tether is passed through the pulleys.	20

2.9	Wind window with shaded area indicating area swept by the kite in the figure-eight trajectory (ϕ degrees); W_{de} represents the wind direction vector; K represents kite tether vector; N, E, and S are the north, east, and south reference vectors; χ is the angle between east and W_{de} ; ψ is the angle between east and the kite tether vector; β is the angle between W_{de} and the kite tether vector.	21
2.10	The figure-eight trajectory followed by the kite during the test. The GPS and altitude data were used to plot the trajectory of the kite in 3 dimensions. (a) Top view: lat vs. lon. (b) 3D view: lat-lon vs. altitude. (c) Side view: lat vs. altitude. (d) Yaw vs. Force. (e) Roll vs. Force. (f) Pitch vs. Force.	22
2.11	Simulation of tether force in MATLAB SIMULINK: (a) From left, the data from the field test are given as a numeric matrix and the kite's data block filters the data to calculate the lift and drag forces; the force-simulated block calculates the tether force. (b) Shows a plot of the lift force vs. drag force from the simulated tether force.	23
2.12	The flow of the estimation of the tether force using the DNN methods: The field test data were imported to the models and then normalised so that they could be used in the ANN and LSTM models; the predicted data in the normalised form were then inverted to the actual values; the performance was evaluated using the RMSE, MAE, and R^2 methods.	24
2.13	The basic architecture of the ANN: the input layer is fed with the kite's orientation data on altitude and wind speed; there are four hidden layers between the input and output and the output of the ANN was the tether force (F_t).	25
2.14	The basic structure of a Long Short-Term Memory (LSTM) unit: X_t is the current input; h_{t-1} is the last output; C_{t-1} is the memory from the last LSTM unit; h_t is the current output; C_t is the next cell state; 'b' is the bias; ' σ ' block is a sigmoid layer; ' \tanh ' block is a tanh layer; ' \times ' and '+' are the scaling and addition operators, respectively.	26
2.15	Tether force simulation for three test cases: (a-c) polar plots of the YRP vs. force; the sweep represents the angles (0° to 360°) and the magnitude represents the tether force, (d-f) time-series plots of the YRP and the tether force under the steady wind conditions.	27
2.16	Tether force simulation for three test cases: (a-c) polar plots of the YRP vs. force; the sweep represents the angles (0° to 360°) and the magnitude represents the tether force, (d-f) time-series plots of the YRP and the tether force under turbulent wind conditions.	28
2.17	Validation of the physical model with the experimental data: (a-c) steady wind conditions, (d-f) turbulent wind conditions.	29

2.18	Experimental validation of predicted tether force from ANN: (a–c) test results for steady wind conditions, (d–f) test results for turbulent wind conditions.	30
2.19	LSTM model test results comparison with the experimental data: (a–c) steady wind condition data for the three tests, (d–f) turbulent wind condition data for the three tests.	31
2.20	Combined analysis of tether force estimation methods–physical, ANN, and LSTM methods: (a–c) the three tests under steady wind conditions, (d–f) the three tests under turbulent wind conditions.	32
2.21	Scatter plots of the physical, ANN, and LSTM models: (a–c) the performance of the models under steady wind conditions, (d–f) the performance of the models under turbulent wind conditions.	33
2.22	Performance analysis of PM, ANN, and LSTM models under steady wind conditions: (a) RMSE method, (b) MAE method, (c) R^2 method.	34
2.23	Performance analysis of PM, ANN, and LSTM models under turbulent wind conditions: (a) RMSE method, (b) MAE method, (c) R^2 method.	34
3.1	Block diagram of a kite power generation system.	38
3.2	Spherical coordinate and geometrically decomposition of the kite system: Fig.(a) shows, the force and speed representations are geometrically comparable. Fig.(b) shows the decomposing kite velocity into radial and tangential components.	39
3.3	Interaction of drum and the kite tether.	41
3.4	Equivalent electrical circuit of PMSM.	42
3.5	kite conversion system (with gear-ratio and drum) using power converter with PMSM.	43
3.6	Wind speed to the kite force (torque and speed) conversion system in Matlab Simulink.	44
3.7	Flow chart of KPS emulator.	45
3.8	Control mechanism of proposed KPS emulator.	46
3.9	Motor speed controller loop.	47
3.10	Load controller loop.	47
3.11	No load analysis at generator terminal: (a) No load speed of coupled machines, (b) No load generator voltage, and (c) No load generator voltage(zoomed view).	50
3.12	Simulation result: (a) Motor current, (b) Motor current(zoomed view),	50
3.12	Simulation result: (c) Electrical power of the motor, (d) Couplings torque, (e) Couplings power, (f) Generator torque, (g) Generator AC current, (h) Generator AC voltage.	51
3.12	Simulation result: (i) Generator output power.	52
3.13	Electrical power output at the generator terminal of three different test cases: (a) 1 kW, (b) 10 kW, and (c) 100 kW	53

3.14	Polar plot of kite flight path test (a) Yaw vs. Force. (b) Roll vs. Force. (c) Pitch vs. Force. Adopted from [Castelino et al., 2022]	54
3.15	Wind data from satellite: plot (a) shows the wind profile for 12 months at 17:00 IST, at 10 m height, respectively, and plot (b) shows 24 hours of wind profile of August month, at 10 m height. . .	55
3.16	Wind data from satellite: plot (a) shows the wind profile for 12 months at 17:00 IST, at 50 m height, respectively, and plot (b) shows 24 hours of wind profile of August month, at 50 m height. . .	55
3.17	Plots using hourly satellite wind data at 50 m height from the ground: (a) wind speed (b) motor speed, (c) estimated kite power from physical model, and (d) generator electrical power.	56
3.18	Power generation plot from hourly satellite wind data at 10 m height from the ground: (a) wind speed (b) motor speed, (c) estimated kite power from physical model (PM), and (d) generator electrical power.	57
3.19	Simulation using experimental data (a) Wind speed, (b) Motor speed, (c) Measured kite power from a field test, (d) Estimated kite power from the physical model, (e) Coupling/Mechanical power, and (f) Generator electrical power.	58
4.1	The projected position of the kite, 'K' on a half sphere with the radius represented by 'r' with the elevation angle θ and azimuth angle ϕ on a North-East-Down (NED) reference frame. The angle made by the wind velocity vector is denoted as ψ with respect to east. The height of the kite is represented by 'h'.	63
4.2	Kite control method using kite control bar.	65
4.3	Significance of figure-of-eight maneuvers	66
4.4	Block diagram of the proposed kite steer controller system	67
4.5	Position controlled DC motor drive	68
4.6	Range of YPR angles and the orientation of the kite and IMU . . .	68
4.7	Visualization of figure-of-eight trajectory of kite using GPS data . .	69
4.8	Change in the Roll and Pitch values in the figure-of-eight trajectory	70
4.9	Operational diagram of the proposed Roll-Pitch-Zone control method	70
4.10	Flowchart of Roll-Pitch-Zone control method	71
4.11	(a) Pictorial representation of the controller (Top view) (b) Top view of the implemented Kite Steering Mechanism (c) Front view of the mechanism (d) Close view of the carriage mechanism	73
4.12	(a) Pictorial representation of the controller (Side View) (b) Side view of the developed kite controller	74
4.13	(a) Kite used for the field tests (b) Kite steering controller	76
4.14	(a) The figure-of-eight trajectory followed by the kite using latitude and longitude values (b) 3D visualization of the path followed by the kite using the altitude data (c) Tether force, left and right line force with respect to the trajectory of the kite (d) The speed of the kite in the given trajectory.	78

4.15	Kite data in SWC -(a) The figure-of-eight trajectory followed by the kite using GPS data (b) 3D view of the path followed by the kite using GPS & altitude data (c) Tether force, left and right line force with respect to the trajectory of the kite (d) The speed of the kite in the given trajectory.	81
4.16	Kite data in TWC -(a) The figure-of-eight trajectory followed by the kite using GPS data (b) 3D view of the path followed by the kite using GPS & altitude data (c) Tether force, left and right line force with respect to the trajectory of the kite (d) The speed of the kite in the given trajectory.	82
4.17	Comparison of tether tension (a) Data from the methods using in the reference [Rushdi et al., 2020a] & (b) Data from the proposed method.	83
4.18	Comparison of centre line force with control line forces and total aerodynamic force. (a) Steady wind & (b) Turbulent wind conditions	84
4.19	Comparison of power generated by centre line only with the total power generated. (a) Steady wind & (b) Turbulent wind conditions	85
4.20	Power consumed to control the kite: Simulated and experimental value. (a) Steady wind & (b) Turbulent wind conditions	85

List of Tables

2.1	Kite Specifications.	15
2.2	Kite telemetry system: on-air kite unit specifications and on-ground kite unit specifications.	17
2.3	Data logged in the field tests consisting of orientation in quaternion form, altitude, GPS data, load-cell values, wind speed, and wind direction.	20
2.4	Details of the parameters used in the Deep Learning Models—ANN and LSTM:	24
3.1	The KPS emulator parameters of three different test cases	47
3.2	Specifications of KPS and CWT [De Lellis et al., 2016]	49
3.3	Field test data used in the simulation: sample data of 10 data points.	54
4.1	Specifications of the proposed kite steer controller	74
4.2	Data received from the on-air device	75
4.3	Data measured at the ground station and appended with the on-air data	75
4.4	Field test results for the manual control of the kite.	77
4.5	The speed of the kite in the figure-of-eight maneuvers	77
4.6	RPZ controller field test data	79
4.7	The speed of the kite in the figure-of-eight maneuvers in RPZ method	80

List of Abbreviations

AC	Alternating Current
AoA	Angle of Attack
ANN	Artificial Neural Network
AWES	Airborne Wind Energy System
CWT	Conventional Wind Turbine
CI	Confidence Interval
DC	Direct Current
DNN	Deep Neural Network
FOC	Field Oriented Control
GPS	Global Positioning System
HAWT	Horizontal Axis Wind Turbines
IMU	Inertial Measurement Unit
KAWECS	Kite-based Airborne Wind Energy Conversion System
KPS	Kite Power System
KSC	Kite Steer Controller
LCD	Liquid Crystal Display
LEI	Leading Edge Inflatable
LSTM	Long Short Term Memory
MAE	Mean Absolute Error
MCU	Micro Controller Unit
NED	North-East-Down
PCB	Printed Circuit Board
PI	Proportional Integral
PM	Physical Model
PMSM	Permanent Magnet Synchronous Machine
RF	Radio Frequency
RMSE	Root Mean Square Error
RNN	Recurrent Neural Network
RPM	Revolution Per Minute
RPZ	Roll-Pitch-Zone
SLE	Supported Leading Edge
SWC	Steady Wind Condition
TWC	Turbulent Wind Condition
YRP	Yaw, Roll, and Pitch

List of Symbols

K	Position of the kite
O	Origin in the kite reference plane
r	Tether length
θ	Angle between zenith and point K
ϕ	Angle between reference axis and orthogonal projection
C_L	Coefficient of lift
C_D	Coefficient of drag
L	Lift force of the kite
D	Drag force of the kite
S	Projected surface area of the kite
v_k	Wind velocity at the kite level
ρ	Density of air
F	Aerodynamic force of the kite
α	Angle of attack of the kite
Q_w, Q_x, Q_y, Q_z	Orientation of the kite in Quaternions
D	Drag force of the kite
ϕ'	Roll of the kite in terms of Euler angles
θ'	Pitch of the kite in terms of Euler angles
ψ'	Yaw of the kite in terms of Euler angles
ϕ_{RAW}	Raw value of roll of the kite from field test
θ_{RAW}	Raw value of pitch of the kite from field test
ψ_{RAW}	Raw value of yaw of the kite from field test
F_T	Tether force of the kite
X_t	Current input
C_{t-1}	Memory from the last LSTM unit
h_{t-1}	Output of the last LSTM unit
C_t	New updated memory in LSTM
h_t	Current Output from LSTM
σ	Sigmoid layer in LSTM
\tanh	The tanh layer in LSTM
b	Bias in the LSTM network
\times	Vector scaling operator in LSTM
$+$	Vector addition operator in LSTM
F_{actual}	Actual tether force from the field test
$F_{predict}$	Predicted tether force from ML approaches
χ	Course angle
$u_{k,r}$	Radial component of kite velocity
$u_{k,t}$	Tangential component of kite velocity
u_a	Apparent wind velocity
u_w	Wind velocity
u_k	Kite velocity

p	Reeling factor
q	Tangential speed factor
\in	Belongs to
\Re	Real number
C_R	Resultant aerodynamic force
u_r	Reel-out speed
ω_d	Angular velocity of the drum
T_d	Torque of the drum
N_d	Speed of the drum
F_t	Tether force of the kite
P_d	Drum power
R_s	Stator phase resistance
L_s	Synchronous inductance
E_s	EMF of the stator
L_q	Quadrature-axis inductance
L_d	Direct-axis inductance
\vec{v}_s	stator voltage vector
v_{sd}	Direct axis stator voltage
v_{sq}	Quadrature axis stator voltage
\vec{i}_s	Stator current vector
i_{sd}	Direct axis stator current
i_{sq}	Quadrature axis stator current
Φ_{fs}	Stator flux produced by PMSM
$\phi_{f_{sd}}$	Direct axis stator flux
$\phi_{f_{sq}}$	Quadrature axis stator flux
P_e	Electrical power
V_L	Line voltage
I_L	Line current
C_p	Coefficient of power
λ	Tip speed ratio
R	Area swept by a wind turbine
β	Pitch of the blade
T_m	Mechanical torque
P_{cyl}	Cycle power
P_{rout}	Power in reel-out phase
P_{rin}	Power in reel-in phase
F_{left}	Force from the left control line
F_{right}	Force from the right control line
$F_{control}$	Total control line force
F_{centre}	Force from the centre power line
P_{mech}	Mechanical power developed at the generator
P_{motor}	Power rating of the actuation motor
$P_{motor_{max}}$	Peak power rating of the actuation motor

Chapter 1

Introduction

Contents

1.1	Background	1
1.2	Kite-based Wind Power Generation	2
1.3	Literature Survey	3
1.3.1	Estimation of Tether Force	4
1.3.2	Application of Machine Learning	4
1.3.3	Simulation of Kite Power System	4
1.3.4	Kite Steer Controller	5
1.4	Motivation for the Work	6
1.5	Problem Statement	6
1.6	Identified Research Gaps	7
1.7	Research Objectives	7
1.8	Outline of the Thesis	7

The current chapter explains the background of the proposed research and introduces airborne wind power generation systems, working of kite-based wind power systems with state-of-the-art research. The motivation for the research work with a problem statement and identified research gaps in the literature are explained. The research objectives and the organization of the thesis chapters are also listed.

1.1 Background

Renewable energy generation and utilisation are crucial for reducing the impact of burning fossil fuels on the environment. Renewable technologies come with challenges that restrict their adoption. Wind power is one of the solutions for

decarbonising the energy system. Electric power from wind turbines started in the 1880s [Olabi et al., 2021] and since then, these machines have evolved into megawatt-scale energy generators. Horizontal axis wind turbines (HAWTs) are now widely used in the wind power industry [Johansen, 2021]. Due to increasing energy demands, wind turbines are being developed to reach higher altitudes using taller towers, increasing the conversion efficiency and tapping into the stronger and more persistent wind at higher altitudes [Caduff et al., 2012]. The cost for the higher hub height of HAWTs increases tremendously, and the turbine installation becomes more challenging [DeCarolis and Keith, 2006].

Airborne Wind Energy System (AWES) is a high-altitude wind energy conversion system that uses one or more kites, gliders, or horizontal flying turbines that are tethered to a ground station to produce energy [Kolar et al., 2013]. The AWES was made to improve existing technologies by focusing on catching winds at high altitudes and turning them into electricity [Peçanha et al., 2020]. Loyd demonstrated that a tethered wing the size of a C-5A aircraft could generate 6.7 MW of electrical power with a wind speed of 10 m/s, and the generated power is three times more than the conventional wind turbine-generated power [Loyd, 1980a]. Since then, most of the prototypes for airborne wind energy systems are still in the early stages of development [Cherubini et al., 2015]. AWES technology’s improved availability, stability, and reduced prices make it economically viable [Zillmann and Bechtle, 2018]. The autonomous takeoff and flying of a tethered aircraft verify the technological viability of the proposed takeoff approach, allowing for deploying this AWES technology in a small area at a low cost [Fagiano et al., 2017]. Economic analysis at an existing site indicated that AWES costs less to transport and assemble and has a larger potential capacity, resulting in more significant economic advantages [De Lellis et al., 2016]. Consequently, a little increase in the operating altitude of the wind energy system can result in a significant rise in produced power. AWES can access winds at heights between 0.1 km and 2 km [Cherubini et al., 2015, Salari et al., 2015].

1.2 Kite-based Wind Power Generation

The concept of producing electricity from kites dates back more than four decades [Loyd, 1980b]. The kite-based AWES, called Kite Power System (KPS), uses a kite connected to the ground through a rope or tether. The tether is wound on a spool called drum, coupled with the generator. As the kite flies, it generates lift and pulls the tether, which turns the drum to generate electricity. In KPS, the kite is steered to achieve lying eight or figure-of-eight trajectories to generate power [Noom, 2013, Long et al., 2022]. The figure-eight trajectories are preferred over other trajectories as it generates more crosswind power while the tether does not get tangled during the flight [Dief et al., 2018]. The KPS operates in two phases [Fechner, 2016] as shown in figure 1.1. In the power phase, the crosswind figure-of-eight loops generate maximum lift to turn the generator to produce electricity. In the recovery phase, the kite is de-powered and reverted by consuming a fraction

of the generated power [Van Der Vlugt et al., 2013].

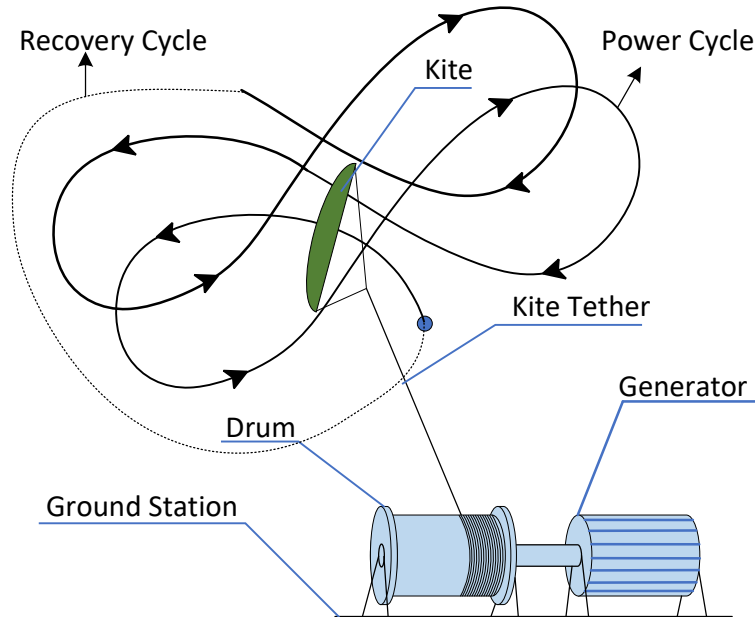


Figure 1.1: Kite power generation technique: kite travels in a figure-eight trajectory, which pulls the tether wound on the drum and rotates the generator to produce electric power

The main advantage of KPS over conventional wind turbines is that it reduces the construction materials by 90 % while accessing the stronger winds at a higher altitude, where conventional wind turbines cannot operate [Lunney et al., 2017]. KPS can have greater energy output and higher efficiency than conventional wind farms [Fechner and Schmehl, 2013, Salma and Schmehl, 2023, Hagen et al., 2023]. Additionally, AWES systems are often lighter, smaller, and more flexible than conventional wind turbines, making them easier to deploy and more suitable for use in remote or challenging locations [Olabi et al., 2021, Tulloch et al., 2023].

1.3 Literature Survey

Airborne Wind Energy Systems (AWES) provide a solution for reaching higher altitudes using fewer materials and lower costs [Meghana et al., 2022]. One of the AWES implementations uses a kite to generate power in pumping cycles [Zolfaghari et al., 2020]. A rigid or soft flying device is attached to a tether of finite length and connected to a drum on the generator [Cherubini et al., 2015]. Energy is generated when the kite pulls the tether, which is called a power generation cycle. When the tether is fully unwound, the kite's inclination angle is reduced and pulled back by consuming a fraction of the power generated in the power generation cycle [Luchsinger, 2013, Duckworth, 1985].

1.3.1 Estimation of Tether Force

Unlike a wind turbine where blades are rotated by the wind to generate power, the kite is flown in crosswind figure-eight manoeuvres, which pull the tether and generate power on the ground. The power generation capabilities of a specific kite at a certain wind velocity can be calculated by estimating the tether force of the kite [Luchsinger, 2013, Burgin and Wilson, 1985]. An analytical model of a kite was first presented by Loyd [Loyd, 1980b] in 1980, providing the fundamentals of kite kinematics. The model assumed the kite and tether to be massless objects to derive a wing's estimated power-generation capabilities. The analytical theory was then refined by Argatov [Argatov et al., 2011] and Terink [Terink et al., 2011] for tethered kites operating at higher altitudes for power generation. The point mass models presented in [Ahmed, 2014, Ruppert, 2012, Akberali et al., 2021] took the kite's mass, velocity, and tether drag into account to estimate the pulling force of a kite. An experimental approach to data collection from kites by towing them was proposed by Rushdi [Rushdi et al., 2020a]. The paper lacked a mathematical or analytical approach to predict the tether force using the collected data. The aerodynamic properties of kites using experimental analysis have been investigated in the literature [Borobia-Moreno et al., 2021] but the data have not been used to estimate the force of kites.

1.3.2 Application of Machine Learning

The nonlinearity in the kite power system makes tether force estimation complex using mathematical models. Deep Neural Networks (DNNs) offer a great solution to nonlinear problems in many applications [LeCun et al., 2015]. Researchers have explored methods for estimating the tether force using regression models [Rushdi et al., 2020b]. The Reinforcement Learning (RL) method has been used [Orzan et al., 2022] to control a tethered kite but there was no explanation for the kite's force. The machine learning-based control of the tethered wings has been discussed in many papers [Fechner, 2016, Dief et al., 2020a] as well as the analytical method for estimating the tether force [Rushdi et al., 2018, van der Vlugt et al., 2019]. However, very few studies contain experimental validation of the methods [Oehler and Schmehl, 2019]. The experimental data-based approach [Baheri and Vermillion, 2017] and system identification approaches [Licitra et al., 2019, Licitra et al., 2017, Dief et al., 2018] have been discussed in the literature, but a comprehensive explanation of the data collection and analysis was not provided. The literature has discussed control techniques for kites but is lacking in predictions of the tether force of kites using machine learning techniques.

1.3.3 Simulation of Kite Power System

An appropriate wind condition or field location for researching an actual KPS is very challenging [Erhard and Strauch, 2015]. Therefore, simulation of airborne wind energy system dynamics and airborne wind energy turbine emulation is convenient. In the literature, most of the KPS use a permanent-magnet synchronous

machine (PMSM) as an electric power generator [Ahmed et al., 2014]. As the KPS operates in pumping cycles, the speed of the generator and the power output is variable and highly dependent on the wind speed. Although there are a lot of Conventional Wind Turbine (CWT) emulations based on PMSM drives [Martinez et al., 2014, Singla et al., 2020, Battaiotto et al., 1996], there is limited literature on the implementation of kite-based emulators. The simulation of power generation using PMSM is explained in the literature but they lack in the discussion related to drum-side mechanical power production [Bagaber et al., 2020, Ahmed et al., 2013, Saberi and Rezaie, 2022] which is crucial in KPS. And also, the study of scaling the power levels using PMSM-based approach is missing in the literature [von den Hoff et al., 2019, Bauer et al., 2016]. The emulated power’s accuracy depends on the kite’s modelling and the data used for the emulation [Ahmed et al., 2013]. Another aspect of the system is scalability which is not discussed in the literature [Ahmed et al., 2013, Bagaber and Mertens, 2021, Bagaber et al., 2022].

1.3.4 Kite Steer Controller

One of the main challenge in the KPS is the autonomous Kite Steer Control (KSC) which is responsible for the steering of the kite [van der Vlugt et al., 2019]. There are two types of KSCs, on-air controller and ground-based controller. The on-air KSC has the motor-actuators and the battery situated near the kite to control the kite. From the on-air controller, a single line connects to the ground station which reduces the number of tethers [Erhard and Strauch, 2012]. On the other hand, the ground-based KSC consists of actuators and batteries which are situated at the ground. In a ground-based KSC, most of the weight is contained at the ground level which makes the system flexible with small kites for the experimental studies [Ahrens et al., 2013]. The ground-based approach can be developed using the available components reducing the cost of the setup, and also it reduces the risk of damage of the controller during kite crashes which increases the reliability. The KSC is an integral part of KPS which is responsible for steering the kite in a predefined path for maximum power extraction [Fechner et al., 2015, Fisscher, 2020]. There are theoretical studies on the design of the KSC [Williams et al., 2008b, Fagiano, 2009] and also the experimental studies [Breukels, 2011, Costello et al., 2017, Castelino et al., 2022] which do not discuss about the force analysis of the control lines. The force on the control lines directly impact the performance of the kite control motors [Erhard and Strauch, 2013, Fechner and Schmehl, 2012]. The power consumed by the control motors should also be taken into account while calculating the net power generated by KPS in a figure-eight cycle.

As the KPS eliminates structure and uses less materials to construct as compared to the conventional wind turbines, it is well suited for offshore floating power generation systems [Fritz, 2013, Fagiano et al., 2010, Coleman et al., 2014]. For the offshore applications, the KSC should be designed to steer the kite in the turbulent winds. There are numerous research paper on control of the tethered kite [Baayen and Ockels, 2012, De Lellis et al., 2013, Zanon et al., 2013, Castro-Fernández et al., 2023] but the research does not explain the controller performance in turbulent

wind conditions. In the turbulent winds, the response of the KSC changes and faster actuation are necessary [Fechner and Schmehl, 2016]. The rapid actuation of the control lines demand more motor power, which has to be taken into consideration in the design of the KSC.

In the literature, a significant amount of research is conducted on the KSC design and theoretical optimization [Williams et al., 2008a, Ilzhöfer et al., 2007, Baayen and Ockels, 2012, Furey and Harvey, 2007, Eijkelhof et al., 2023], yet very few experimental approaches [Lansdorp et al., 2007, Canale et al., 2009, Thedens and Schmehl, 2023, Cayon et al., 2023] have been developed and validated. The experimental approaches fails to justify the power aspect of the KSC and power variations in the figure-eight trajectory [Rushdi et al., 2020a].

1.4 Motivation for the Work

The KPS has significant advantages over conventional Wind Turbines such as accessibility of stronger winds at higher elevation, less material usage, and the KPS can be designed as a mobile power generation system. The mobility of the system facilitates it to be installed in the places where the grid connectivity is unavailable and it can be installed in the remote locations where conventional wind turbine cannot be installed. The main challenges involved in the commercialization of the KPS include - optimization of the KSC, launching and landing method of the kite, and autonomous operation of the system [Khan and Rehan, 2016, Salma et al., 2020, Dief et al., 2020b]. The minimalist structural design and the higher capacity factor of KPS as compared to conventional wind turbines [De Lellis et al., 2016] is the main motivation to the researchers around the world. The commercial viability of KPS depends on the reliable operation of the system and also on the scalability of the system. The direction of this research is towards contribution in the control aspects of the kite and also on the study on the scalability of the system.

1.5 Problem Statement

To design and develop an experimental method to estimate the tether force from the kite and optimization of methods for the estimation of the potential of the kite power system. The scalability of the system needs to be studied using the experimental data by an emulation technique. A kite steering controller has to be developed which can perform in the turbulent wind conditions of the coastal region. Also, simulation of the kite power system for varying wind conditions has to be analysed and the an experimental analysis of power consumed to control the kite has to be developed.

1.6 Identified Research Gaps

From an extensive survey on the state-of-the-art technology in the kite-based wind power generation system, some of the problems are identified which needs to be addressed to make the system viable. The estimation of tether force is vital in designing a KPS. The tether force estimation methods described in the literature is lack experimental validation. Moreover, the mathematical models described in the literature considers approximation of lift and drag coefficients which are not justified. The non-linear behaviour of the system in the steady and turbulent wind conditions can be predicted using machine learning methods. The simulation of system dynamics under dynamic wind conditions are not available in the literature and there is limited literature on the performance of the KPS under electrical loading. The variation of tether force during the figure-eight trajectory is very important to estimate the power production from the system and the power consumed in the trajectory has to be taken into account for the estimation of net power generation capacity of the system. In the literature, there is limited research on the experimental validation of the kite steer controller under varying wind conditions. Moreover, the estimation of forces from the control lines is necessary to design a kite steering actuator mechanism.

1.7 Research Objectives

From the research gaps observed in literature as mentioned in the previous chapter the following are the main objectives of the proposed work:

- Estimation and experimental validation of aerodynamic force of the kite using analytical and machine learning methods.
- Design and simulation of a kite-based electric power generation system using FOC-based PMSM for scaling of the system using MATLAB-Simulink environment.
- Design and development of a ground-based kite steering unit with rapid actuation to study the performance of KPS in varying wind conditions.
- Experimental validation of kite steering system with an analysis on the variation of power in the figure-eight trajectory and the power consumption of the KSC in steady and turbulent wind conditions.

1.8 Outline of the Thesis

The whole thesis is organized into five chapters as follows,

Chapter 1: A brief introduction to Kite-based wind power generation system with extensive literature survey of the force design and simulation models of force estimation, kite control and power generation aspects. The identified research

gaps and research objectives are also discussed in this chapter.

Chapter 2: A methodology to estimate the tether force from the kite with experimental validation is rigorously explained with the design aspects of the system. A physical method (PM) is proposed for the estimation of tether force with a study of application of machine learning algorithms to predict the force from the kite is discussed in this chapter.

Chapter 3: The study of potential of kite-based power generation system using simulation is discussed in this chapter with the experimental verification of the results. The scalability of the system is explained and a comparative analysis of the kite-based systems with the conventional wind turbine is also discussed in this chapter.

Chapter 4: The Design and development aspects of a ground-based kite steer controller with a novel control approach is explained in this chapter. The power consumption of kite steer controller is discussed with the power generation of the system. The testing and validation of the controller in steady and turbulent wind conditions is discussed in this chapter.

Chapter 5: This chapter concludes the contributions of the proposed research work and also discusses the scope for possible future works which can enhance the reliability of kite-based power generators for it to be a commercially viable product.

Chapter 2

Kite Tether Force Estimation

Contents

2.1	Introduction	9
2.2	Problem Description	10
2.2.1	Kite Constraints	10
2.2.2	Kite Dynamics	12
2.2.3	Kite Field Test Conditions	12
2.3	Tether Force Estimation Methods	13
2.3.1	Wind Window and Crosswind Power	13
2.3.2	Kite Kinematics and Aerodynamic Force	13
2.3.3	Experimental Setup	14
2.3.4	Kite Tether Force Estimation	20
2.4	Results	26
2.4.1	PM Simulation Results	26
2.4.2	Tether Force Validation	28
2.5	Summary	35

2.1 Introduction

This chapter presents a design and methodology to estimate the tether force of a KPS using an experimental setup. The estimation of aerodynamic force of the kite is essential for the design and development of a KPS. The proposed approach is based on field data collection, processing, and analysis to obtain the tension of the tether under steady and turbulent wind conditions. Tether force estimation using the Physical Model (PM) of a kite is proposed and is simulated using MATLAB-Simulink. Two machine learning models- ANN and LSTM are trained with the known data from the field tests and the models are tested with unknown data to

predict the tether force. The proposed methods are experimentally validated and the performance of each method is evaluated. Section 2.2 describes the problem description and explains the challenges involved in the experiments. Section 2.3 describes the tether force estimation methods, the attributes of the experimental setup and its operation in detail. Section 2.3 also explains the simulation of tether force using a MATLAB-Simulink environment and the tether force estimation using machine learning techniques. The results are presented in Section 2.4, which includes the results from the flight tests, simulation results, and experimental validation of the simulated tether force. The conclusions and discussion of this research work are presented in the last Section 2.5.

2.2 Problem Description

Estimating the tether force is essential for designing and developing a kite power system. The tether force depends on the kite’s lift coefficient (C_L) and drag coefficient (C_D). The values of C_L and C_D depend on the angle of attack (AoA), which varies with the kite’s flight (orientation) [Ahmed et al., 2011]. The kite’s flight and control are highly nonlinear; hence, modelling the system becomes complicated. In the modelling, assumptions often have to be made to approximate the power output of the system [Bauer et al., 2018]. In many cases, the AoA is assumed to be constant, which makes C_L and C_D constant [Hummel et al., 2019]. In some of the previous studies, the values of C_L and C_D are assumed to be monotonically increasing with the kite’s trajectory but lack experimental validation [Houska and Diehl, 2007]. Hence, a simple and accurate approach must be developed to estimate the tether force in the figure-eight trajectory.

2.2.1 Kite Constraints

Figure 2.1 shows the kite’s position and orientation, as well as the AoA of the kite’s trajectory. Figure 2.1a shows the orientation of the kite in terms of the yaw, roll, and pitch. In the figure, V_x and V_y show the direction of the kite’s travel path and F_T is the tether force measured on the ground. The kite makes an angle with the ground reference called the elevation angle, which is denoted by γ . In the figure-of-eight trajectory, the kite makes an angle with the reference x-axis called a sweep angle, which is denoted by ϕ . F_L denotes the lift force experienced by the kite and the drag force is denoted by F_D . Figure 2.1b shows the AoA of the kite, which is the angle between the kite’s chord line and the relative wind flow. The tether force is measured on the ground, as shown in Figure 2.1b.

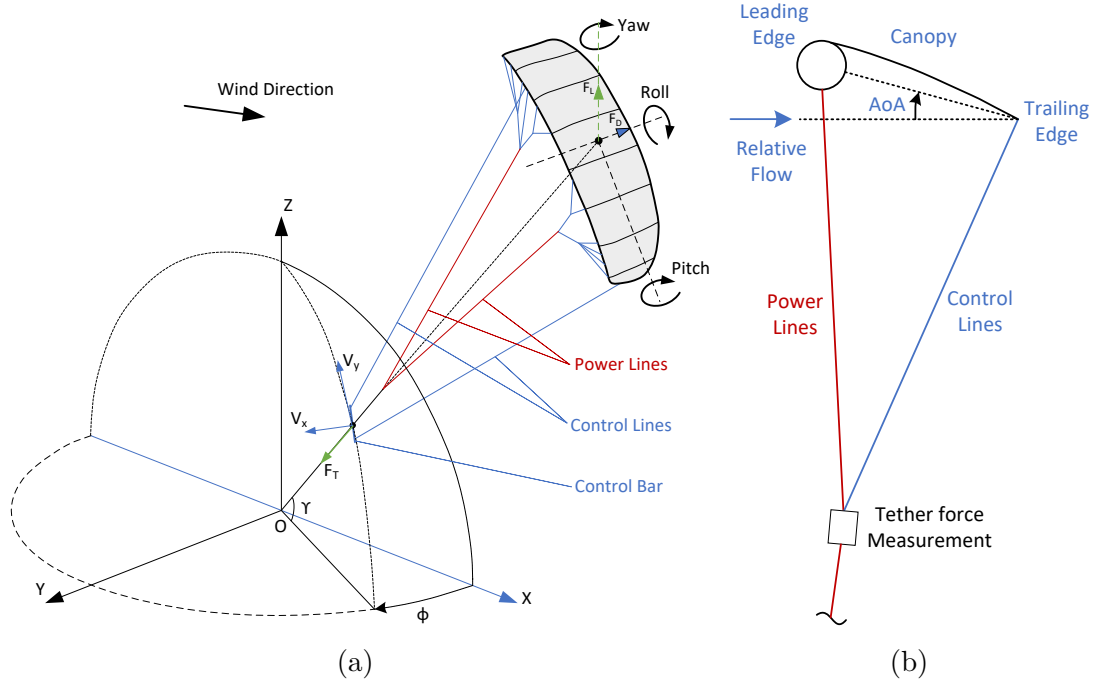


Figure 2.1: Kite's position and orientation represented in the spherical coordinate system and the forces experienced by the kite [Oehler and Schmehl, 2019]. (a) Kite's orientation and position. (b) Angle of attack of the kite.

The lift and drag forces can be estimated by finding the relationship between the kite's orientation and the net aerodynamic force. The orientation of the kite in the Euler form is specified in terms of the yaw, roll, and pitch (YRP) angles, which are related to the measured tether force value from the field tests, to develop the physical model, is proposed. There is a negligible sag in the tether for a short tether line, which is a fixed length of 24 m. Therefore, the elevation angle can be calculated using the kite's altitude.

Hypothesis 1: *The aerodynamic force of a kite can be estimated by knowing the orientation (YRP) of the kite at a particular altitude and wind speed.*

The above hypothesis can be validated using analytical techniques for which the following assumptions are made:

Assumption 1: *The wind speed at the kite is assumed to be the same as the wind speed on the ground for a short tether length.*

Assumption 2: *The kite is manoeuvred at constant speed in the figure-eight pattern.*

Assumption 3: *The effect of tether drag, sag, and gravity on the net aerodynamic*

force is negligible.

Assumption 4: *The tether is assumed to be rigid and straight and the force at the ground station is equal to that at the kite.*

2.2.2 Kite Dynamics

Acquiring accurate orientation data from the kite is challenging. The orientation (YRP) is transmitted to the ground station via wireless communication channels. The measured data should be in quaternions to avoid gimbal lock [Alaimo et al., 2013] and the quaternions are converted to the Euler form for calculating the orientation angles. The yaw angle varies from -180 to $+180$ degrees, the pitch angle varies from -90 to $+90$ degrees, and the roll angle varies from -180 to $+180$ degrees. Inertial measurement sensors are required to determine the absolute orientation using an acceleration sensor, gyroscope, and magnetometer [Castelino and Kashyap, 2021]. The fusion of the acceleration, gyroscope, and magnetometer values provides the orientation. The quaternions are four signed numbers, including a real number Q_w followed by three imaginary values, Q_x , Q_y , and Q_z , representing an object's rotation. The force calculation of the kite model is in a spherical coordinate system that describes the kite's orientation in terms of Euler angles. The orientation of the kite in quaternion form is converted into Euler form using the following formula [Perumal, 2011]:

$$\begin{bmatrix} \phi' \\ \theta' \\ \psi' \end{bmatrix} = \begin{bmatrix} \text{atan2}(2(Q_w Q_x + Q_y Q_z), 1 - 2(Q_x^2 + Q_y^2)) \\ \text{asin}(2(Q_w Q_y + Q_z Q_x)) \\ \text{atan2}(2(Q_w Q_z + Q_x Q_y), 1 - 2(Q_y^2 + Q_z^2)) \end{bmatrix} \quad (2.1)$$

where ϕ' is the roll of the kite, θ' is the pitch of the kite, and ψ' is the yaw angle of the kite, which are applied in this order [Karduna et al., 2000]. The notation of the YRP angles depends on the sensor (IMU) placement on the kite. In this experiment, the pitch and roll values are interchanged by 90 degrees clockwise according to the sensor placement. Therefore, the pitch values vary from -180 degrees to $+180$ degrees and the roll values vary from -90 degrees to $+90$ degrees.

2.2.3 Kite Field Test Conditions

The field tests were conducted on the shores of the National Institute of Technology Karnataka, Surathkal Beach. Initially, the test was conducted at low wind speeds (3 m/s to 4 m/s) to study the characteristics and learn about flying. Finding the perfect wind conditions to conduct the test was a challenge. Sometimes, there were strong winds and at other times, there was no wind. We experienced a tremendous kite-pulling force that inspired us the most. At first, a rock-mounted anchored safety line was used to hold the kite, but manoeuvring the kite became challenging as the wind direction changed. Later, wood-mounted sandbags were used as a secure platform. The weight of the sandbags was estimated by measuring the tether force from the previous tests.

2.3 Tether Force Estimation Methods

2.3.1 Wind Window and Crosswind Power

The wind profile plays an essential role in calculating the kite tether force. The 'wind window' is an area where a kite can fly in the direction of the wind [Argatov et al., 2011]. When the kite flies in the direction of the wind, it is called a downwind. As shown in Figure 2.2, if the kite is flown in the maximum power zone, it is called the crosswind zone. When the kite is at the edges of the wind window, the aerodynamic force reduces. The kite is flown in a crosswind zone in the power generation phase to generate maximum power. When the kite reaches the maximum height/length, it returns from the wind window zone and reverts to the initial state, which consumes a fraction of the energy.

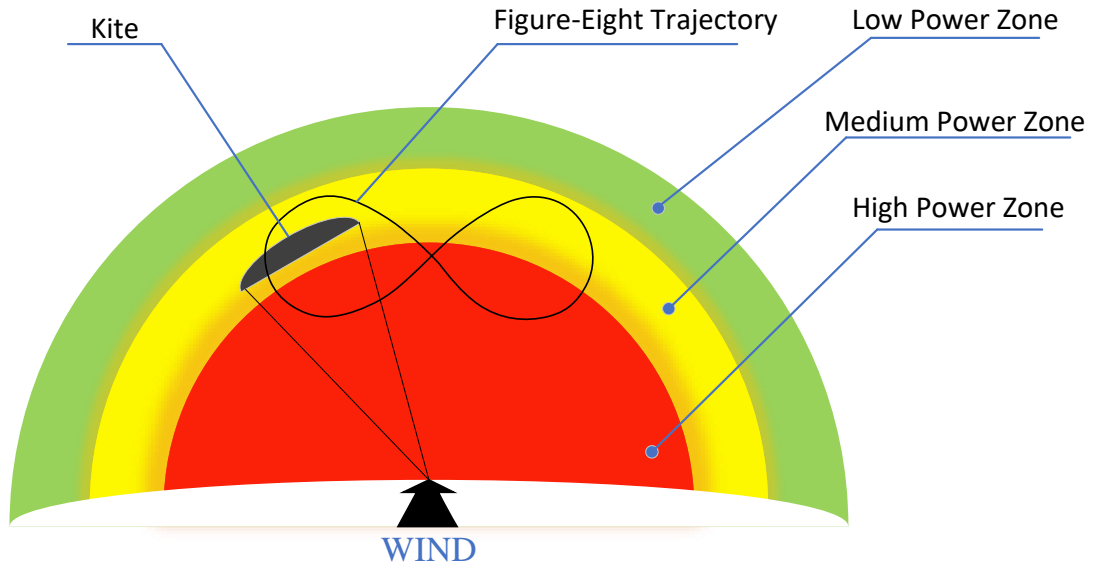


Figure 2.2: Wind window: an imaginary boundary in which the kite can be flown to produce power; the red area indicates the maximum power zone, the yellow area shows the moderate power zone, and the green area indicates the low power zone.

2.3.2 Kite Kinematics and Aerodynamic Force

The kite's position is represented using a spherical coordinate system, as shown in Figure 2.3. The proposed method uses a kite reference frame in a spherical coordinate system to represent the kite in the three-dimensional space. Figure 2.3 shows the kite reference framework in which 'K' is the kite's position, ' r ' is the tether length, and θ is the angle between the point K and zenith (Z-axis). The ϕ is the angle between the reference axis (x-axis) and the kite's orthogonal projection.

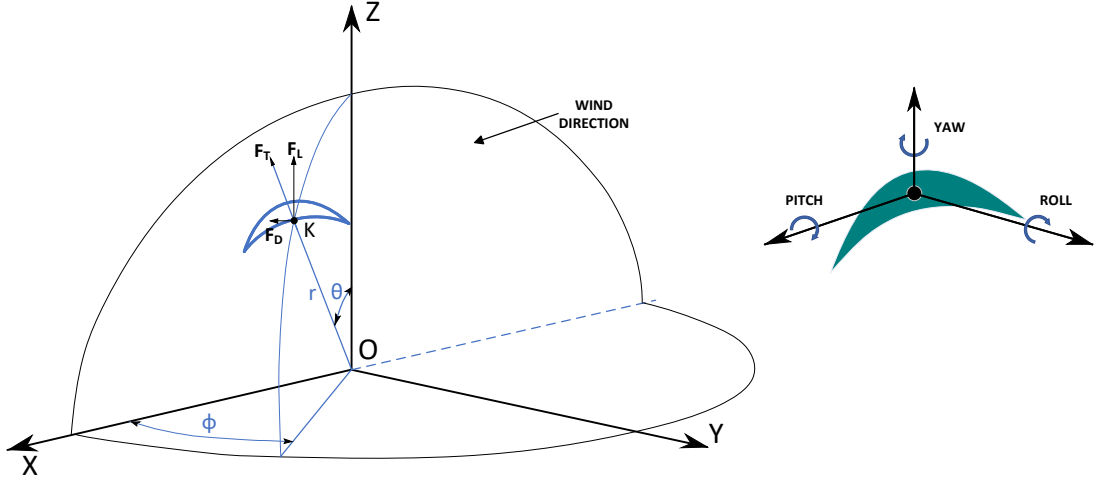


Figure 2.3: Kite reference frame [van der Vlugt et al., 2019]: The left figure shows the position of the kite at point K in a three-dimensional plane with the forces acting on the kite. The right figure shows the orientation of the kite in terms of the Euler form.

The magnitude of the lift and drag forces depends on the AoA, which varies throughout the figure-eight trajectory [Dadd et al., 2011]. The AoA can be estimated by the orientation of the kite under specific wind conditions. The lift and drag forces are estimated by

$$F_L = \frac{1}{2} \rho C_L S v_w^2 \quad (2.2)$$

$$F_D = \frac{1}{2} \rho C_D S v_w^2 \quad (2.3)$$

where ρ is the air density, C_L and C_D are the lift and drag coefficients, S is the projected area of the kite, and v_w is the wind speed. The resultant aerodynamic force is given by

$$F = \sqrt{F_L^2 + F_D^2} \quad (2.4)$$

2.3.3 Experimental Setup

The following section describes the data collection methodology from the field tests using the experimental setup. Section 2.3.3.1 through Section 2.3.3.3 explain the hardware used to acquire the kite's positional data and the wind data collection on the ground. Section 2.3.3.4 explains the tether force measurement setup and Section 2.3.3.5 explains the data logged in the field tests with a plot.

Figure 2.4 shows the experimental setup used for the measurement of the tether force. Figure 2.4a shows a pictorial representation and Figure 2.4b shows the testing of the actual system in the field. The kite used in the experiment was

a commercially available Airush Lithium 12 m² supported leading-edge inflatable (SLEI) kite, as shown in Figure 2.5. Table 2.1 shows the specifications of the kite.

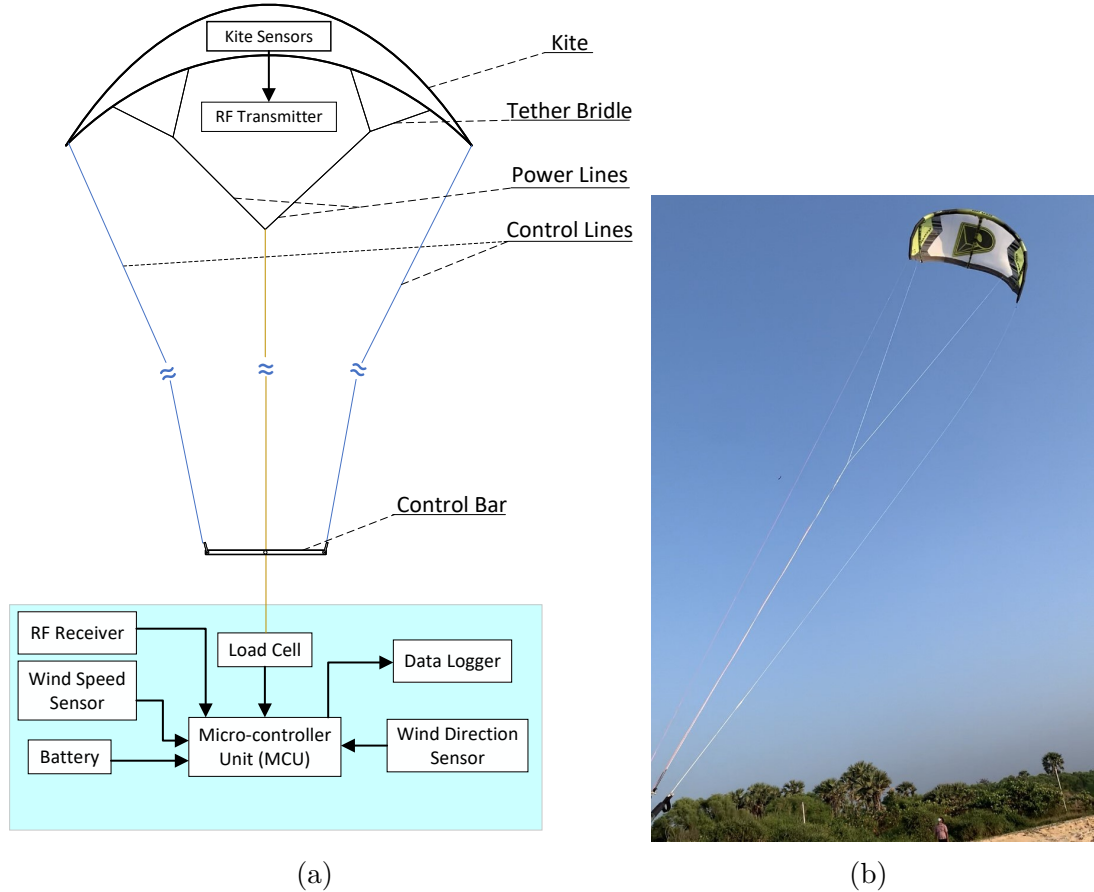


Figure 2.4: Experimental setup: (a) pictorial representation of the system used for estimating the tether force with a block diagram of the system, (b) Actual experimental setup used in the experimental tests.

Table 2.1: Kite Specifications.

Kite Parameters	
No. of Lines	4 lines
Surface Area	12 m ²
No. of Struts	3
Canopy Material	Ripstop Nylon
Weight (Deflated)	3.5 kg
Type of kite	Supported leading-edge kite (SLE)

The kite's measurement system was divided into on-air and on-ground systems. The on-air system consisted of a kite (Figure 2.5) and its sensor system (Figure 2.6). The on-ground system consisted of sensors and a data logger system (Figure

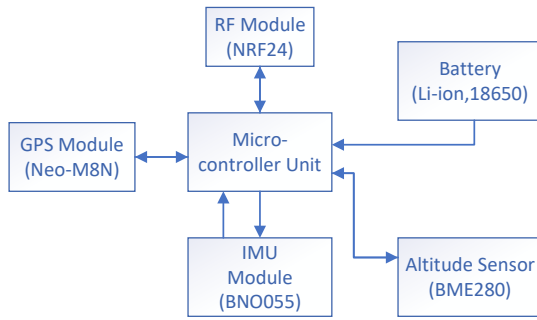


Figure 2.5: Airush Lithium 12 m² Kite.

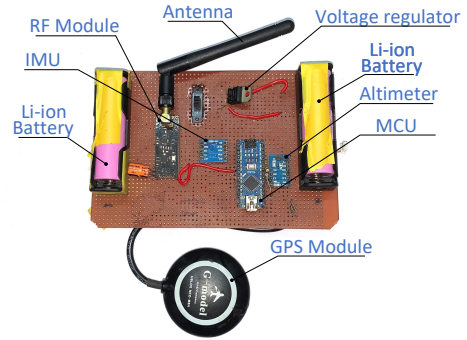
2.7). On the kite, sensors were mounted to measure its orientation, altitude, and location. The measured parameters of the kite were transmitted to the ground using a radio frequency (RF) transmitter module. On the ground, the data were logged after being received from the kite using the RF receiver module. The ground setup consisted of a load cell that measured the force of the kite, a wind speed sensor, and a wind vane to measure the wind direction.

2.3.3.1 Kite Telemetry System

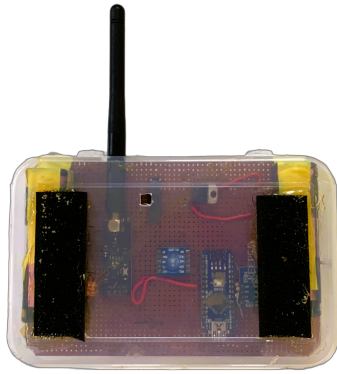
The proposed tether force estimation approach requires the orientation data of the kite. Since the kite is at a higher elevation, the kite's orientation data must be transmitted to the ground unit. The kite telemetry system is divided into on-air and on-ground units. Table 2.2 shows the specifications of the on-air and on-ground units. Figure 2.6 shows the system setup of the on-air unit.



(a) Block diagram of kite transmitter



(b) Kite transmitter circuit



(c) Kite transmitter circuit inside a box



(d) Kite transmitter mounted on the kite

Figure 2.6: Sensor system on the kite: (a) block diagram of the system, (b) PCB implementation of the sensor system, (c) PCB enclosed within the box for protection, (d) Sensor system installed on the kite using velcro.

Table 2.2: Kite telemetry system: on-air kite unit specifications and on-ground kite unit specifications.

Sl No	Part Name	On-Air Kite Unit	On-Ground Kite Unit
1	Wireless Module	NRF24L01 2.4 GHz	NRF24L01 2.4 GHz
2	Micro-Controller Unit (MCU)	ATMEGA328p, 8 bit, 16 MHz, 32 KB flash, 2 KB SRAM, 14 I/O pins	ATMEGA328p, 8 bit, 16 MHz, 32 KB flash, 2 KB SRAM, 14 I/O pins
3	Sensors (20 Hz Sampling)	IMU-BNO055 Altimeter-BME280 GPS—Neo M8N	Loadcell with HX711 ADC Anemometer (Cup type) Wind direction (Encoder)
4	Data Logging	NA	SD card module
5	Power Source	18650 Li-ion battery (Two in series—8 V)	12 V, 7.5 Ah Lead Acid Battery

As shown in Table 2.2, the micro-controller unit used in this experiment was an ATMEGA328p, which reads the sensor values and sends the values to the

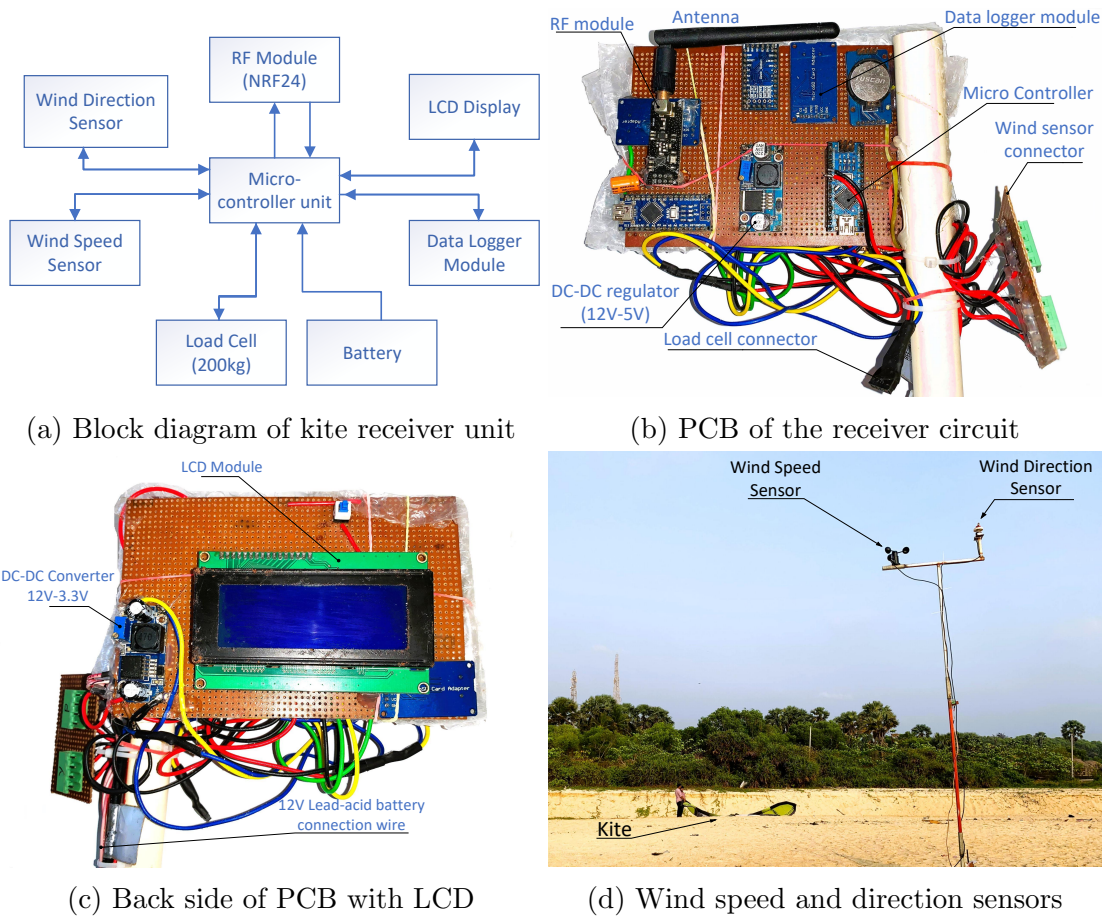


Figure 2.7: Sensor system on the ground: (a) Block diagram of the kite data receiver system on the ground, (b) Implementation of the sensor data receiver circuit in the PCB, (c) Back side of the PCB with LCD, (d) Wind speed and direction sensors at the testing site.

ground station via an RF communication link. The Inertial Measurement Unit (IMU) used in this experiment was a BNO055 module with a built-in sensor fusion algorithm. The module can produce rotations in terms of quaternions at a rate of 100 Hz. The kite's altitude was measured using a barometric pressure sensor module, BME280, which has a sampling rate of 100 Hz and has an accuracy of ± 1 m. The Global Positioning System (GPS) recorded the kite's location data, which output the kite's latitude and longitude at 20 Hz which is accurate upto ± 1 m. The sensor data were transmitted to the ground using the NRF24L01+ module, which operates at a 2.4 GHz frequency and has a transmission distance of over 1000 m. The kite's sensor system was powered by two lithium-ion batteries installed on the PCB.

2.3.3.2 On-Air Kite Unit

Figure 2.6a shows a block diagram of the sensor system mounted on the kite. Figure 2.6b shows the circuit diagram of the transmitter unit. The transmitter

unit measured the kite's orientation, altitude, and location and sent it to the ground station through the RF module. The transmitter PCB was secured inside a plastic container, as shown in Figure 2.6c, to avoid beach sand and impacts during testing. A box with a sensor unit was attached using velcro, as shown in Figure 2.6d to measure the flight data.

2.3.3.3 On-Ground Kite Unit

In addition to the kite data receiver circuit, the on-ground unit consisted of wind speed, wind direction, load cell, and data logger modules. Figure 2.7 shows the system setup of the ground sensor system. A block diagram of the ground unit is shown in Figure 2.7a. The board was implemented on a PCB, as shown in Figure 2.7b.

During the field tests, an LCD was installed for visualising the data, and an LCD was installed on which the status of the kite's data transmission and ground sensor data was displayed, as shown in Figure 2.7c. The sensors were mounted on the pole to measure the wind speed and direction. The data received from the kite was logged on the ground, which is used to estimate the force using the analytical method.

2.3.3.4 Force Measurement Unit

The force of the fixed- and short-length tethers was equal to the net aerodynamic force of the kite as per the assumptions made in Section 2.2.1. The force of the tether was measured using a load cell arrangement, as shown in Figure 2.8. One end of the load cell was anchored to the wooden platform and sandbags and the other was connected to the kite. The output voltage of the load cell changed when the tether exerted a force on the load cell. The subtle changes in voltage were converted to digital form by a 24-bit analogue-to-digital converter (HX711). The digital values obtained from the sensor were then converted to force (Newton).

2.3.3.5 Field Data Collection

The force was estimated using the recorded data from the field tests. Multiple tests were conducted to record the tether force with the kite's figure-eight trajectory data. Table 3.3 shows a sample of raw data obtained from one of the field tests, which include the kite orientation data (Q_w, Q_x, Q_y, Q_z), altitude of the kite in meters, location of the kite (latitude and longitude), force measurement from the load cell (analogue value), wind velocity (in m/s), and wind direction. The changes in the data observed in the table is due to variation of kite orientation and position in a figure-eight trajectory.

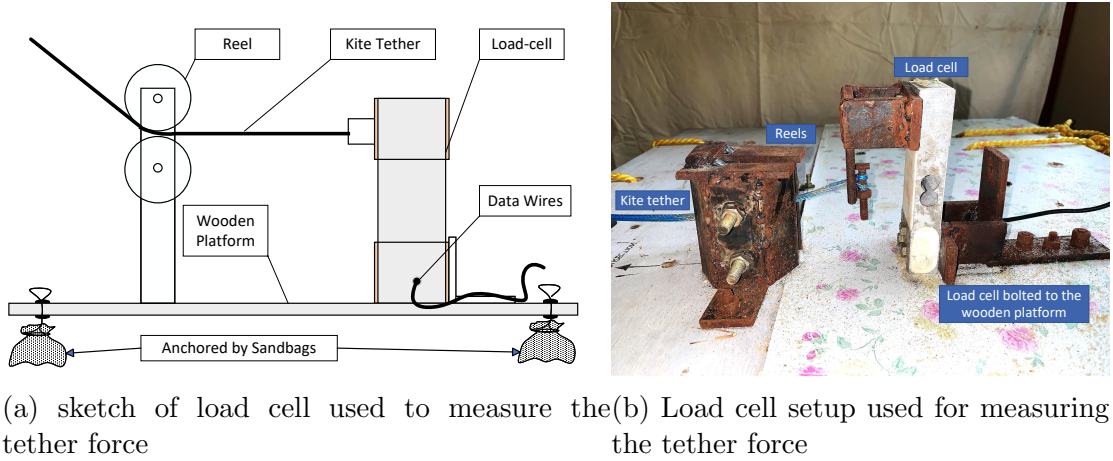


Figure 2.8: Measurement of tether force using load-cell, (a) shows the pictorial representation of the setup, (b) shows the actual setup mounted on the wooden board in which the tether is passed through the pulleys.

Table 2.3: Data logged in the field tests consisting of orientation in quaternion form, altitude, GPS data, load-cell values, wind speed, and wind direction.

Data Point	Qw	Qx	Qy	Qz	Altitude (m)	Latitude	Longitude	Load-Cell Analog Value	Wind Speed (m/s)	Wind Direction (Degrees)
1	0.04	-0.36	0.82	0.44	0.43	130091287	747885344	354,420	3.58	15
2	0.06	-0.37	0.82	0.44	0.17	130091287	747885344	611,959	3.63	6
3	0.13	-0.4	0.78	0.47	0.96	130091263	747885311	778,686	3.58	3
4	0.22	-0.44	0.73	0.48	1.95	130091232	747885259	1,012,329	3.58	7
5	0.26	-0.45	0.72	0.46	2.41	130091214	747885219	1,020,015	3.53	13
6	0.3	-0.45	0.73	0.42	4.98	130091167	747885097	955,023	3.55	17
7	0.31	-0.44	0.75	0.4	5.93	130091147	747885017	976,031	3.6	14
8	0.27	-0.41	0.79	0.36	7.14	130091131	747884937	984,059	3.6	9
9	0.2	-0.37	0.85	0.32	8.16	130091119	747884748	947,582	3.63	8
10	0.17	-0.34	0.89	0.27	10.05	130091119	747884655	788,606	3.63	11
11	0.15	-0.32	0.9	0.25	10.66	130091148	747884473	607,128	3.68	13
12	0.16	-0.32	0.9	0.22	12.23	130091164	747884386	550,783	3.7	6
13	0.19	-0.33	0.91	0.18	13.89	130091212	747884234	461,953	3.65	6
14	0.2	-0.34	0.9	0.17	15.53	130091240	747884159	399,323	3.65	15
15	0.2	-0.34	0.91	0.15	16.33	130091300	747884055	405,638	3.65	12

2.3.4 Kite Tether Force Estimation

According to the hypothesis discussed in Section 2.2.1, the force from the kite is related to its orientation. The effect of the orientation of the kite on the tether force with varying altitudes and wind speeds was studied. The orientation data of the kite in quaternion form were converted to Euler form, which resulted in the YRP angles, as discussed in Section 2.2.2. The YRP values changed their signs rapidly, which needed to be filtered to simulate the tether force. The raw values of the yaw (ψ_{RAW}), pitch (θ_{RAW}), and roll (ϕ_{RAW}) were filtered and converted into positive values. The YRP values were converted by $\psi = |\psi_{RAW}|$, $\theta = 180 - |\theta_{RAW}|$, and $\phi = |\phi_{RAW}|$, respectively.

Figure 2.9 shows the projection of area swept by the kite in the wind window in the figure-eight trajectory. The kite line is projected in the two-dimensional plane and the movement of the kite is shown in the plot. Although the lift depends on the pitch angle (θ) of the kite, the magnitude of the lift decreased as the kite made an angle β with the wind direction vector. The β angle, calculated as $|\chi - \psi|$, was zero when the kite tether vector was aligned with the wind direction vector. The β angle increased as the kite approached the edges of the wind window, which affected the lift produced by the kite.

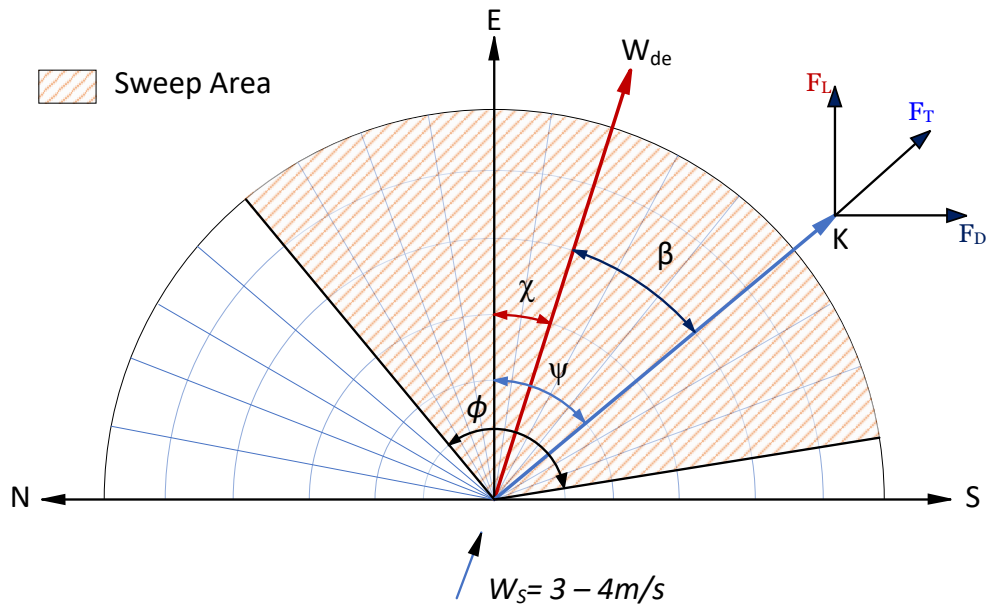


Figure 2.9: Wind window with shaded area indicating area swept by the kite in the figure-eight trajectory (ϕ degrees); W_{de} represents the wind direction vector; K represents kite tether vector; N, E, and S are the north, east, and south reference vectors; χ is the angle between east and W_{de} ; ψ is the angle between east and the kite tether vector; β is the angle between W_{de} and the kite tether vector.

Figure 2.10 shows the kite's flight path in the experimental field. As the kite moved in a figure-eight trajectory, the force varied according to the position. The GPS and altitude data collected from the field test were used to plot the kite's trajectory. Figure 2.10a shows the top view of the kite's trajectory, Figure 2.10b shows the front view, and Figure 2.10c shows the side view of the kite's trajectory. The figures show that the kite took off from the ground and followed the figure-eight trajectory. Figure 2.10d–f show the corresponding YRP angles during the trajectory of the kite.

2.3.4.1 Kite Inclination Effects

The force acting on the kite for a particular wind speed can be split into lift and drag components. The lift components act perpendicular and the drag components act parallel to the wind direction. For an airfoil, the lift and drag components depend on the wind velocity and orientation of the kite in terms of the wind. C_L

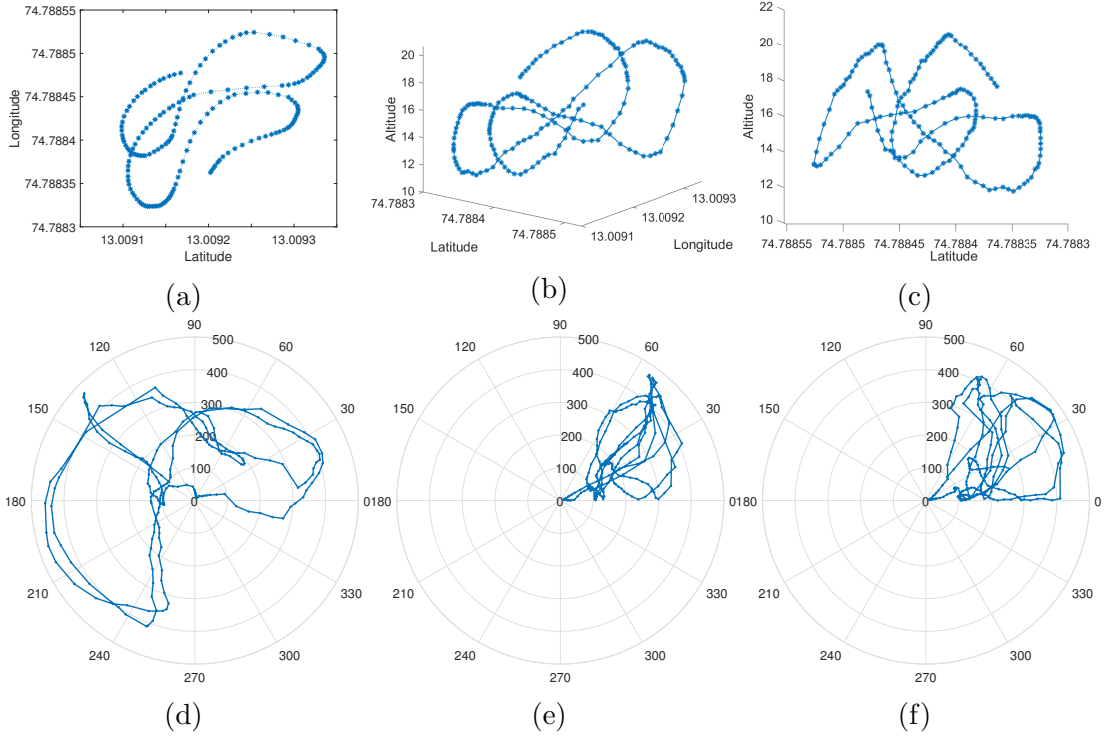


Figure 2.10: The figure-eight trajectory followed by the kite during the test. The GPS and altitude data were used to plot the trajectory of the kite in 3 dimensions. (a) Top view: lat vs. lon. (b) 3D view: lat-lon vs. altitude. (c) Side view: lat vs. altitude. (d) Yaw vs. Force. (e) Roll vs. Force. (f) Pitch vs. Force.

and C_D change the kite force as per the fundamental aerodynamic Equations (2.2) and (2.3) as a function of α (AoA) [Center, 2005] since the actual measurement of the AoA is difficult and depends on the orientation. C_L and C_D for a thin surface and low-aspect-ratio airfoil [Paiva and Fontes, 2017, Hobbs, 1986] as a function of α can be written as

$$C_L \approx 2\pi\alpha \quad (2.5)$$

$$C_D \approx 1.28 \times \sin\alpha \quad (2.6)$$

The observation made from the field tests was that the C_L is a function of the pitch angle (θ) and sweep angle (β) and C_D is a function of the pitch angle, sweep angle, and roll angle (ϕ). As discussed in Section 2.3.4, the wind window's sweep angle and roll angle induce an additional drag as a cosine function. Therefore, by reforming Equations (2.5) and (2.6), the equations for C_L and C_D can be written as

$$C_L \approx 2\pi(\theta - \beta) \quad (2.7)$$

$$C_D \approx 1.28 \times (\sin(\theta) + \cos(\beta) + \cos(\phi)) \quad (2.8)$$

2.3.4.2 Kite Tether Force Estimation using Physical Model (PM)

Field tests were performed in favourable wind conditions (3 m/s to 6 m/s) to obtain the kite’s orientation data. Hence, the lift and drag forces were estimated by using Equations (2.7) and (2.8) in Equations (2.2) and (2.3), which yields

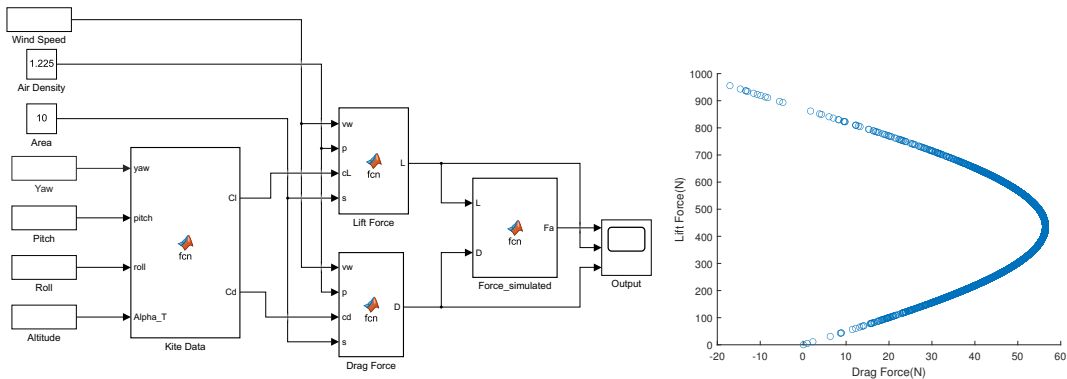
$$F_L \approx \frac{1}{2}\rho.C_L.Sv_k^2 = \frac{1}{2}\rho.2\pi(\theta - \beta).Sv_k^2 \quad (2.9)$$

$$F_D \approx \frac{1}{2}\rho.C_D.Sv_k^2 = \frac{1}{2}\rho \times 1.28 \times (\sin(\theta) + \cos(\beta) + \cos(\phi)).Sv_k^2 \quad (2.10)$$

As discussed in Section 2.3.2, the tether force was assumed to be equal to the kite’s force for a tether length of less than 24 m. Hence, the resultant aerodynamic force from Equation (2.4) yields

$$F_T = \sqrt{\left(\frac{1}{2}\rho 2\pi(\theta - \beta)Sv_k^2\right)^2 + \left(\frac{1}{2}\rho 1.28(\sin(\theta) + \cos(\beta) + \cos(\phi))Sv_k^2\right)^2} \quad (2.11)$$

Figure 2.11a shows the simulation of the tether force using the MATLAB SIMULINK environment. The parameters used for the kite were the same as those discussed in Section 2.3.3. The inputs were imported into SIMULINK in the left blocks, as discussed in Section 2.3.3.5. The following two lift and drag force blocks were used to compute the lift and drag forces based on Equations (2.9) and (2.10). Figure 2.11b shows the plot of the lift force vs. drag force, which shows a comparison of the lift and drag components of the tether force in the figure-eight trajectory. The resultant aerodynamic force based on Equation (2.11), which is equal to the tether force, was computed and displayed in the last block, as discussed in Section 2.4.2.1.



(a) MATLAB Simulink simulation blocks

(b) Lift vs. Drag Force

Figure 2.11: Simulation of tether force in MATLAB SIMULINK: (a) From left, the data from the field test are given as a numeric matrix and the kite’s data block filters the data to calculate the lift and drag forces; the force–simulated block calculates the tether force. (b) Shows a plot of the lift force vs. drag force from the simulated tether force.

2.3.4.3 Kite Force Estimation Using Deep Neural Networks

The kite’s power system modelling involves nonlinear dynamics, which depend on the wind and kite parameters. The Deep Neural Network (DNN) technique offers a good solution with noisy data compared to the physical models [LeCun et al., 2015]. The tether force was estimated using Artificial Neural Network (ANN) and Long Short-Term Memory(LSTM) algorithms. The ANN and LSTM model parameters are given in Table 2.4. Figure 2.12 shows the process of estimating the tether force using the DNN methods. The DNN was fed with 30,000 data points as the input to train the model with Adam as the training method and 1000 data points to test the model with loss evaluation by MSE method. The values needed to be normalised before being used in the DNN. The orientation data of the kite received in quaternion form were taken as the input, along with the altitude and wind speed.

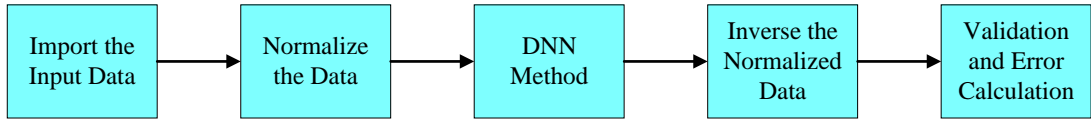


Figure 2.12: The flow of the estimation of the tether force using the DNN methods: The field test data were imported to the models and then normalised so that they could be used in the ANN and LSTM models; the predicted data in the normalised form were then inverted to the actual values; the performance was evaluated using the RMSE, MAE, and R^2 methods.

Table 2.4: Details of the parameters used in the Deep Learning Models—ANN and LSTM:

S No.	Items	Detail of ANN	Detail of LSTM
1	Target	Tether force	Tether force
2	Input Variable	$Q_w, Q_x, Q_y, Q_z,$ Altitude, Wind Speed	$Q_w, Q_x, Q_y, Q_z,$ Altitude, Wind Speed
3	Training Parameters	Learning rate: 0.0001, Number of epochs: 1000	Learning rate: 0.0001, Dropout: 0.2, Mini-Batch Size: 8, Number of epochs: 1000
4	Training dataset	Steady Wind Case (30,000) Dynamic Case (30,000)	Steady Wind Case (30,000) Dynamic Case (30,000)
5	Test dataset	Steady Wind Case (1000) Dynamic Case (1000)	Steady Wind Case (1000) Dynamic Case (1000)
6	Network layer	4 (hidden layers)	6 $\left(\begin{array}{l} \text{Fully Connected 1: Bi-directional LSTM 1:} \\ \text{Fully Connected 2: Dropout 1: Bi-directional LSTM 2:} \\ \text{Fully Connected 3: Dropout 2: Fully Connected 4} \end{array} \right)$
7	Number of neurons in each layer	100:50:25:5	100:50:50:25:25:5
8	Training Method	Adam	Adam
9	Loss function	mse	mse
10	Training Type	Regression	Regression

2.3.4.4 Artificial Neural Network (ANN)

An Artificial Neural Network (ANN) is an interconnection of neurons influenced by the human nervous system [Wang, 2003]. It is a computational approach in

which an enormous amount of neurons are inter-connected for parallel processing of the information. ANNs can find a relation between the input and output irrespective of the system's complexity. Applications of ANNs are growing day by day. In electrical engineering, they are widely used for energy prediction, optimisation, and energy forecasting [Ahmad et al., 2014] applications. Figure 2.13 shows the basic architecture of the ANN in which three layers—input, hidden, and output—are shown. The output is processed by applying weight matrices to the input layers through hidden layers with an activation function. For both the Steady Wind Condition (SWC) and Turbulent Wind Condition (TWC) flight cases, 30,000 data points were given as the training data and 1000 data points were given as the testing data. The neural network had four hidden layers and was trained using the Adam method. ANN computations were performed in the MATLAB coding environment. Table 2.4 shows the parameters of the proposed ANN approach in which the kite's orientation in quaternion form, altitude, and wind speed are given as the input matrix and the tether force is obtained as the output, as discussed in Section 2.4.2.2.

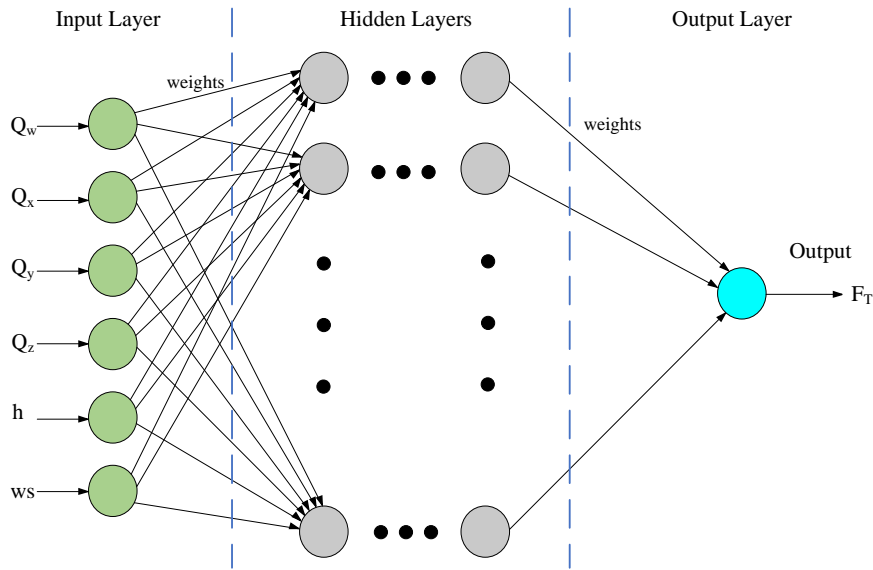


Figure 2.13: The basic architecture of the ANN: the input layer is fed with the kite's orientation data on altitude and wind speed; there are four hidden layers between the input and output and the output of the ANN was the tether force (F_t).

2.3.4.5 Long Short-Term Memory (LSTM)

The Long Short-Term Memory (LSTM) method is an advancement of the Recurrent Neural Network (RNN), which was developed by Hochreiter and Schmidhuber [Schmidhuber et al., 1997]. The LSTM model consists of sequential blocks called memory cells in which the short-term correlation between the cells is found by comparing each cell state with the adjacent cell states. The LSTM network decides to sustain, define, or update the memory state to evaluate the long-term de-

dependencies [Greff et al., 2016]. The basic structure of the LSTM network is shown in Figure 2.14. The parameters involved in the LSTM network are shown in Table 2.4. The model was fed with the kite’s orientation data, altitude, and wind speed under steady and turbulent wind conditions, with three tests in each case. The LSTM network was trained by a regression-type model with the Adam method and has six network layers. The tether force F_T was the output from the network, as discussed in Section 2.4.2.3.

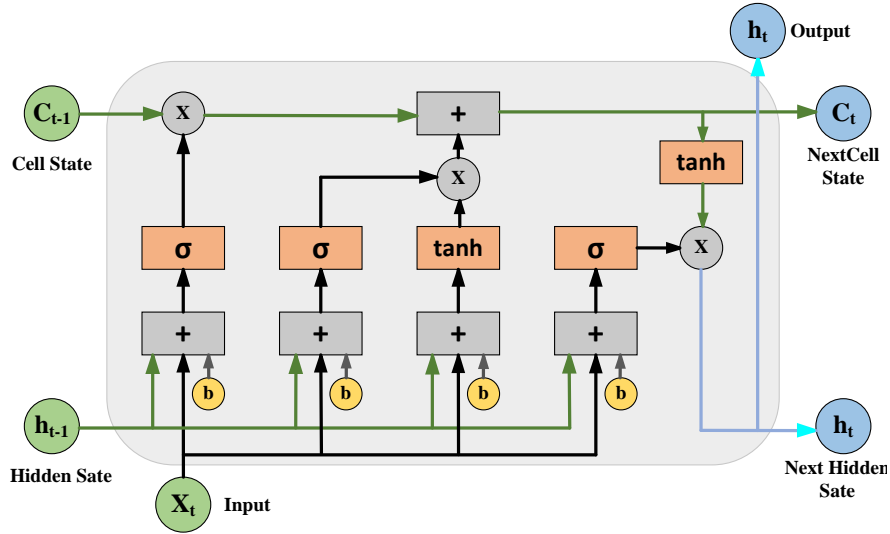


Figure 2.14: The basic structure of a Long Short-Term Memory (LSTM) unit: X_t is the current input; h_{t-1} is the last output; C_{t-1} is the memory from the last LSTM unit; h_t is the current output; C_t is the next cell state; 'b' is the bias; ' σ ' block is a sigmoid layer; ' \tanh ' block is a tanh layer; ' \times ' and ' $+$ ' are the scaling and addition operators, respectively.

2.4 Results

This section discusses the results of the tether force estimation and validation of the PM, ANN, and LSTM methods using the field test data. The combined analysis of the proposed models was performed by comparing the errors in each test case with the experimental data. Multiple flights were conducted and fed to the models, as discussed for the test data in Section 2.3.3.5. The models were tested in different test scenarios: steady wind conditions (SWC) and turbulent wind conditions (TWC). In the SWC scenario, the flight parameters (YRP and wind speed) changed gradually, whereas the parameters changed drastically in the TWC scenario. Three flight tests were conducted each for the SWC and TWC.

2.4.1 PM Simulation Results

The estimation of the tether force through simulations was performed using a MATLAB SIMULINK environment. The kite’s orientation data were loaded as

an input matrix in MATLAB and consisted of the yaw, pitch, and roll and wind velocity. The tether force was calculated using Equation (2.11), as described in Section 2.3.4.2. The simulation inputs for the two different wind profiles (SWC and TWC) and three separate field test data for each condition were taken as the inputs.

Figure 2.15 shows the simulation of the tether force under SWC. Figure 2.15a–c show the polar plots of the YRP angles vs. the tether force for tests 1, 2, and 3, respectively. The plots show the force variation versus the change in the orientation angles (YRP). In Figure 2.15a–c, it can be seen that the yaw angle varied from 0° to 270° and the roll angle varied from 0° to 70° , with abrupt changes in the force, which shows a nonlinear relationship between the force and the yaw and roll. We can also observe that the pitch angle varied, following the force in a linear relationship. Figure 2.15d–f show the time-series plots of the tether force for the corresponding YRP angles for tests 1, 2, and 3, respectively. In the figure, the left y-axis represents the YRP angles in degrees and the right y-axis represents the tether force in Newtons. In Figure 2.15d–f, it can be seen that the force varied directly with a change in the pitch angle, whereas the yaw and roll angles contributed indirectly to the estimation of the tether force.

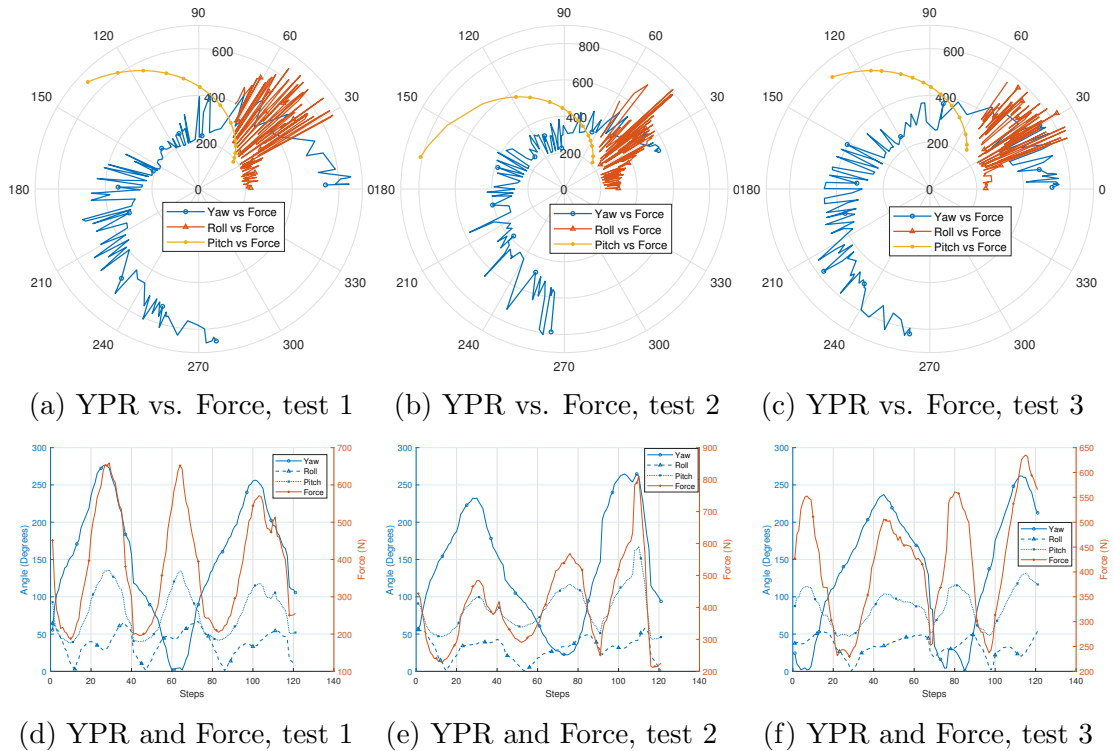


Figure 2.15: Tether force simulation for three test cases: (a–c) polar plots of the YRP vs. force; the sweep represents the angles (0° to 360°) and the magnitude represents the tether force, (d–f) time-series plots of the YRP and the tether force under the steady wind conditions.

The tether force was also simulated under TWC to investigate the effect of abruptly changing the orientation angles and wind velocity in the estimation approach. Three test data sets of the kite's orientation were used to simulate the tether force under TWC. Figure 2.16 shows the simulation results of the tether force under TWC where there were abrupt fluctuations in the YRP angles. Figure 2.16a–c show the polar plots of the YRP angles vs. tether force for test 1, test 2, and test 3, respectively. The figures show that the yaw and roll angles had high variations, whereas the pitch angle variation was acceptable for the force simulation. Figure 2.16d–f show the time-series plots of the simulated tether force for the corresponding YRP angles for test 1, test 2, and test 3, respectively. The plots show that the orientation angles varied abruptly for the TWC tests. The simulated tether force followed the pitch angle.

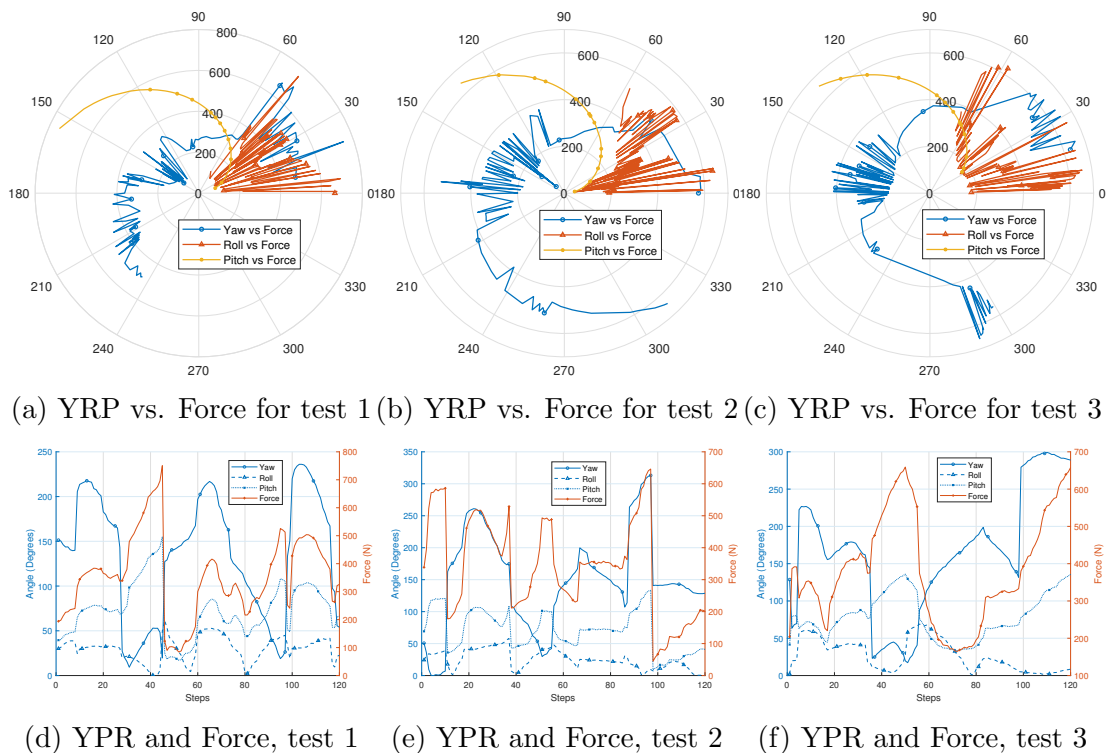


Figure 2.16: Tether force simulation for three test cases: (a–c) polar plots of the YRP vs. force; the sweep represents the angles (0° to 360°) and the magnitude represents the tether force, (d–f) time-series plots of the YRP and the tether force under turbulent wind conditions.

2.4.2 Tether Force Validation

The flight tests were conducted on the shores of NITK, Surathkal Beach. The tether length of the kite was 24 m and was kept constant. The kite was flown in figure-eight trajectories and the data were recorded for different wind speeds. The recorded kite orientation data with altitude and wind speed were taken as an input matrix in the MATLAB SIMULINK environment to estimate the tether

force using the PM, ANN, and LSTM models. The tether force estimated using the above models was validated using experimental tether force data.

2.4.2.1 Physical Model (PM) Validation

Figure 2.17 compares the simulated tether force with the experimental tether force. In the figure, F-PM represents the simulated tether force from the proposed physical model and F-Exp represents the tether force measured in the field tests. Figure 2.17a–c show a comparison of the tether force from the physical model and the experimental data for tests 1, 2, and 3, respectively, under SWC. In the figures, we can observe that the experimental data varied steadily under SWC and the physical model can estimate the tether force based on the orientation data of the kite. Figure 2.17d–f show a comparison of the simulated tether force and the experimental force under TWC for tests 1, 2, and 3, respectively. In Figure 2.17d, we can observe that the tether force in the experimental data changed abruptly due to the TWC and there was a significant error in the simulated tether force. Figure 2.17e,f also show a significant gap between the simulated force and the actual data from the field tests under TWC. From Figure 2.17, we can infer that the physical model can perform better for SWC.

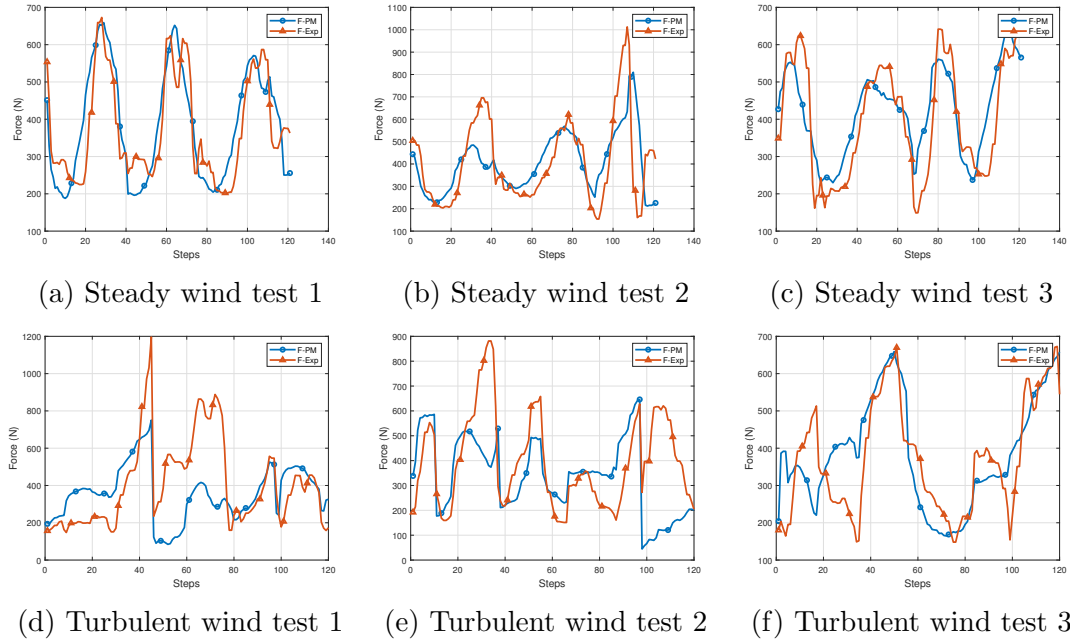


Figure 2.17: Validation of the physical model with the experimental data: (a–c) steady wind conditions, (d–f) turbulent wind conditions.

2.4.2.2 Artificial Neural Network (ANN) Model Validation

The ANN model was trained with the field test data of the SWC and TWC tests. The test results in each case were validated using the experimental data shown in Figure 2.18.

Figure 2.18a–c show a comparison of the ANN test results and the experimentally observed data for SWC in tests 1, 2, and 3, respectively. From Figure 2.18a, we can observe that the model estimated the tether force better than the experimentally observed data. Figure 2.18d–f show the test results of the ANN model compared with the experimental data for TWC in tests 1, 2, and 3, respectively. The prediction of the tether force under SWC using the ANN was similar to that of the PM. For TWC, comparing the results of the PM in Figure 2.17e with those in Figure 2.18e, we can observe that the ANN was able to predict better than the PM for TWC. From the results of the ANN model, we can infer that the model similarly estimated the tether force irrespective of steady or turbulent wind conditions.

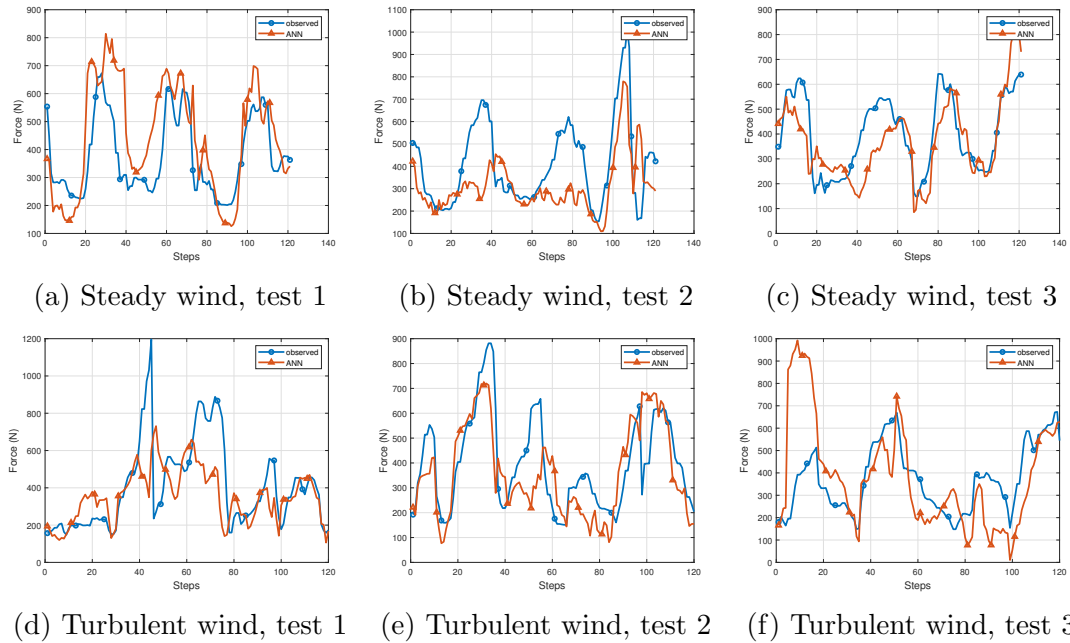


Figure 2.18: Experimental validation of predicted tether force from ANN: (a–c) test results for steady wind conditions, (d–f) test results for turbulent wind conditions.

2.4.2.3 Long Short-Term Memory (LSTM) Model Validation

The LSTM model was trained and tested using the same data points as the physical and ANN models. Figure 2.19 show the test results of the LSTM model compared with the experimental data. Figure 2.19 (a-c) show the test results of the LSTM compared with the experimental results for SWC in tests 1, 2, and 3, respectively. From Figure 2.19a, we can observe that the model performed better and predicted the tether force compared with the experimental data. In Figure 2.19b, we can observe a deviation in the actual results for test case 2. Figure 2.19 (d-f) show a comparison of the test results of the LSTM with the experimental data for TWC in tests 1 to 3, respectively. In Figure 2.19d, we can see that the model was able to estimate the tether force under TWC, except for

the spike in the force value. In Figure 2.19e,f, the estimated values were divergent compared to the experimental values for TWC.

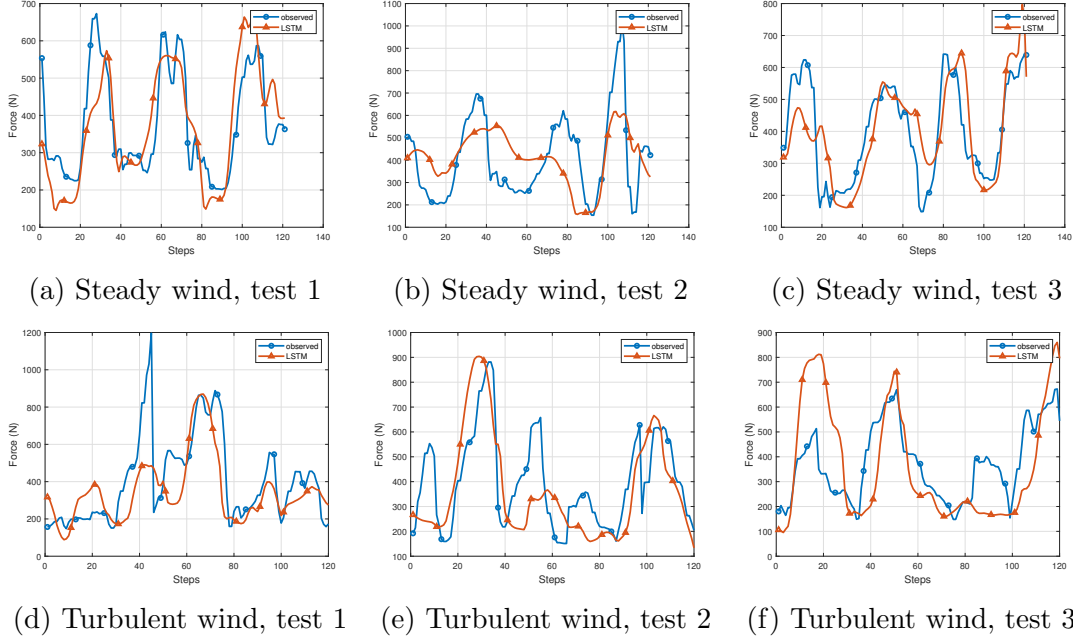


Figure 2.19: LSTM model test results comparison with the experimental data: (a–c) steady wind condition data for the three tests, (d–f) turbulent wind condition data for the three tests.

2.4.2.4 Comparison and Validations of Models

The PM, ANN, and LSTM model results were compared with the actual values measured in the field tests for the combined analysis of the models. Figure 2.20 shows a comparison of the proposed methods with the experimental values for steady and turbulent wind conditions in three test cases. From Figure 2.20 (a-c), we can infer that the physical model performed better in estimating the tether force under SWC in all three test cases. In Figure 2.20 (d-f), we can infer that the performance of the PM decreased for TWC as it was susceptible to the noise in the input data, whereas the machine learning methods performed better for TWC.

Figure 2.21 shows the performance of the PM, ANN, and LSTM models with a linear regression line with a confidence interval (C.I) of 95%. The regression line represents the best fit of the observed values. Figure 2.21a–c show the scatter plots for 363 data points under SWC and Figure 2.21d–f show the plots for TWC. In Figure 2.21a, the performance of the PM under SWC is shown and it can be seen that the observed points are closer to the regression line, which represents the estimated values being closer to the actual values. Figure 2.21b shows the performance of the ANN model under SWC where the observed values are away from the regression line, indicating that the prediction value was less accurate. Figure 2.21c shows the performance of the LSTM model under SWC, where we

can see that the observed values were better than the ANN model. Figure 2.21d shows the performance of the PM under TWC. The figure shows that the values are away from the regression line, indicating a reduction in accuracy for TWC. However, the ANN and LSTM model performances, as shown in Figure 2.21e,f, performed better compared to the PM for TWC.

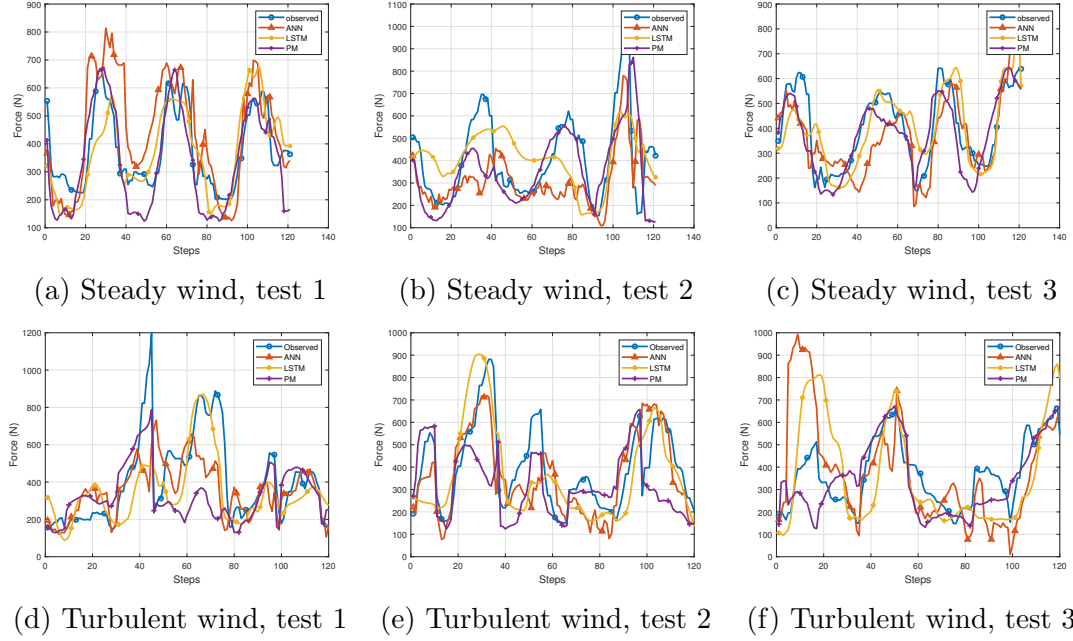


Figure 2.20: Combined analysis of tether force estimation methods—physical, ANN, and LSTM methods: (a–c) the three tests under steady wind conditions, (d–f) the three tests under turbulent wind conditions.

The error parameters for the three methods were compared with three different error parametrics—the root mean square error (RMSE), mean absolute error (MAE), and R-squared (R^2) method.

2.4.2.4.1 RMSE Method: This method evaluates the standard deviations in the estimated tether force which are calculated using the equation

$$RMSE_{F_T} = \sqrt{\frac{\sum_{i=1}^N (F_{actual} - F_{estimated})^2}{N}} \quad (2.12)$$

where $RMSE_{F_T}$ denotes the RMSE of the tether force, F_{actual} is the tether force from the field test, $F_{predict}$ is the estimated tether force from the machine learning algorithm, and N is the number of non-missing data points.

2.4.2.4.2 MAE Method: This method calculates the mean absolute error involved in the tether force measurement. The absolute error is the difference between the actual and estimated tether force. The formula to calculate the MAE

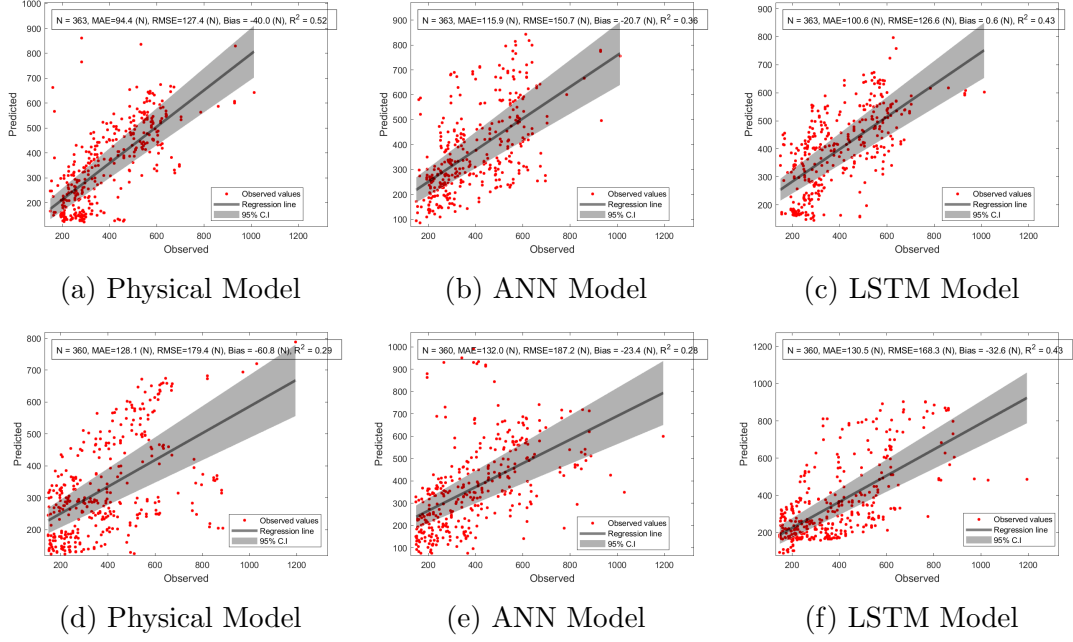


Figure 2.21: Scatter plots of the physical, ANN, and LSTM models: (a–c) the performance of the models under steady wind conditions, (d–f) the performance of the models under turbulent wind conditions.

for the tether force is given below:

$$MAE_{F_T} = \frac{\sum_{i=1}^N |F_{actual} - F_{estimated}|}{N} \quad (2.13)$$

where MAE_{F_T} is the mean absolute error in the tether force and n is the number of errors.

2.4.2.4.3 R^2 Method: The R-squared method is used to evaluate the best fit or goodness of fit of the expected tether force with the experimental values using the ratio of the sum of squares regression (SSR) and the sum of squares total (SST). The value of R-squared varies from zero to one and has to be closer to one for a better result. The formula to evaluate the error using the R^2 method is as follows:

$$R_{F_T}^2 = 1 - \frac{SSR}{SST} = 1 - \frac{\sum_{i=1}^N (F_{actual} - F_{estimated})^2}{\sum_{i=1}^N (F_{actual} - \frac{\sum F_{actual}}{N})^2} \quad (2.14)$$

Figures 2.22 and 2.23 show the performance analysis of the PM, ANN, and LSTM models for the three tests under SWC and TWC, respectively. In the figures, a lighter cell colour for the RMSE and MAE methods indicates a better estimation of the tether force, whereas for the R^2 method, a darker cell colour indicates a better estimation of the tether force.

In Figure 2.22a, it can be seen that the overall RMSE values of the PM and LSTM models were 127 N and 126 N, respectively, compared to a value of 150 N

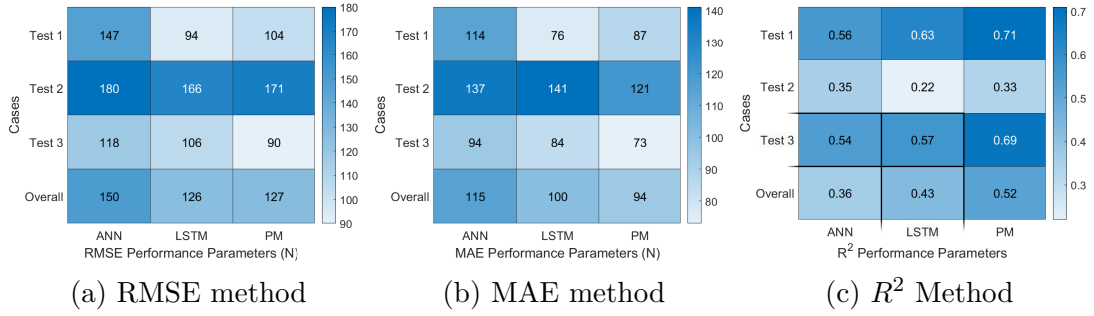


Figure 2.22: Performance analysis of PM, ANN, and LSTM models under steady wind conditions: (a) RMSE method, (b) MAE method, (c) R^2 method.

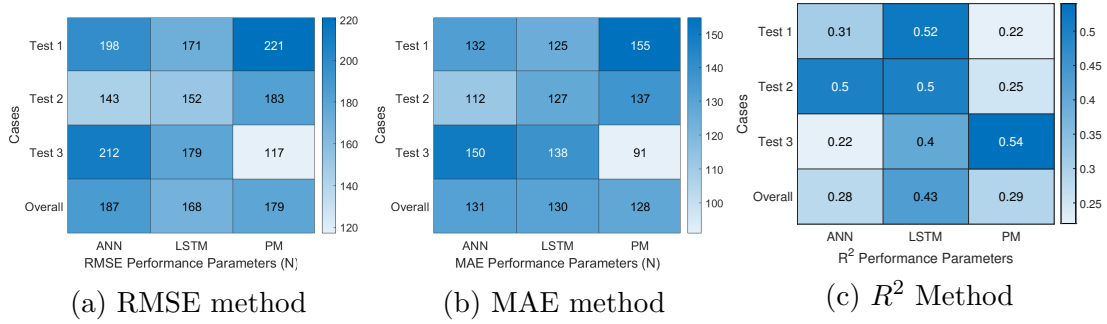


Figure 2.23: Performance analysis of PM, ANN, and LSTM models under turbulent wind conditions: (a) RMSE method, (b) MAE method, (c) R^2 method.

for the ANN model, which indicates that the PM and LSTM models performed better in SWC. Using the MAE method, the PM had the overall lowest error value of 94 N compared to 115 N and 100 N for the ANN and LSTM, respectively, as shown in Figure 2.22b. In Figure 2.22c, it can be seen that the PM had an overall performance score of 0.52, which shows good estimation compared to the scores of 0.36 and 0.43 for the ANN and LSTM methods, respectively, using the R^2 method.

Under TWC, the overall RMSE value of the LSTM was 168 N, which was the lowest compared to 187 N and 179 N using the ANN and PM, respectively, as shown in Figure 2.23a. In Figure 2.23b, it can be seen that the PM had the overall lowest error value of 128 N, indicating better estimation compared to 131 N and 130 N using the ANN and LSTM methods, respectively, with the MAE method. The R^2 method, as seen in Figure 2.23c, shows that the LSTM method was more accurate, with a value of 0.43, which was the highest among the three, with 0.28 for the ANN and 0.29 for the PM, indicating a better estimation of the tether force in TWC than the ANN and PM.

2.5 Summary

Airborne wind energy has the potential to solve some of the shortcomings of conventional wind turbines. Estimating the tether force is essential for determining the power generation capabilities of the system. The kite is steered in crosswind figure-eight manoeuvres to harvest wind energy. Multiple field tests were conducted in a coastal region to study the kite's flight dynamics under steady wind conditions (SWC) and turbulent wind conditions (TWC). The test data collected in the field tests were used to estimate the tether force using MATLAB Simulink and Deep Neural Network (DNN) models. The combined analysis of the tether force estimation using the proposed methods was validated using experimental tether force data and the performance of the methods was evaluated using the RMSE, MAE, and R^2 methods.

The proposed physical model (PM) had an overall error value of 127 N using the RMSE method and 94 N using the MAE method in estimating the tether force in SWC. However, in turbulent wind conditions, the overall error values increased to 179 N and 128 N using the RMSE and MAE methods, respectively. The PM had a performance index of 0.52 in SWC and 0.29 in TWC using the R^2 method, indicating better estimation in SWC than TWC. The proposed ANN model had error values of 150 N and 115 N in SWC using RMSE and MAE methods, respectively, and in TWC, the error values increased to 187 N and 131 N, respectively. The R^2 method indicated the change in the error values from 0.36 in SWC to 0.28 in TWC for the ANN method. In the proposed LSTM method, we observed error values of 126 N using the RMSE and 100 N using the MAE in SWC. The error values increased to 168 N using the RMSE and 130 N using the MAE in TWC. Using the R^2 method, we observed that the LSTM had an error value of 0.43 in both SWC and TWC, which indicates that the LSTM method had similar performance in the estimation of the tether force in both SWC and TWC.

The PM model relied on the ground-level wind velocity; however, in TWC, the wind velocity at the position of the kite changed rapidly, which made the estimation less accurate. Based on the RMSE method, we can deduce that the LSTM model performed better than the PM and ANN, with overall error values of 126 N and 168 N in SWC and TWC, respectively. The performance of the PM in TWC can be improved by measuring the wind velocity at the kite's position.

Chapter 3

Simulation of Kite Power System

Contents

3.1	Introduction	37
3.2	KPS Emulator Modelling	38
3.2.1	Kite Dynamics	38
3.2.2	PMSM Modelling	42
3.2.3	Simulation Model	44
3.2.4	Emulator Model	45
3.2.5	Comparison with Conventional Wind Turbine	47
3.3	Simulation Results and Discussion	48
3.3.1	No-load Test	49
3.3.2	On-load Test	49
3.3.3	Field Test Data Analysis	53
3.3.4	Simulation using the satellite data	54
3.3.5	Verification using experimental data	57
3.3.6	Discussion and Applications	59
3.4	Summary	59

3.1 Introduction

Kite Power System (KPS) is a promising method for capturing the power from winds at high altitudes. The current chapter discusses the proposed KPS emulator based on Field Oriented Control (FOC)-based PMSM with experimental kite data and discusses the system's potential with 1 kW, 10 kW, and 100 kW systems. The KPS is also compared with CWT to evaluate the energy production capabilities of the KPS. Figure 3.1 shows the proposed block diagram of KPS, which consists of five parts.

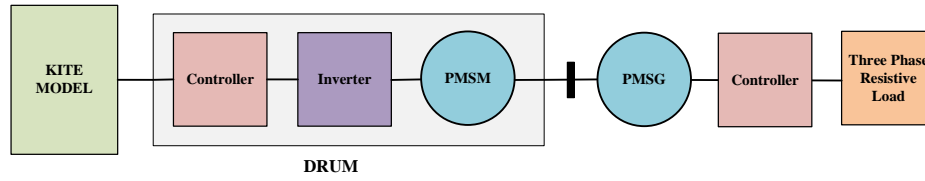


Figure 3.1: Block diagram of a kite power generation system.

The first part is the kite system which gives the output in the form of torque and reel-out speed, and it translates into mechanical power; this automated power control in the kite emulator system is shown in the second block, which consists of a controller, a power converter and permanent magnet synchronous motor (PMSM), which combined known as a drum. The drum is mechanically coupled with a PMSG (permanent magnet synchronous generator) that transforms mechanical energy into electrical energy.

The main contribution and novelty of this proposed research work in listed:

- The study analyses the scalability of the KPS using PMSM and key results are discussed.
- The dynamic behaviour of a kite-based wind power generation. The effect of wind speed in terms of reel-out speed, tether force, traction power, drum speed, and drum torque is described.
- The design, simulation, and implementation of an airborne wind energy turbine emulator system built using PMSM.
- The KPS emulator is tested with the experimental data from the field tests and the behaviour of the system is described.

The chapter is organised as follows - the mathematical formulations of the kite model, PMSM model, simulation model, the emulator model, and the comparison with the conventional wind turbine is described in section 2. The simulation results and the discussions are presented in section 3, which describes the dynamic behaviour of the kite; further, we have presented no load, on-load tests, and field test data analysis with experimental ground data simulation results. Section 4 summarizes the research outcomes and explains future works.

3.2 KPS Emulator Modelling

3.2.1 Kite Dynamics

The wind reference frame serves as the initial point of reference for the analysis as shown in Figure 3.2. Its origin, 'O', coincides with the location where the rope exits the ground station, and both its Z-axis and X-axes are oriented in the direction

of the wind. We employ a spherical coordinate system (r, θ, ϕ) and the methods described in references [van der Vlugt et al., 2019, Schmehl et al., 2013, Noom, 2013] to define its position K and velocity $u_a \in \mathfrak{R}$ [m/sec], the radial distance $r \in \mathfrak{R}$ [m], polar angle $\theta \in \mathfrak{R}$ [rad], and azimuth angle $\phi \in \mathfrak{R}$ [rad] are used to represent the position. The course angle $\chi \in \mathfrak{R}$ [rad] indicates the direction of flight in the local tangential plane. Figure 3.2a shows the geometrically similar velocity and force diagrams where u_a and F_a are decomposed in the vector plane. When assuming a straight tether and a minimal mass effect, $u_{a,r}$ aligns with F_a . In figure 3.2b, the kite velocity u_k is decomposed in radial direction $u_{k,r}$ and tangential direction $u_{k,t}$. The apparent wind velocity u_a is defined as the difference between the wind velocity u_w and the velocity of the kite u_k . Course angle χ is measured in the tangential plane defined in the wind framework for reference X, Y, and Z axes.

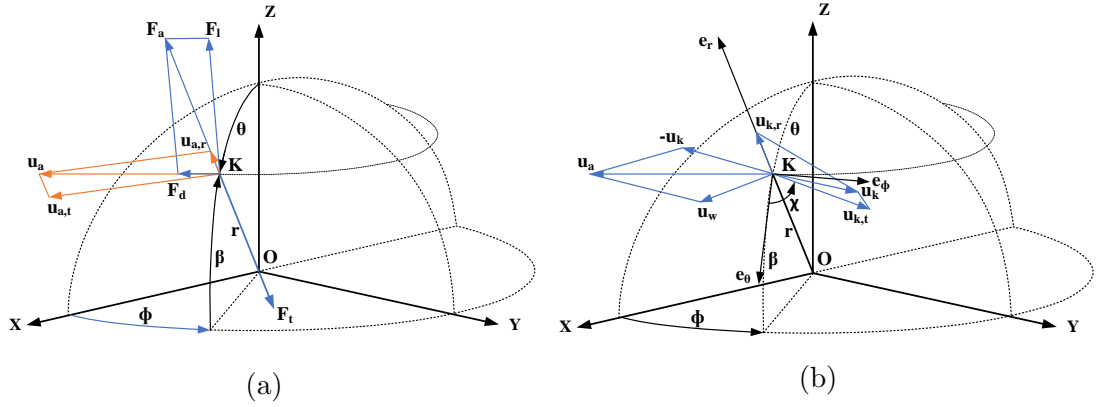


Figure 3.2: Spherical coordinate and geometric decomposition of the kite system: Fig.(a) shows, the force and speed representations are geometrically comparable. Fig.(b) shows the decomposing kite velocity into radial and tangential components.

The apparent wind speed characterises the flow rate in relation to the kite [van der Vlugt et al., 2019].

$$u_a = u_w - u_k \quad (3.1)$$

we can also write apparent wind speed in spherical coordinates as shown below

$$u_a = \begin{bmatrix} \sin \theta \cos \phi \\ \cos \theta \sin \phi \\ -\sin \phi \end{bmatrix} u_w - \begin{bmatrix} 1 \\ 0 \\ 0 \end{bmatrix} u_{k,r} - \begin{bmatrix} 0 \\ \cos \chi \\ -\sin \chi \end{bmatrix} u_{k,t} \quad (3.2)$$

where the kite's radial and tangential contributions to its speed are denoted by $u_{k,r}$ and $u_{k,t}$ respectively.

The straight tether suggests that the reeling speed and radial kite speed are the same and this assumption implies that the tether mass is neglected to simplify the simulation approach.

$$u_{k,r} = u_{k,t} \quad (3.3)$$

The reeling factor as

$$p = \frac{u_{k,r}}{u_w} \quad (3.4)$$

And the tangential speed factor as

$$q = \frac{u_{k,t}}{u_w} \quad (3.5)$$

The second equation may be written as

$$u_a = \begin{bmatrix} \sin \theta \cos \phi - p \\ \cos \theta \sin \phi - q \cos \chi \\ -\sin \phi - q \sin \chi \end{bmatrix} u_w \quad (3.6)$$

The steering system controls the course angle χ , the ground station controls the reeling factor p , and the force equilibrium determines the dependent variable, the tangential speed factor q . The kite flies in figure-of-eight crosswind trajectories and the aerodynamic force of the kite varies throughout the flight. The figure-of-eight trajectory data is taken from the field tests to compute the aerodynamic forces of the kite which is discussed in section 3.4.

The components of the airborne wind energy system's integral aerodynamic force can be separated into the lift and drag forces

$$\vec{F}_a = \vec{F}_L + \vec{F}_D \quad (3.7)$$

The lift force and drag force are written as

$$\vec{F}_L = \frac{1}{2} \rho C_L u_a^2 A \quad (3.8)$$

And

$$\vec{F}_D = \frac{1}{2} \rho C_D u_a^2 A \quad (3.9)$$

the kite projected surface area $A \in \Re [m^2]$, apparent wind speed $u_a \in \Re [m/s]$, air density $\rho \in \Re [kg/m^3]$, lift and drag coefficients C_L and C_D are respectively. The aerodynamic force represent as

$$\vec{F}_a = \frac{1}{2} \rho C_R u_a^2 A \quad (3.10)$$

Where

$$C_R = \sqrt{C_D^2 + C_L^2} \quad (3.11)$$

Assume aerodynamic force $F_a \in \Re [N]$ is balanced by tether force $F_t \in \Re [N]$ shown in Figure 3.2, and represent as

$$\vec{F}_t = -\vec{F}_a \quad (3.12)$$

The Reel-Out Speed $u_r \in \Re [m/s]$ is calculated using the wind speed $v_w \in \Re [m/s]$ and Lift Force $F_L \in \Re [N]$ describe in References [Fechner and Schmehl, 2014]

$$u_r = v_w \sin \theta \cos \phi - \sqrt{-h^2 - g^2 + \frac{2F_L}{C_L A \rho}} \quad (3.13)$$

$$h = u_{k,t} \sin \chi + v_w \sin \phi, \quad g = u_{k,t} \cos \chi - v_w \cos \phi \cos \theta$$

According to Loyd's calculations, the maximum amount of mechanical power can be generated at a specific reel-out speed u_r . This is provided by

$$u_r = \frac{1}{3} \cdot v_w \quad (3.14)$$

The drum speed relating to the tether reel-out speed is given by,

$$u_r = r \cdot \omega_d \quad (3.15)$$

where u_t is the reel-out speed of the tether and ω_d is the angular velocity of the drum and r is the drum radius. Figure 3.3 shows the interaction between the kite tether and the drum. The drum torque (T_d) $\in \Re$ [Nm] is equal to the multiplication of drum radius and the tether force:

$$T_d = F_t \cdot r = F_t \cdot \frac{D}{2} \quad (3.16)$$

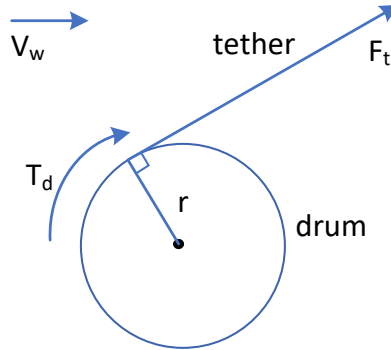


Figure 3.3: Interaction of drum and the kite tether.

From equation 3.14, by knowing the wind speed (m/s) we can obtain the reel-out speed of the tether (m/s). With the additional input of the diameter of the drum, the optimum speed of the drum (RPM) can be estimated using the following equation:

$$N_d = \frac{u_r}{2\pi r} \cdot 60 = \frac{u_r}{\pi D} \cdot 60 \quad (3.17)$$

Where D is drum diameter $\in \Re$ [m], N_d is drum speed $\in \Re$ [rpm].

The drum power (P_d) $\in \Re$ [W] of the kite is calculated by multiplying the drum torque by the drum speed in the following formula:

$$P_d = T_d \cdot \omega_d \quad (3.18)$$

Where ω_d is drum speed $\in \Re$ [rad/s]

3.2.2 PMSM Modelling

The equivalent electric model of PMSM shown in Figure 3.4, which comprises of stator phase resistance $R_s \in \mathfrak{R} [\Omega]$, synchronous inductance $L_s \in \mathfrak{R} [\text{H}]$, and EMF $E_s \in \mathfrak{R} [\text{V}]$, can be employed to represent each machine's phase. Here we are considering the synchronous inductance (L_s) is equal to quadrature-axis inductance (L_q) and direct-axis inductance (L_d). The magnetic circuit is assumed to have linear properties (saturation neglected), constant air gap and sinusoidal behaviour of a three-phase current.

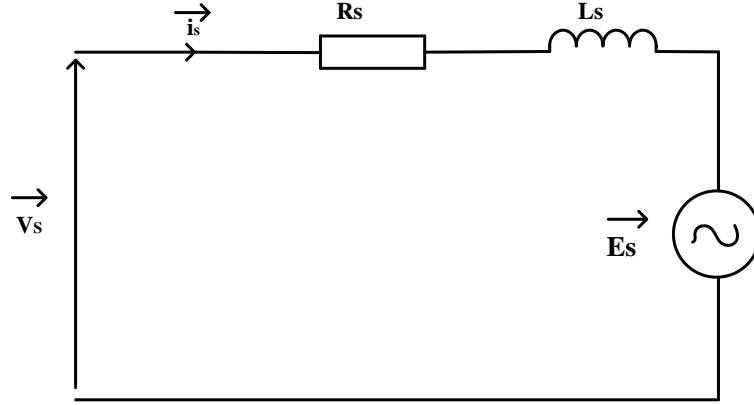


Figure 3.4: Equivalent electrical circuit of PMSM.

The variables vector presentation shows all three phases at the same time. It is shown in park coordinates (d,q) by [Ba et al., 2022],

$$v_{sq} = R_s i_{sq} + L_s \frac{di_{sq}}{dt} + \omega L_s i_{sd} + w \phi_{fsd} \quad (3.19)$$

$$v_{sd} = R_s i_{sd} + L_s \frac{di_{sd}}{dt} - \omega L_s i_{sq} \quad (3.20)$$

$$\phi_{sd} = L_s i_{sd} + \phi_{fsd} \quad (3.21)$$

$$\phi_{sq} = L_s i_{sq} \quad (3.22)$$

$$T_e = p \phi_{fsd} i_{sq} \quad (3.23)$$

Where, the voltage at the stator is represented by the vector $\vec{v}_s = v_{sd} + j.v_{sq}$, the current at the stator is represented by the vector $\vec{i}_s = i_{sd} + j.i_{sq}$, the flux produced by PMSM is $\vec{\Phi}_{fs} = \phi_{fsd} + \phi_{fsq}$, ω is the electric pulsation, and p is the number of pole pairs.

The voltage source inverter circuit shown in Figure 3.5 has six toggle switches and operates from a supply voltage of V_{dc} . Depending on the use case, the AC voltage's frequency may be changed or held constant. Reference voltages are generated by the current regulators; these voltages are then inverted using the field-oriented control technique developed by Clarkes and Parks transform. The

sinusoidal pulse width modulation generator uses the reference voltage as input to generate switching pulses for the three-phase inverter. This dc input voltage is sent into the three-phase inverter, which in turn generates an ac output voltage that drives the motor [Suman and Mathew, 2018].

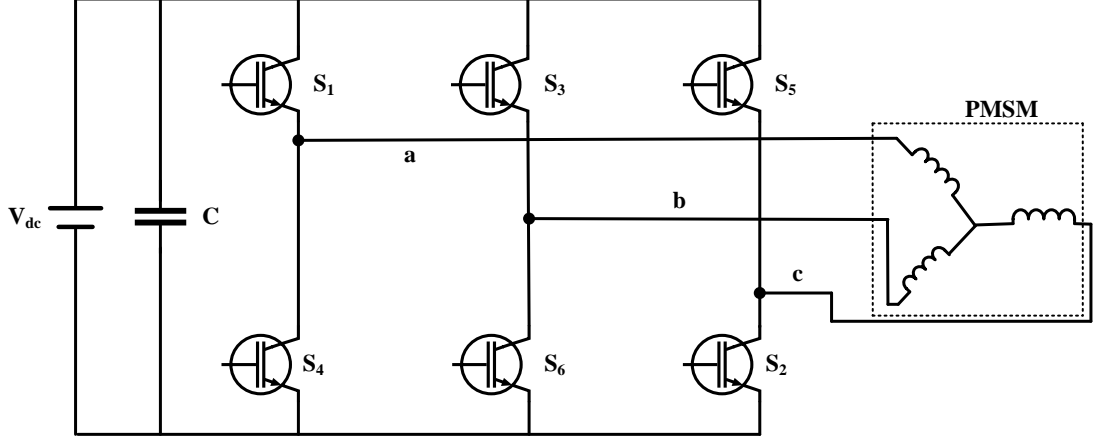


Figure 3.5: kite conversion system (with gear-ratio and drum) using power converter with PMSM.

Park and clarkes transform is used to convert three-phase (abc) to two-phase (dq) which is written as

$$v_{sq} = \frac{2}{3} \left[V_a \cos \theta + V_b \cos \left(\theta - \frac{2\pi}{3} \right) + V_c \cos \left(\theta + \frac{2\pi}{3} \right) \right] \quad (3.24)$$

$$v_{sd} = -\frac{2}{3} \left[V_a \sin \theta + V_b \sin \left(\theta - \frac{2\pi}{3} \right) + V_c \sin \left(\theta + \frac{2\pi}{3} \right) \right] \quad (3.25)$$

And inverse Park and Clarkes transform is used to convert from two phases (dq) to three phases (abc), which is written below

$$V_a = V_q \cos \theta - V_d \sin \theta \quad (3.26)$$

$$V_b = V_q \cos \left(\theta - \frac{2\pi}{3} \right) - V_d \sin \left(\theta - \frac{2\pi}{3} \right) \quad (3.27)$$

$$V_c = V_q \cos \left(\theta + \frac{2\pi}{3} \right) - V_d \sin \left(\theta + \frac{2\pi}{3} \right) \quad (3.28)$$

where, The three-phase electrical output power of the generator is written below

$$P_e = \sqrt{3}.V_L.I_L \cos \Phi \quad (3.29)$$

Where V_L and I_L are the generator voltage and current respectively. $\cos \phi$ is the power factor. The Kite power evaluated using Equation 3.18 and generator output power evaluated using Equation 3.29 matches to each other can be seen in by Figure 3.12i.

3.2.3 Simulation Model

Figure 3.6 depicts the simulation of the reel-out speed, tether force, drum speed, and drum torque using the MATLAB SIMULINK environment. The parameters used for the kite were the same as those discussed in Section 2. The following two lift and drag force blocks were used to compute the lift and drag forces based on Equations 3.8 and 3.9 respectively. The resultant of aerodynamic force based on Equation 3.10, which is equal to the tether force, was computed and displayed in the third block. The reel-out speed estimator shown in block four is estimated based on Equations 3.13 and 3.14, and the last block is a drum, which produces drum torque and speed based on equations 3.16 and 3.17 respectively.

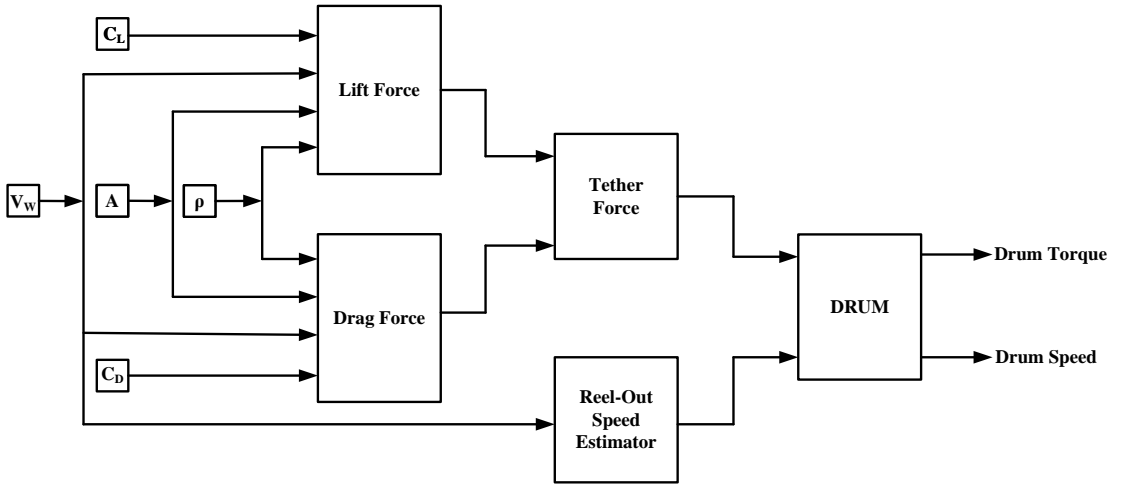


Figure 3.6: Wind speed to the kite force (torque and speed) conversion system in Matlab Simulink.

Drum speed ($\omega_d \in \Re$ [rad/s] in term of tether force shown in below:

$$\omega_d = \frac{P_d}{F_t \cdot (\frac{D}{2})} \quad (3.30)$$

Where P_d is the drum power in watts, F_t is the tether force and D is the drum diameter. This equation provides the relation between tether force and drum speed.

Figure 3.7 shows the flow chart and gives an overall view of the methodology used in this investigation. The first block shows the collection of the wind data (A , C_L , C_D , ρ , and u_w) depicted in table 3.1, which is the input parameter of the kite dynamic block. The dynamic kite block generates mechanical kite power by using Equation 3.18. In the next stage, the drum dynamic estimates torque and speed using Equation 3.16 and 3.17, respectively.

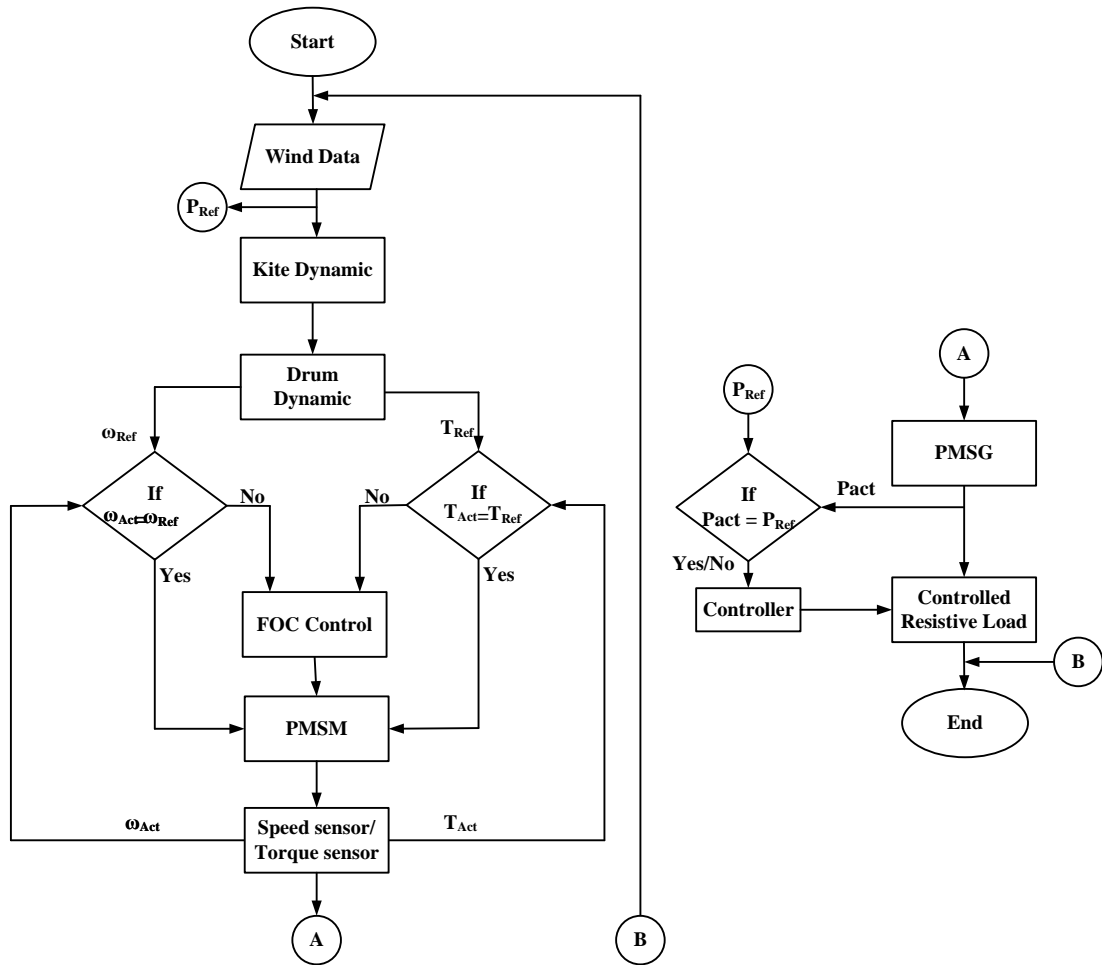


Figure 3.7: Flow chart of KPS emulator.

The torque and speed of the PMSM motor is controlled using field-oriented control technique in the next phase. In the next step, a torque and speed sensor measures the motor's speed and torque and compares it to the reference speed and torque; if the two do not match, the control is returned to the controller, which fixes the error. In the next stage, PMSG converts mechanical power to electrical power. The output of PMSG is connected to the controlled resistive load through a load controller.

3.2.4 Emulator Model

The kite emulator consists of a combination of a kite model, a permanent magnet synchronous motor, a three-phase inverter (DC/AC converter), and controllers. PMSM is used to mimic the KPS characteristics. The PMSM is regulated by following the kite airborne wind turbine's torque command. The motor provides high-performance torque control using the field orientation control (FOC) method. The developed PMSM-based KPS system's overall control mechanism is shown in Figure 3.8. The power inverter uses sinusoidal pulse width modulation (SPWM)

to supply the motor with three-phase power. Using the rotor angle determined by a sensing element integrated into the PMSM, The PMSM's phase currents are mapped and measured relative to a rotational reference frame. Motor phase currents are regulated by keeping the d-axis current at zero and the q-axis current at a value high enough to issue the reference torque at all speeds below or equal to the rotor speed.

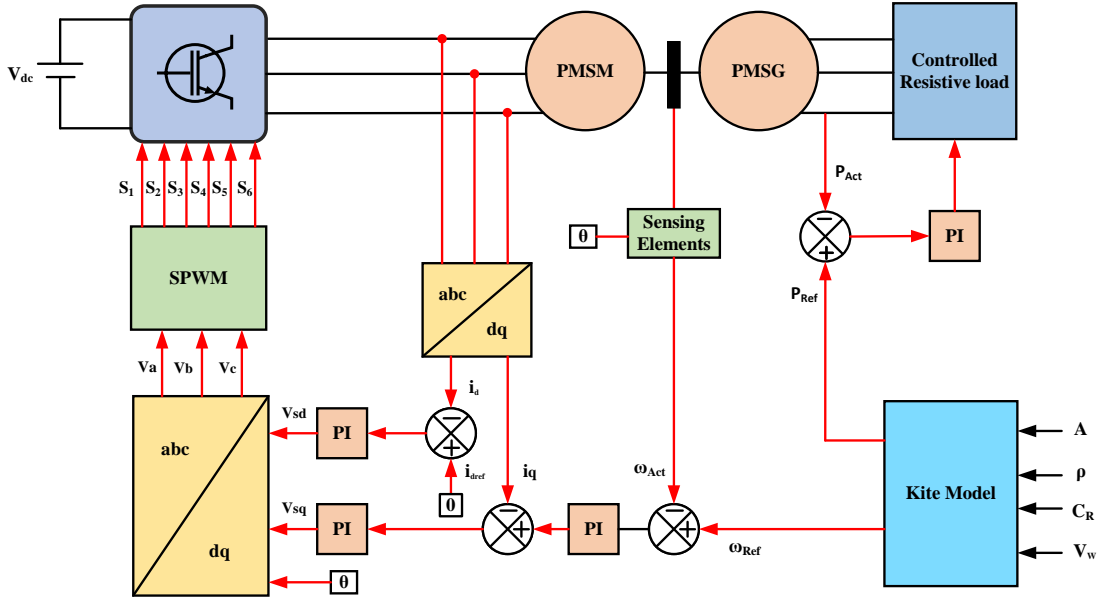


Figure 3.8: Control mechanism of proposed KPS emulator.

The generator, which is also a permanent magnet synchronous machine, is coupled to the emulator, and the load, which is a regulated resistive load, is managed by the load controller. In the outer loop for speed control, the reference speed (ω_{Ref}) value is compared with the actual speed (ω_{Act}) value and determines the error in the calculated speed. In the current-feedback loop, the speed deviation is amplified proportionally and integrally before being denoted as the quadrature-axis current. The size and polarity of the reference current define the direction and magnitude of the torque produced by the PMSM. The torque generated by the synchronous permanent magnet motor now causes the rotational speed to approach the nominal value. Putting the reference of the direct-axis current controller at zero allows for independent control of torque along the q-axis current.

Speed control loop of field or depicted in Figure 3.9; error in measured speed is calculated by comparing reference speed (ω_{Ref}) with actual speed (ω_{Act}). The speed error is amplified proportionally and integrally before being sent into a current-feedback loop, where it is known as the quadrature-axis current.

Figure 3.10 shows the output electrical power control loop, the reference kite power (P_{Ref}) value is compared with the actual electrical output power of PMSG (P_{Act}) value and determines the error in the measured electrical power. Once the

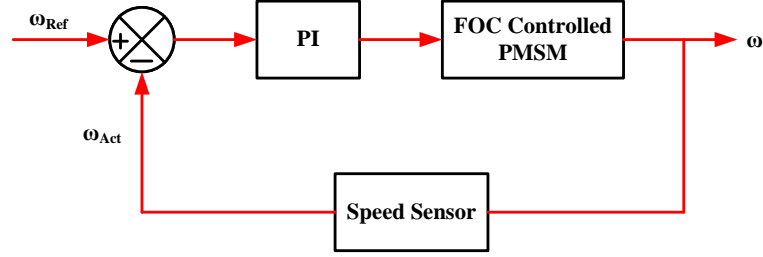


Figure 3.9: Motor speed controller loop.

output power error has been amplified proportionally and integrally, it is sent to the power-feedback loop, where it is known as the electrical load power.

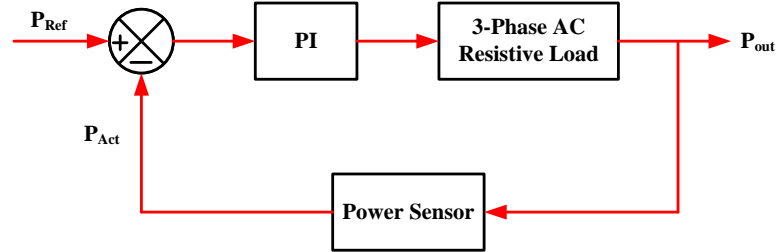


Figure 3.10: Load controller loop.

Table 3.1 represents the system parameters for the simulation of KPS as shown in the table below:

Table 3.1: The KPS emulator parameters of three different test cases .

Parameter	1 kW	10 kW	100 kW
Kite Area	2.5 m^2	14 m^2	60 m^2
Aerodynamic Coefficient, C_R	1.125	2.875	3.825
Wind Speed	2 - 12.25 m/s	2 - 12.25 m/s	2 - 12.25 m/s
Air Density	1.225 kg/m^3	1.225 kg/m^3	1.225 kg/m^3
Rated Voltage of Machines	415 V	415 V	415 V
Rated Speed of Machines	1500 rpm	1500 rpm	1500 rpm
Pole Pairs of Machines	4	4	4
Rated Current of Machines	1.5 A	14 A	135 A
Maximum Torque of Machines	6 Nm	65 Nm	630 Nm

3.2.5 Comparison with Conventional Wind Turbine

Commercialization of KPS mainly depends on its scalability and also capacity factor. The KPS and the CWTs both generate energy from the wind, but they differ in their design and operation. A distinct feature of KPS is that it can

generate electricity at higher altitudes, where the wind is strong and consistent. This can make the KPS more efficient than the CWTs, which are limited by the height of the blades. The mechanical power (P_m) developed by a CWT is given by [Kim et al., 2012],

$$P_m = \frac{1}{2} \rho \pi R^2 C_p(\lambda, \beta) v_w^3 \quad (3.31)$$

where ρ is the air density, R is the radius of the area swept by the turbine, and C_p is the power coefficient which is the ratio of mechanical power to the power in the wind. C_p is a function of Tip Speed Ratio (TSR) denoted by λ and the pitch angle of the turbine blade β . The λ is calculated as tip speed divided by the wind speed.

The mechanical torque T_m developed by the CWT is given by [Yan et al., 2013],

$$T_m = \frac{1}{2} \frac{\rho \pi R^3 C_p(\lambda, \beta) v_w^2}{\lambda} \quad (3.32)$$

The value of C_p varies non-linearly with λ and β and varies with respect to the turbine design. From the equations 3.31 and 3.32, we can infer that by knowing the values of v_w , λ , and β we can evaluate the mechanical torque developed by the turbine. As the KPS operates in pumping mode, maximum power generated in a cycle of operation P_{cyl} which includes power generated during tether reel-out P_{rout} and the power spent during the reel-in P_{rin} of the kite is given by,

$$P_{cyl} = P_{rout} - P_{rin} \quad (3.33)$$

Table 3.2 shows the data used for the comparison of KPS with CWT which is taken from the literature [De Lellis et al., 2016]. From table 3.2 we can observe that a KPS with a projected area of 270.9 m^2 attains the rated power at 7.3 m/s which is much lesser than the CWT making it suitable for low wind profile regions. The maximum power from the KPS is limited to 1322 kW which is due to the power consumed in the reeling-in of the kite. The capacity factor of the KPS is 45.59% as compared to 31.36% of CWT, indicating 45% more average power production from KPS plant as compared to CWT plant.

3.3 Simulation Results and Discussion

This section discusses the results of KPS under no-load and with an AC resistive load conditions. The KPS emulator presented in the block diagram (Figure 3.8) is implemented and simulated in MATLAB/Simulink, and the results are shown considering variable wind speed from 2 m/s to 12.25 m/s . The plots of the kite

Table 3.2: Specifications of KPS and CWT [De Lellis et al., 2016]

Parameters	KPS	CWT
Nominal Power (P_{nom})	2MW	2MW
Specifications	Wing span = 36.8 m	Hub height = 78 m
	Projected Area = 270.9 m^2	Blade length = 43 m
	Tether diameter = 3 cm	Area swept = 5808.0 m^2
	Reel-out length = 230 m	TSR = 6.7
	Max tension = 56.09 ton	$C_p = 0.43$
Rated Wind Speed at P_{nom}	7.3 m/s	9.8 m/s
Max Power	$P_{cyl,max} = 1322$ kW	$P_{max} = 2$ MW
	$P_{rout} = 2$ MW	
	$P_{rin} = 678$ kW	
Average Power (P_{avg})	911 kW	627 kW
Capacity Factor (C_F)	45.59 %	31.36 %

dynamics, power converter output, PMSM output, and the PMSG output parameters are discussed in detail.

3.3.1 No-load Test

Figure 3.11 shows the simulation results of KPS emulator under no-load condition using the data shown in Table 3.1. Figure 3.11a depicts the motor speed at no load, which varies between 253.54 rpm to 1500 rpm, the minimum and maximum speeds of the motor, which is the same as the motor's reference speed. Figure 3.11b represents the generator voltage, which changes from 68 V to 133 V in 0 to 2 seconds and 334 V to 400 V in a period of 8 to 10 seconds at the corresponding wind speed. Figure 3.11c is a zoomed section of Figure 3.11b, which shows the three-phase voltage of the generator. From the no-load analysis, the FOC control of the PMSM is validated, which follows the reference speed from the kite model.

3.3.2 On-load Test

Figure 3.12 shows the KPS simulation results with AC resistive load analysis at the PMSG terminal using the parameters shown in Table 3.1. Figure 3.12a depicts the variation in motor current, which changes according to the load torque. Motor current varies from 2.64 A to 33.45 A, which is the minimum and maximum current of the motor from period 0 to 10 seconds at wind speeds of 2 m/s to 12.25 m/s respectively. Figure 3.12b shows the enlarged form of motor current, which is depicted in figure 3.12a. Figure 3.12c represents the motor input power, which is the motor's electrical power. It varies from 33 W to 6950 W with a time variation from 0 to 10 seconds at wind speeds of 2 m/s to 12.25 m/s, respectively.

Figure 3.12d shows the torque variation, with the blue waveform representing

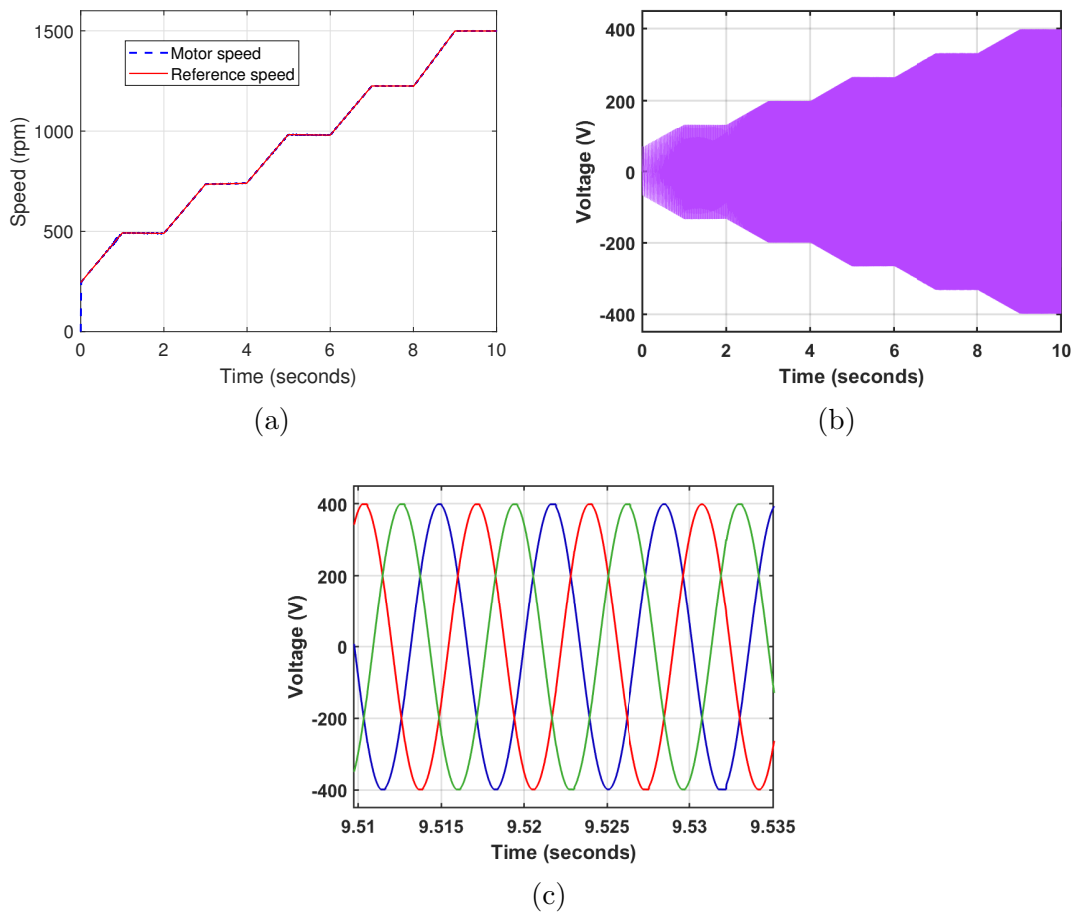


Figure 3.11: No load analysis at generator terminal: (a) No load speed of coupled machines, (b) No load generator voltage, and (c) No load generator voltage(zoomed view).

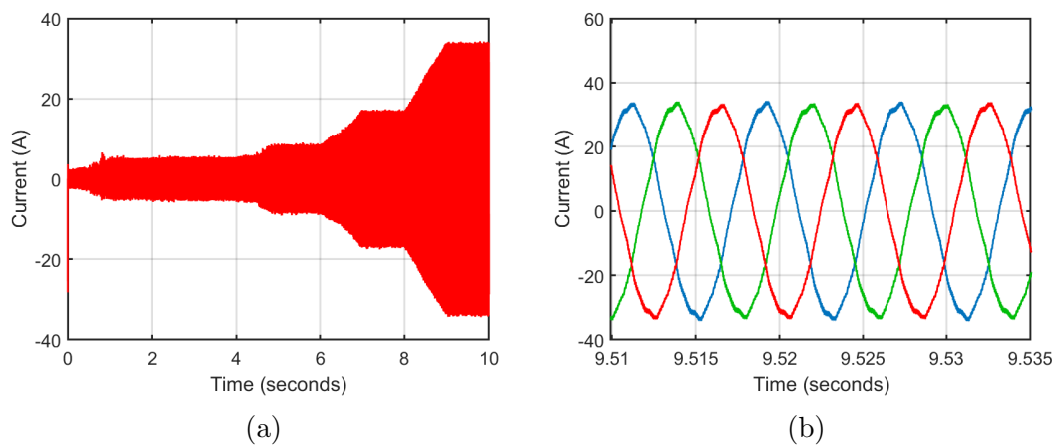
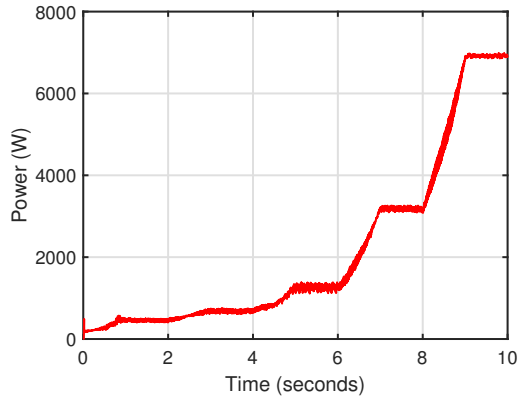
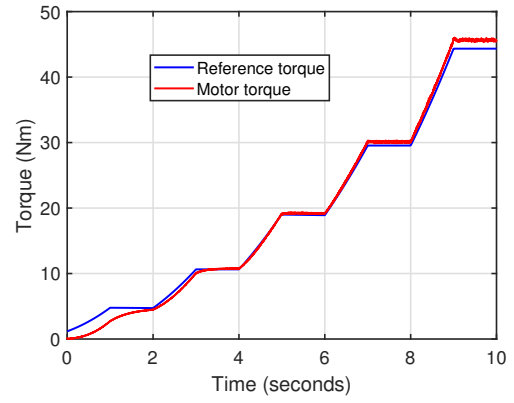


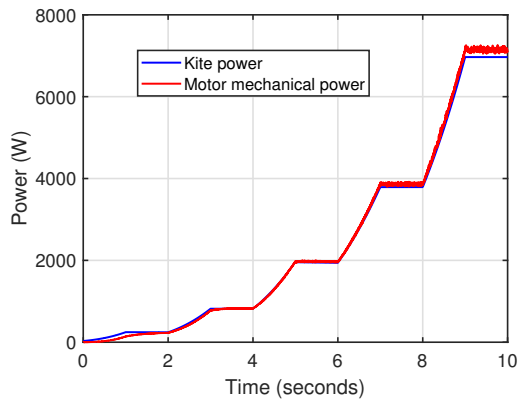
Figure 3.12: Simulation result: (a) Motor current, (b) Motor current(zoomed view),



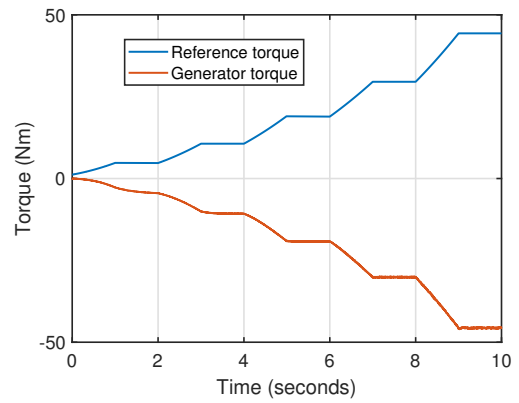
(c)



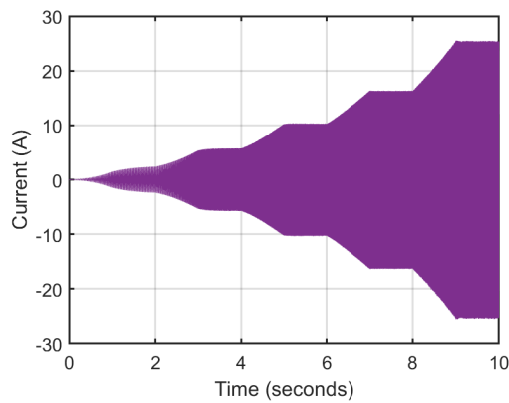
(d)



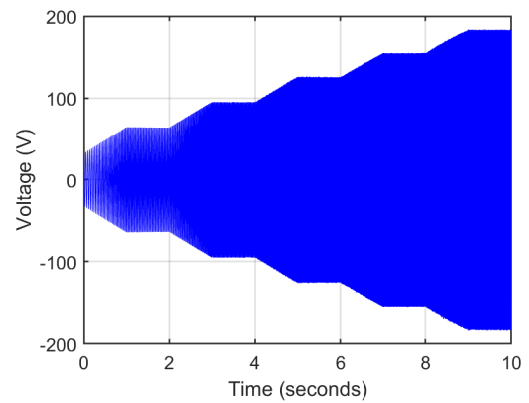
(e)



(f)

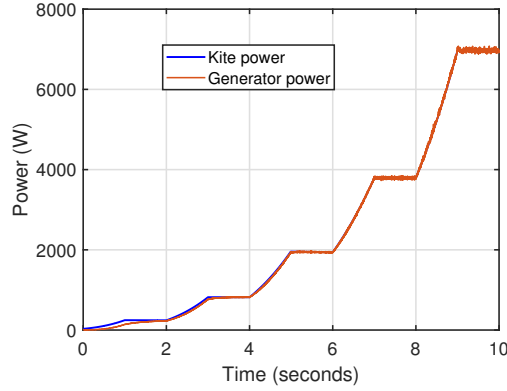


(g)



(h)

Figure 3.12: Simulation result: (c) Electrical power of the motor, (d) Couplings torque, (e) Couplings power, (f) Generator torque, (g) Generator AC current, (h) Generator AC voltage.

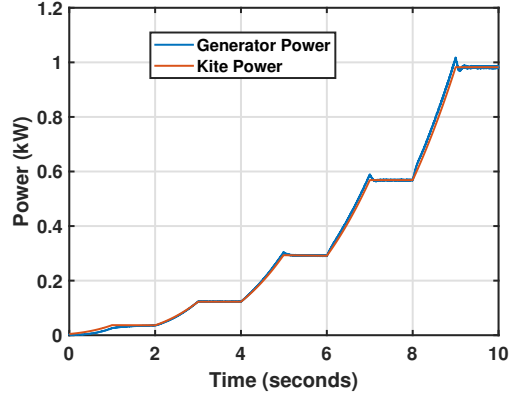


(i)

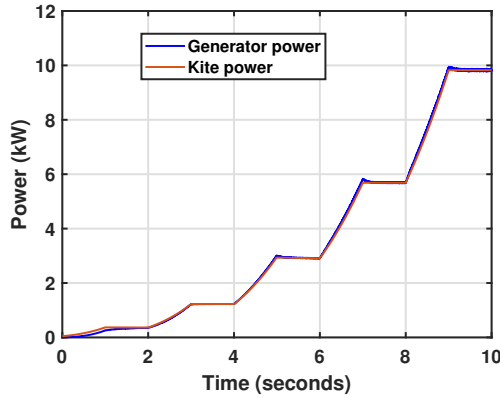
Figure 3.12: Simulation result: (i) Generator output power.

the kite torque and the red waveform representing the motor torque. It varies from a minimum torque of 1.27 Nm at 2 m/s of wind speed and a maximum torque of 45 Nm at 12.25 m/s of the period of 0 to 10 seconds, which follows the motor reference torque. The motor and generator coupling power is depicted in 3.12e. It changes from 33 W to 7000 W, with a corresponding wind speed of 2 m/s to 12.25 m/s, which precisely follows the reference power of the kite. Figure 3.12f shows the generator torque, which is the negative of motor torque. It changes from -1.27 Nm to -45 Nm at wind speed varies from 2 m/s to 12.25 m/s. Figures 3.12g show The generator's current, which changes from 0 A to 27 A and corresponding wind speeds from 2 m/s to 12.25 m/s, respectively. Figures 3.12h show The generator's AC voltage, which changes from 68 V to 198 V, and the corresponding wind speed from 2 m/s to 12.25 m/s, respectively. figure 3.12i depicts the generator's electrical power output. The load test analysis of the KPS emulator system shows the performance of the proposed PMSM-based emulator for varying load demands with the speed and torque reference values from the kite model.

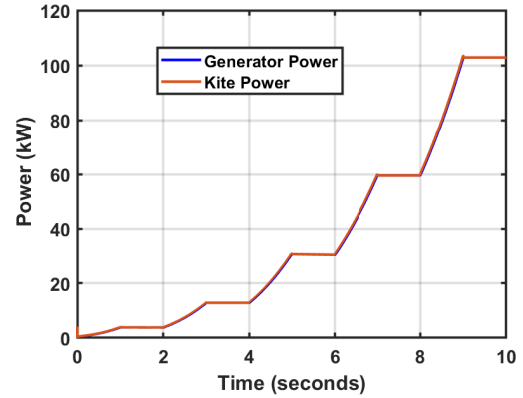
In this study, KPS with three different power ratings, 1 kW, 10 kW, and 100 kW are simulated with the resultant aerodynamic coefficient C_R of 1.125, 2.875 and 3.825, respectively, at the generator terminal as shown in Figure 3.13. The kite's area depends on the airfoil's design and the rated wind speed. The ratings of the designed KPS for three power ratings are shown in 3.1. Figures 3.13a, 3.13b, 3.13c show the performance of the 1 kW, 10 kW, and 100 kW emulator system respectively. The analysis of various power ratings shows that the KPS emulator can be used to test the scaled-up version of the system under varying load conditions, which is crucial in analysing the performance of KPS prior to the development of the actual system.



(a) 1 kW



(b) 10 kW



(c) 100 kW

Figure 3.13: Electrical power output at the generator terminal of three different test cases: (a) 1 kW, (b) 10 kW, and (c) 100 kW

3.3.3 Field Test Data Analysis

The kite flight data collected from the field test is used to estimate the force. The tether force, along with the kite's figure-eight trajectory data were recorded through several experiments. The raw data from the field testing are shown in table 3.3 and include the kite orientation information (Yaw, Pitch, Roll), the kite's altitude in meters, the force measured by the load cell (analog value), wind speed (in m/s), and the wind direction (in degrees). The wind direction is recorded with respect to the east-direction axis.

We may write the C_L and C_D equations as

$$C_L \approx 2\pi(\dot{\theta} - \beta) \quad (3.34)$$

$$C_D \approx 1.28.(\sin(\dot{\theta}) + \cos(\beta) + \cos(\phi')) \quad (3.35)$$

Where β is the angle made by the kite with respect to the wind direction vector and is calculated as $|\chi - \psi|$ [Castelino et al., 2022]. The χ is the angle

Table 3.3: Field test data used in the simulation: sample data of 10 data points.

Data Point	Yaw (Degrees)	Pitch (Degrees)	Roll (Degrees)	Altitude (m)	Tether Force (N)	Wind Speed (m/s)	Wind Direction (Degrees)
1	50.68	-131.76	48.03	1.9	481	3.58	17
2	48.37	-135.88	52.03	2.4	485	3.53	14
3	45.94	-143.90	54.68	4.9	453	3.55	9
4	47.20	-147.42	54.78	5.9	464	3.60	8
5	48.21	-149.27	46.20	7.1	467	3.60	11
6	52.36	-151.14	35.22	8.1	450	3.63	13
7	54.88	-155.88	29.09	10.2	372	3.63	6
8	56.07	-156.77	25.46	10.6	283	3.68	6
9	54.80	-160.40	25.39	12.2	255	3.70	15
10	53.56	-166.97	27.68	13.8	211	3.65	12

made by the wind direction vector with respect to the east direction vector and ψ is the angle made by the kite with respect to the east direction vector.

Figure 3.14 depicted the kite's flight path in the experimental field. As the kite moved in a figure-eight trajectory, the force changes according to the position. The kite trajectory was plotted using GPS data received during the field test. Figure 10a depicted the Yaw vs Force, Figure 10b shows the Roll vs Force, and Figure 10c shows the pitch vs Force, which shows the corresponding YRP angles during the kite's trajectory.

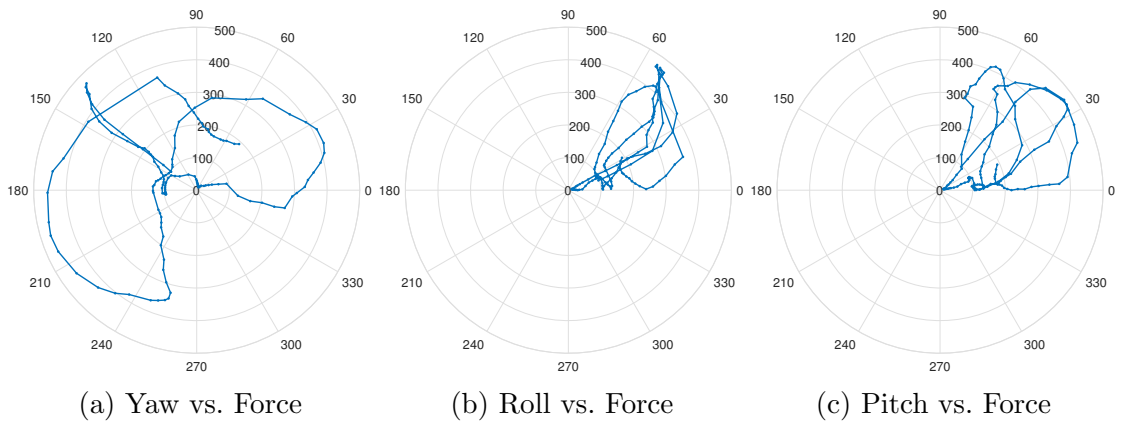


Figure 3.14: Polar plot of kite flight path test (a) Yaw vs. Force. (b) Roll vs. Force. (c) Pitch vs. Force. Adopted from [Castelino et al., 2022]

3.3.4 Simulation using the satellite data

The pictorial representation of satellite-derived wind data is shown in Figure 3.15 & 3.16 for the National Institute of Technology Karnataka (NITK) beach location at a height of 10 m and 50 m respectively. NITK is situated in the Dakshina Kannada district of Karnataka state in India. The aforementioned satellite wind analysis is shown for two levels of height 10 m and 50 m. Figures 3.15a and 3.16a

show the wind speed and direction for 12 months of the year 2022 at 17:00 IST, whereas Figure 3.15b and 3.16b represents the wind speed and direction for 24 hours of August month's wind profile. Finally, we get most of the wind speed and direction variation from the plot towards the south-east direction, and wind speed varies from 2 m/s to 8 m/s.

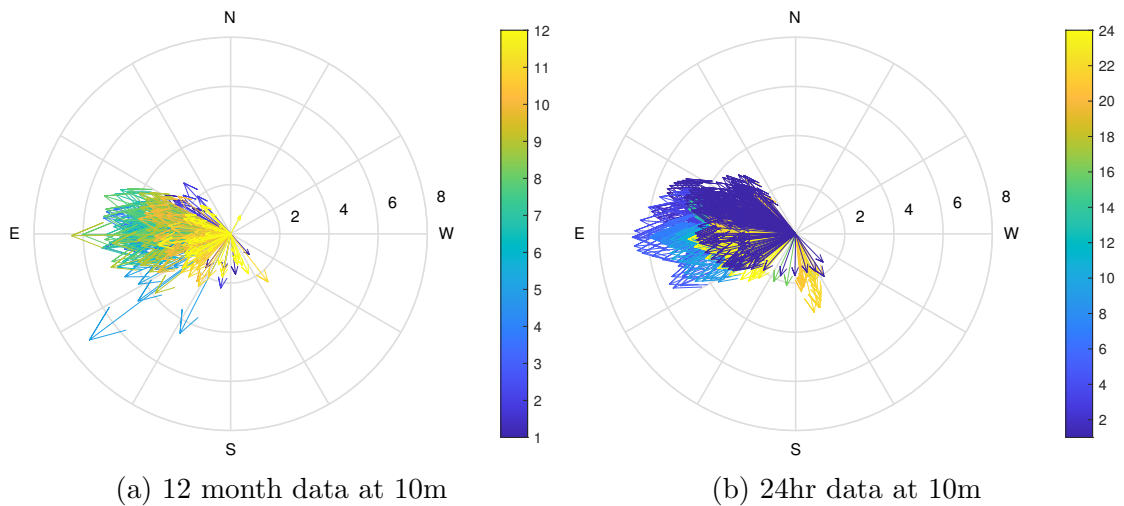


Figure 3.15: Wind data from satellite: plot (a) shows the wind profile for 12 months at 17:00 IST, at 10 m height, respectively, and plot (b) shows 24 hours of wind profile of August month, at 10 m height.

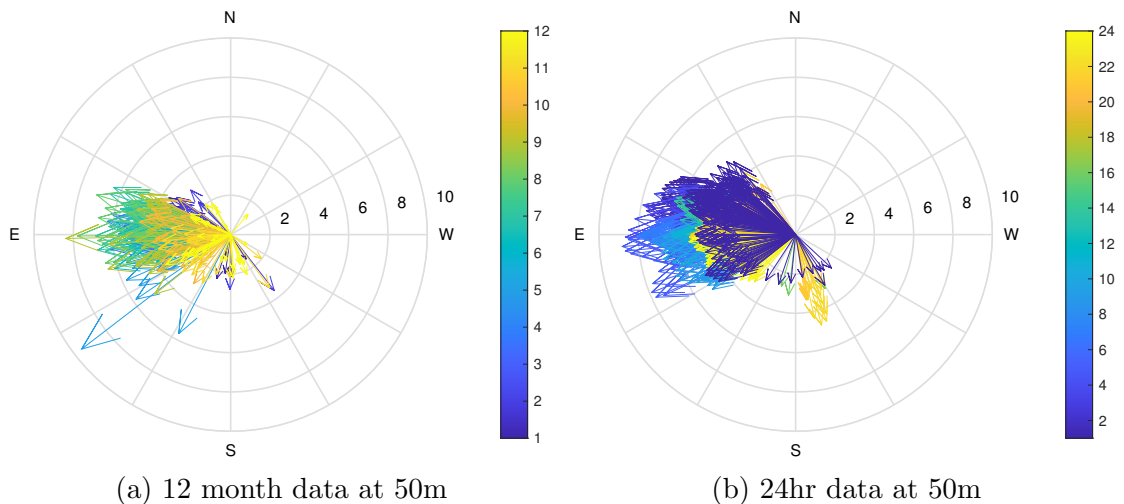


Figure 3.16: Wind data from satellite: plot (a) shows the wind profile for 12 months at 17:00 IST, at 50 m height, respectively, and plot (b) shows 24 hours of wind profile of August month, at 50 m height.

Figure 3.17 shows the power generation plot from hourly satellite wind data at 50 m height from the ground and takes 50 wind data samples in the month of August which is simulated in the KPS model and shown in simulation results

below. Figure 3.17a shows the wind speed variations from 2.75 m/s to 6 m/s. Figure 3.17b shows the motor speed in rpm, and it varies from 325 rpm to 730 rpm. Figure 3.17c shows the kite power in watts, which varies from 95 W to 830 W and Figure 3.17d shows the generator power in watts, which changes from 95 W to 820 W which is exactly matching with kite generated power. Figure 3.18 shows the power generation plot from hourly satellite wind data at 50 m height from the ground.

From the satellite data, fifty wind data samples in the month of August are simulated in the KPS model and shown in simulation results. Figure 3.18a shows the wind speed in m/s, it varies from 1.9 m/s to 4.75 m/s. Figure 3.18b shows the motor speed in rpm, and it varies from 230 rpm to 582 rpm. Figure 3.18c shows the kite power in watts, which varies from 34 W to 392 W and Figure 3.18d shows the generator power in watts, which changes from 34 W to 392 W which is exactly matching with kite generated power.

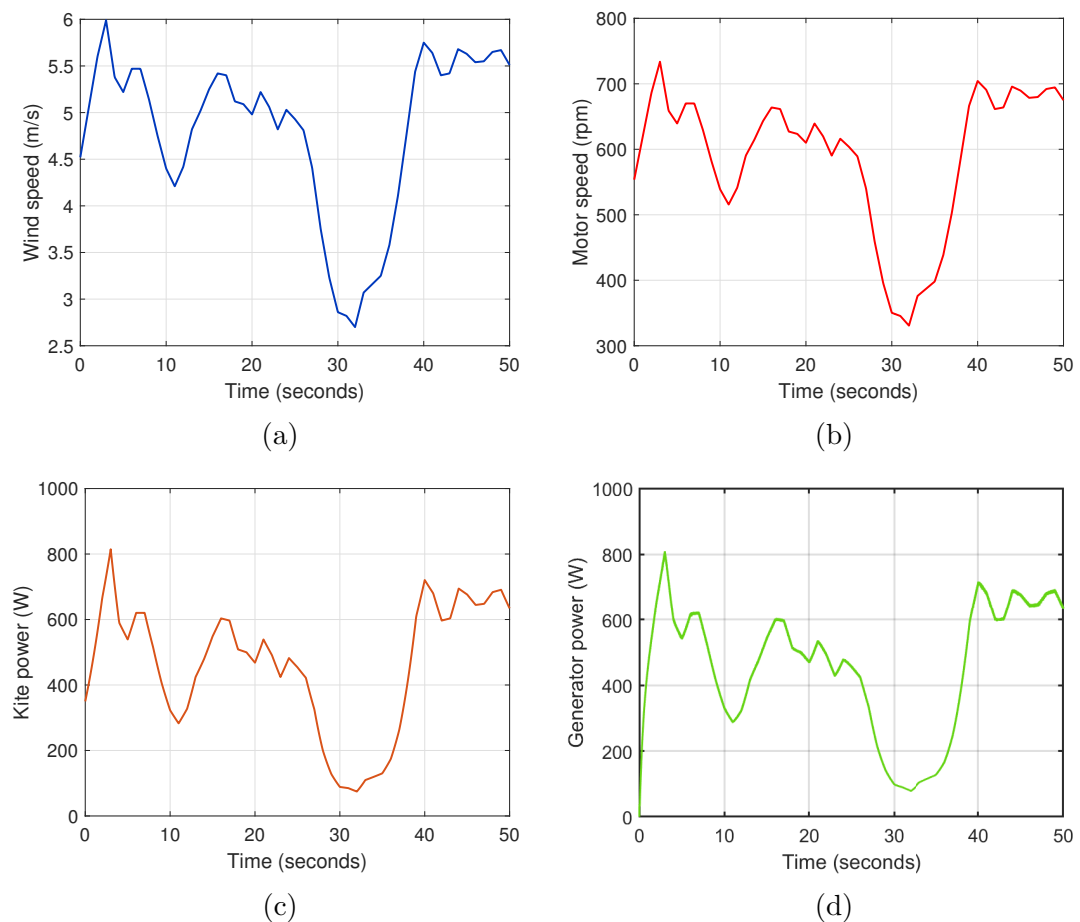


Figure 3.17: Plots using hourly satellite wind data at 50 m height from the ground: (a) wind speed (b) motor speed, (c) estimated kite power from physical model, and (d) generator electrical power.

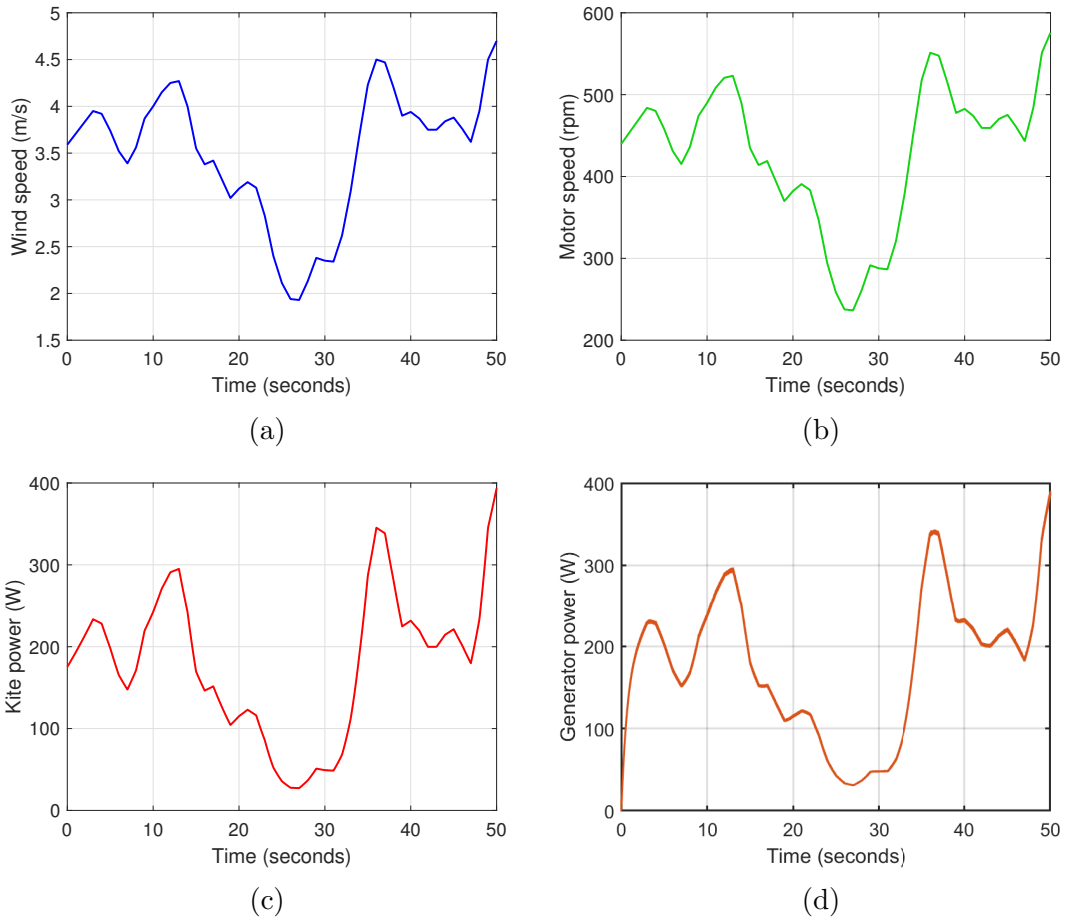


Figure 3.18: Power generation plot from hourly satellite wind data at 10 m height from the ground: (a) wind speed (b) motor speed, (c) estimated kite power from physical model (PM), and (d) generator electrical power.

3.3.5 Verification using experimental data

Figure 3.19 shows the ground data simulation results of motor speed, measured kite power from a field test, estimated kite power from a physical model, coupling/mechanical power, and generator electrical power. The recorded data from the field testing was used to estimate the power. Data from the kite's figure-eight trajectory was recorded alongside the wind velocity and tether force in a series of experiments. Figure 3.19a depicted the experimental wind speed, which changes a minimum of 3.15 m/s and a maximum of 4.65 m/s.

Figure 3.19b shows the motor reference speed with a 1:5 gear ratio, which changes minimum values of 387.255 rpm and maximum value of 570 rpm. Figure 3.19c shows the measured kite power from the field test, which varies with a minimum of 174 W and a maximum of 674 W at sample times 36 and 26 seconds, respectively. Figure 3.19d shows the estimated kite power from the physical model, which varies with a minimum of 100 W and a maximum of 675 W at sample times 13 and 24 seconds, respectively. Figure 3.19e shows the coupling or mechanical

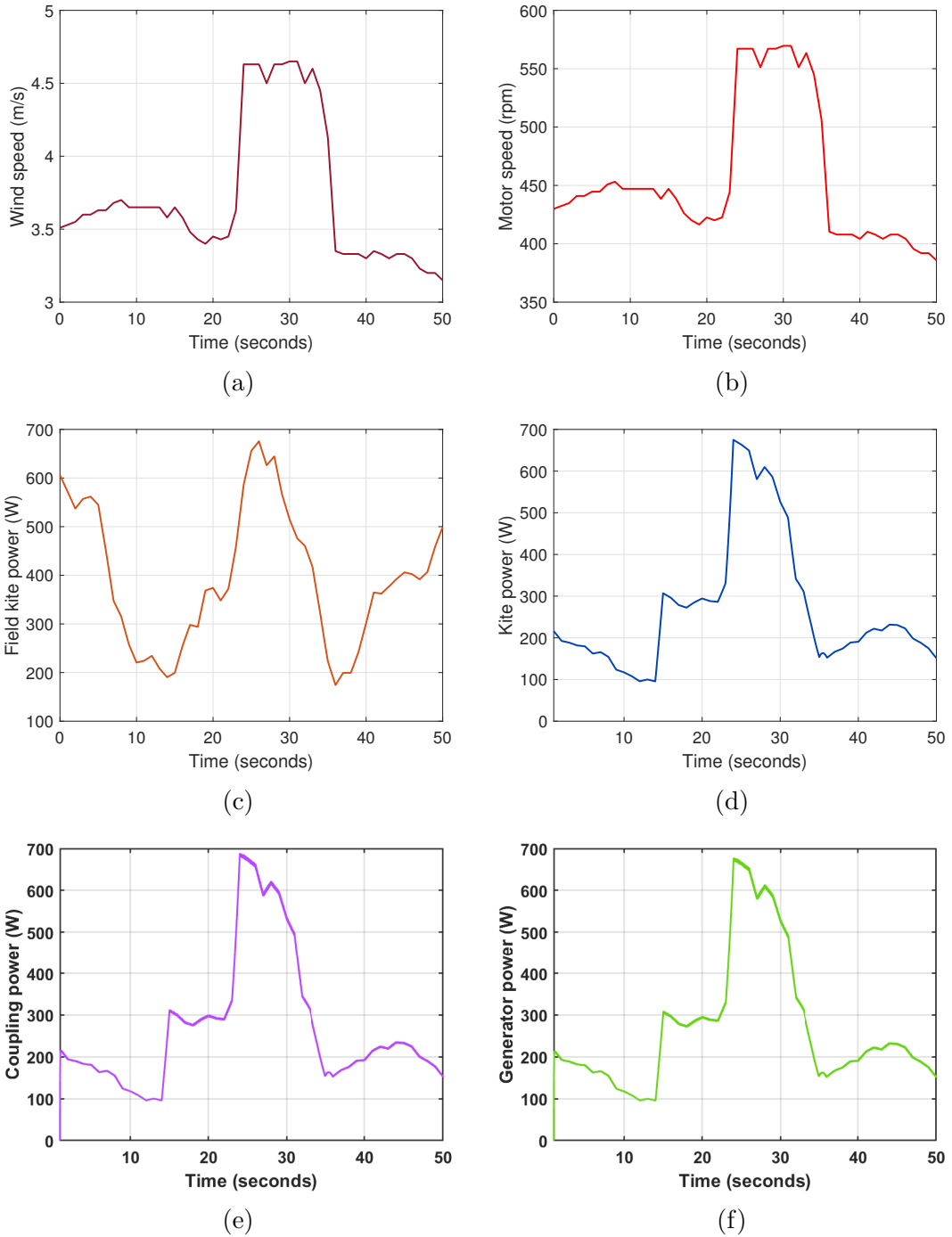


Figure 3.19: Simulation using experimental data (a) Wind speed, (b) Motor speed, (c) Measured kite power from a field test, (d) Estimated kite power from the physical model, (e) Coupling/Mechanical power, and (f) Generator electrical power.

power of permanent magnet of synchronous machines, which varies with a minimum of 100 W and a maximum of 690 W at sample times 13 and 24 seconds, respectively. Figure 3.19f shows the emulator electrical power at the permanent magnet synchronous generator terminal or resistive load terminal, which changes with a minimum of 100 W and a maximum of 675 W at sample times 13 and 24 seconds, respectively. It is precisely the same as the estimated kite power from the physical model.

3.3.6 Discussion and Applications

The study's results discussed in the chapter contains crucial outcomes for emulating kite-based power generators for scaling up the system. The PMSM-based drive provides the required response to the variables provided by the kite model. For a power range of 100 kW, a 60 m^2 kite is necessary with a resultant aerodynamic coefficient of 3.825. As the kite-based wind power generation system has variable speed and variable frequency output at the generator, the PMSM is preferred over DC and induction generators [Bansal et al., 2002]. A 3-phase PMSG is used in this analysis which can be driven with the required speed and torque characteristics using the feedback loops the kite model requires. As a standalone application, a PMSM is preferred over other AC generators [Spooner and Williamson, 1996] as the field is produced by the permanent magnets, which do not need an external source to excite the machine [Pereira and Sousa, 2022]. Three methods in this simulation generate the variations in the wind speeds - using a signal builder, satellite data of the site, and experimental data from the field tests. The potential application of this technology is as a standalone power generation unit in a region where conventional wind turbines are not practical. The kite-based power generators can be installed in remote locations where the utility grid is unavailable [Reuchlin et al., 2023]. The kite power system, in combination with the battery storage system [Mittal et al., 2010] can also be employed in remote locations where an uninterrupted power supply is necessary [Ilyushin and Afanaseva, 2019, Afanaseva and Ilyushin, 2018]. From the simulated graphs, we can understand the system's dynamics for a specific wind profile, and a kite-based system can be designed based on the requirements.

3.4 Summary

The research described in this chapter contributes to the study of power emulation in a commercial-scale Kite Power System (KPS). A KPS emulator is designed and simulated to mimic an actual KPS drive train in a controlled testing environment. In this research work, we have studied the KPS emulator with PMSM, driven by a Field Oriented Control (FOC) technique. A three-phase power inverter drives the PMSM with a PI current controller operating in a closed loop. We have validated the emulator results with the experimental field test data of the kite. The key outcomes of this research are listed below:

- The KPS emulator based on FOC-controlled PMSM offers precise control over speed and torque, which can mimic the kite characteristics accurately.
- The KPS emulator offers a wide range of kite sizes at varying wind speeds, which can help researchers to realise the system prior to implementation to study the dynamics of the system.
- The proposed KPS emulator was simulated with three power ranges of 1 kW, 10 kW, and 100 kW at a kite surface area of 2.5 m^2 , 14 m^2 , and 60 m^2 , respectively at the generator terminal.
- The wind speed varies from 2 m/s to 12.25 m/s for both no-load and full-load rated conditions. We have used experimental ground test data to verify the system and the dynamic behaviour of the generator at no-load and on-load conditions.
- The hourly satellite wind speed data at 10 m and 50 m above the ground is considered in this study with the figure-of-eight data from the field tests to emulate the power generation from KPS. The wind speed data at 50m height with a maximum power of 820 W is generated with a kite area of 10 m^2 at a maximum wind speed of 6 m/s. The wind speed data at the height of 10 m with a maximum power of 392W is generated with a kite area of 10 m^2 at a maximum wind speed of 4.65 m/s
- The comparative study of KPS with CWT of 2 MW power ranges shows that the capacity factor of the KPS is 45.59 % compared to 31.36 % of CWT, indicating 45 % more average power production in KPS which is one of the highest factors in the wind energy industry.

The analysis shows that the kite power derived from the mathematical model satisfies the generated power from the emulation system. The kite's tether force varies throughout the kite's flight trajectory, which needs precise control of the generator shaft speed. PMSM-based emulator system offers promising results for emulating KPS with various sizes of kites and varying wind profiles. The cut-out speed is a critical factor in a wind energy conversion system, and in a KPS, the kite steering unit is used to lower the elevation angles to de-power and land the kite. The future scope of this study will be integrating a kite steering unit with a power emulator. The research work described in this chapter is a step forward in exploiting KPS, making them equally efficient to wind turbines.

Chapter 4

Design of Kite Steer Controller

Contents

4.1	Introduction	61
4.2	Modelling and Control of the Kite	62
4.2.1	Kite Dynamics	62
4.2.2	Kite control method	65
4.2.3	Design of Kite Steer Controller (KSC)	66
4.2.4	Design of Position Controlled Actuators	67
4.3	Method of the kite Steer Controller	67
4.3.1	Roll Pitch Zone (RPZ) Control Method	69
4.3.2	Implementation of the KSC	72
4.3.3	Field Test and Data Analysis	74
4.4	Results and discussions	75
4.4.1	Manual Kite Control Test	76
4.4.2	RPZ Control Experimental Validation	79
4.4.3	Comparative Analysis	83
4.4.4	Power simulation results	83
4.5	Summary	85

4.1 Introduction

The Kite Steer Controller (KSC) is a critical component of the KPS, responsible for the controlled figure-eight manoeuvre of the kite. In this study, a ground-based KSC is designed and developed with a novel Roll-Pitch-Zone (RPZ) method to control the kite. The force from each tether is measured with the power consumption while controlling the kite in a figure-eight trajectory. The KSC is experimentally validated using multiple field test data. The power from the KPS is

simulated using MATLAB coding environment using the experimental data. The net power output, including the power consumption in a figure-eight trajectory, is also explained rigorously. The significant contribution is as follows:

- Design and development of a ground-based kite controller with rapid actuation for the turbulent wind condition.
- A novel control RPZ control method and the experimental validation in steady and turbulent wind conditions.
- The force analysis of the control lines compared to the kite's power lines can be used to estimate the KSC motor for various wind profiles.
- Evaluation of the power consumption of the kite steer controller in a figure-eight trajectory with the variation of force with respect to the figure-eight trajectory.
- The net power generation of the KPS by including the power consumed by the KSC in a figure-eight trajectory.

The outline of the chapter is as follows: the kite dynamics, modelling, and control approaches are explained in section 2, with the design aspects of the kite steering unit. The proposed control algorithm for the autonomous control of the kite and the field test methodology is explained in section 3. Section 4 explains this study's results and discusses the results. Section 5 summarizes the chapter with the key outcomes of this study and the further study needed to improve the proposed methods.

4.2 Modelling and Control of the Kite

4.2.1 Kite Dynamics

The aerodynamic force experienced by the kite depends on the position and orientation of the kite with respect to the wind velocity vector. The position of the kite is represented in the wind reference frame with 'r' as the tether length, θ as the polar angle, and ϕ as the azimuth angle as shown in figure 4.1. The orientation of the kite is represented by the Euler angles (Yaw, Pitch, and Roll) with respect to North-East-Down (NED) reference frame. The kite is steered in figure-of-eight crosswind trajectories. In the figure-of-eight trajectories, the position, orientation, and altitude (h) of the kite changes. The kite is controlled by a Kite Steer Controller (KSC) which steers the kite in a controlled trajectory to maximize the aerodynamic force of the kite.

In figure 4.1, the position of the kite 'K' changes throughout the trajectory of the kite. The azimuth angle ϕ is calculated by the projection of point 'K' on the horizontal plane. The figure-of-eight trajectories are controlled in to the wind direction called as crosswind trajectories. The aerodynamic force of the kite

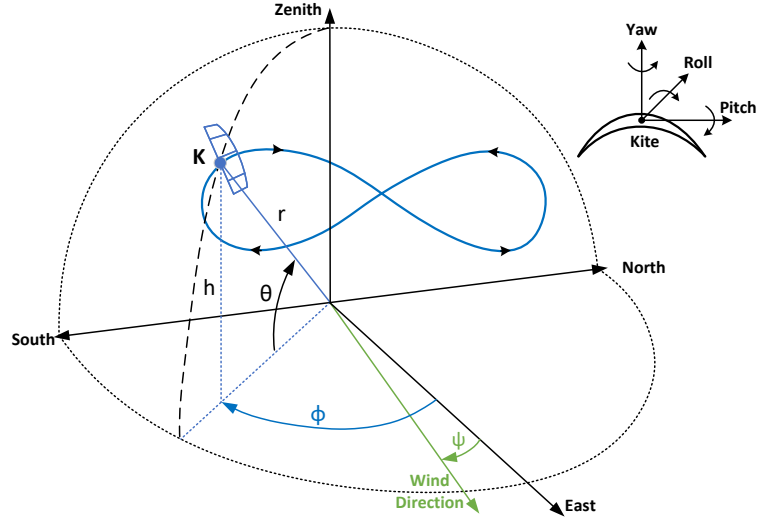


Figure 4.1: The projected position of the kite, 'K' on a half sphere with the radius represented by 'r' with the elevation angle θ and azimuth angle ϕ on a North-East-Down (NED) reference frame. The angle made by the wind velocity vector is denoted as ψ with respect to east. The height of the kite is represented by 'h'.

increases as the polar angle decreases and as the kite operates in smaller azimuth angles [cite]. The yaw, Pitch, and Roll (YPR) of the kite denotes the rotational angles of the kite at a particular position of the kite. The controlled differential movements of control lines of the kite steers the kite in a optimum trajectory.

The total aerodynamic force of the kite depends on the lift & drag of the kite. The lift generated by the kite (F_L) and the drag force (F_D) is given by,

$$F_L = \frac{1}{2} \rho C_L u_a^2 A \quad (4.1)$$

$$F_D = \frac{1}{2} \rho C_D u_a^2 A \quad (4.2)$$

where 'A' represents kite's projected surface area [m^2], apparent wind velocity u_a [m/s], air density ρ [kg/m^3], lift and drag coefficients C_L and C_D are respectively. The apparent wind velocity is the difference between the wind velocity and the kite velocity. The total aerodynamic force can be written as,

$$F_{aero} = \frac{1}{2} \rho C_R u_a^2 A \quad (4.3)$$

where C_R is the resultant aerodynamic coefficient and is given by,

$$C_R = \sqrt{C_D^2 + C_L^2} \quad (4.4)$$

By neglecting the sag in tether for a short tether, the total aerodynamic force from the kite is equal to the tether force. The tether is wound on a spool called as a drum which gets rotated by the unwinding tether to create torque. The drum which is coupled to the shaft of the generator to generate electric power. The total tether force (F_T) experienced by the drum is given by,

$$F_T = F_{centre} + F_{left} + F_{right} \quad (4.5)$$

The forces appearing on the control lines (F_{left} & F_{right}) which is denoted as a net control line force ($F_{control}$) depends on design of the kite and it depends on the geometry of the kite [Jehle and Schmehl, 2014]. The control line forces as a function of total tether force is given by,

$$F_{control} = \delta.F_T \quad (4.6)$$

where δ is control line factor which defines the force on the control lines. For the kite used in this study, the value of δ is 0.23 which is found from the field tests. The torque of the drum with radius 'r' and is given by,

$$T_D = F_T.r.\sin\theta = F_T \times \frac{D}{2} \quad (4.7)$$

where 'D' represents the diameter of the drum and $\sin\theta = 1$ as the angle of tether force with respect to the drum is always right angle. The optimum unwind speed (u_s) is one third of the wind velocity (u_w). Hence, the optimum drum speed (RPM) based on the diameter of the drum is given by,

$$N_D = \frac{u_s}{\pi D} \times 60 = \frac{u_w}{3.\pi D} \times 60 \quad (4.8)$$

We can write the mechanical power developed at the generator shaft as,

$$P_{mech} = T_D.\omega_D = T_D.2\pi\left(\frac{N_D}{60}\right) \quad (4.9)$$

The electrical power generated will depend on the efficiency of the generator and in general, Permanent Magnet Synchronous Generators (PMSG) have an efficiency (η) of 92% to 97%, therefore the electric power generated can be written as,

$$P_{elec} = \eta.P_{mech} \quad (4.10)$$

4.2.2 Kite control method

The kite controller is designed to steer the kite autonomously by imitating the human control method of the kite. The kite controller is designed, developed, and tested based on a 12 m^2 Leading Edge Inflatable (LEI) kite. The kite has four lines on each of its corners. The top two lines are called as the traction lines as they deliver most of the power through them to the ground and the bottom two lines are called as the control lines through which the kite is steered. The kite can be controlled by a human through a control bar. The control bar consists of arrangements which enables the steering of the kite as shown in figure 4.2. The traction lines are connected together and passed through the control bar which is connected to the human operator. The control lines are connected to the left and right extremes of the control bar. The control bar can be pulled which tightens the control lines for more power and the control bar can be pushed away which releases the control lines to lower the power. The kite can be steered to the left by pulling the control bar from the left side only and it can be steered to the right by pulling the control bar from the right end only by using centre point as a pivot.

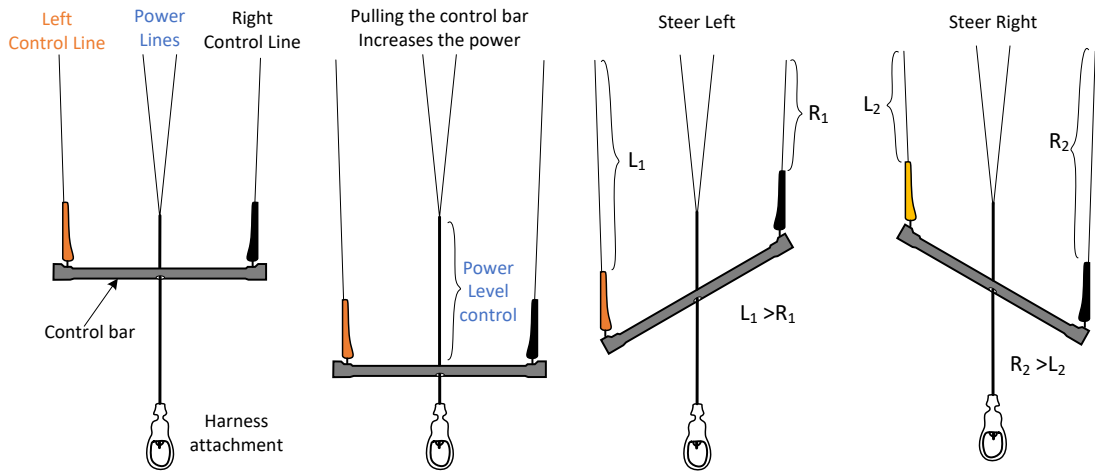


Figure 4.2: Kite control method using kite control bar.

The kite is steered in figure-of-eight trajectory for the extraction of crosswind power. The kite generates more lift when the kite is flying at high speed with lower elevation angle ' θ '. Figure 4.3 shows the significance of figure-of-eight trajectory of the kite. The height of the loop is Δh and the length of the loop is $\Delta\phi$ which affects the net power output in a loop of operation. The kite exerts maximum force when it travels from higher end of the loop to the lower end of the loop as the velocity of the kite increases in the section. The velocity of the kite decreases while turning the kite and the tether force also decreases. In Figure 4.3, a plot of altitude vs azimuthal angle is shown on the right. The loop 1 has the higher altitude which in turn increases the polar angle and reduces the aerodynamic force from the kite while loop 3 exerts more aerodynamic force on the kite as the polar angle reduces. The aerodynamic force of the kite can be adjusted by

adjusting the loop boundaries.

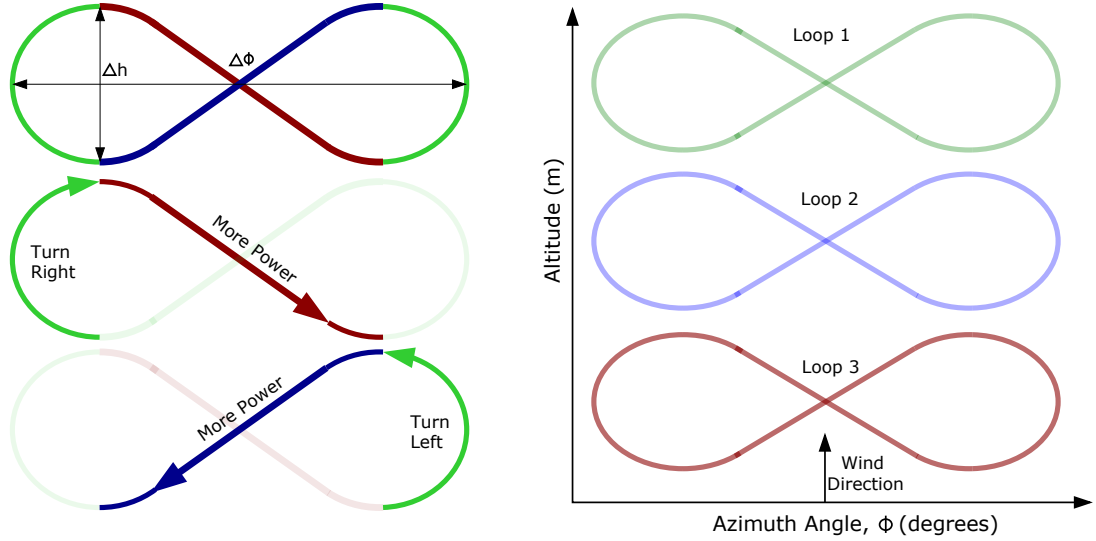


Figure 4.3: Significance of figure-of-eight maneuvers

4.2.3 Design of Kite Steer Controller (KSC)

As discussed in above section, while controlling the kite through a control bar, the control line exerts a tension on the control bar. This tension has to be sustained by the operator to steer the kite which depends on the speed of the kite with respect to wind speed called as apparent wind speed. The tension on the control lines vary from kite-to-kites and also depends also on the geometry and design of the kite [Luchsinger, 2013]. The kite used in this study exerts a maximum tension of 40 kg (about 400 N) on each of the control lines while steering the kite at a wind speed of 6 m/s which is measured in the field tests. The actuation length required by the each of the control lines is 90 cm which is obtained by the length and range of movement of the control bar. The actuation time depends on the apparent wind speed of the kite and in the turbulent winds, the kite turns faster and needs rapid actuation of the line. Therefore, the controller should be able to actuate 90cm under 2 seconds to steer the kite instantly in case of the turbulent winds.

The power ratings of the motors is calculated by the above requirements which is given by,

$$P_{motor} = \frac{Force \times distance}{Time} \quad (4.11)$$

Therefore, $P_{motor_{max}} = \frac{400 \times 0.9}{2} = 180$ W of mechanical power is required from each of the motors. In the electrical form, by accounting a total loss of about 30 % in the form of motor efficiency and converter efficiency, a power rating of 234 W from each of the motors is required to sustain the tension of the control line.

4.2.4 Design of Position Controlled Actuators

The block diagram of the closed-loop position control is shown in figure 4.5. The KSC has two parts, an on-air unit and a ground station. The on-air unit is a sensor system which is mounted on the kite to transmit the kite position, orientation and the altitude data to the ground station. The on-air unit is equipped with battery power source which provides power to the Micro-Controller Unit (MCU), Global Positioning System (GPS), Inertial Measurement Unit (IMU), Altimeter, and the Radio Frequency (RF) Transmitter. The kite is connected to the ground station through three tethers of which center line is composed of two power lines and two control lines. The ground station has a MCU which receives the data through RF receiver and logs the data. The MCU provides the required signals to the motor driver based on the feedback received from the on-air system. The left and right actuators pull & releases the left & right control lines respectively.

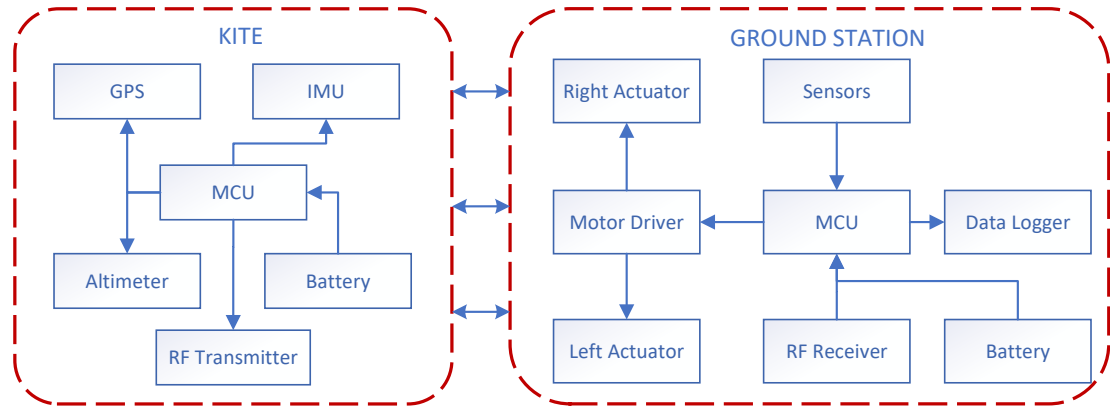


Figure 4.4: Block diagram of the proposed kite steer controller system

Figure 4.5 shows the control diagram of the DC motor drive. The motor drive consists of two loops - the inner loop controls the current and the outer loop controls the position of the DC motor. The current feedback is compared with the reference input and the PI controller applied to get the required duty cycle to protect the motor from excessive load conditions. The position control of the motor is necessary as the kite tether has to be held at a certain length to maneuver the kite. The position of the motor shaft is sensed by the 360 pulse per revolution optical encoder which ensures the motor is at certain position given as input by the user.

4.3 Method of the kite Steer Controller

The orientation of the kite is measured using an IMU which is mounted on the kite. The orientation data is converted in to Euler form for easier understanding of the orientation of the kite during figure-of-eight trajectories. The range of pitch and roll angles are shown in figure 4.6 in which we can observe that, the angle values have both positive and negative sign in a 360 degree rotation. And also, the YPR

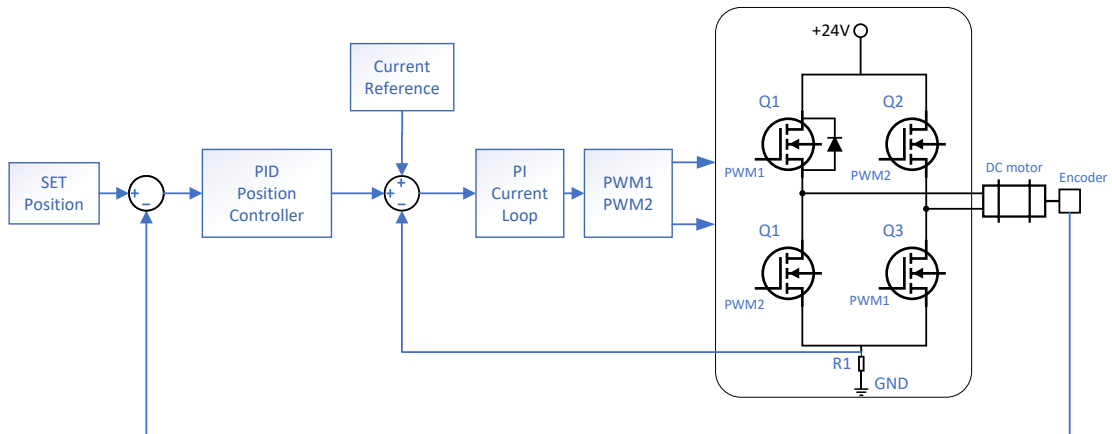


Figure 4.5: Position controlled DC motor drive

representation of orientation depends on the Euler rotation sequence which is XYZ with respect to North-East-Down (NED) reference called as absolute orientation. The XYZ rotation sequence means that the object will be first rotated around X-axis and then around Y-axis and finally around Z-axis. The sign of pitch angle changes when roll angles exceed the limit of the reference frame [Eric Tseng et al., 2007] which is observed in the figure-eight trajectory of the kite.

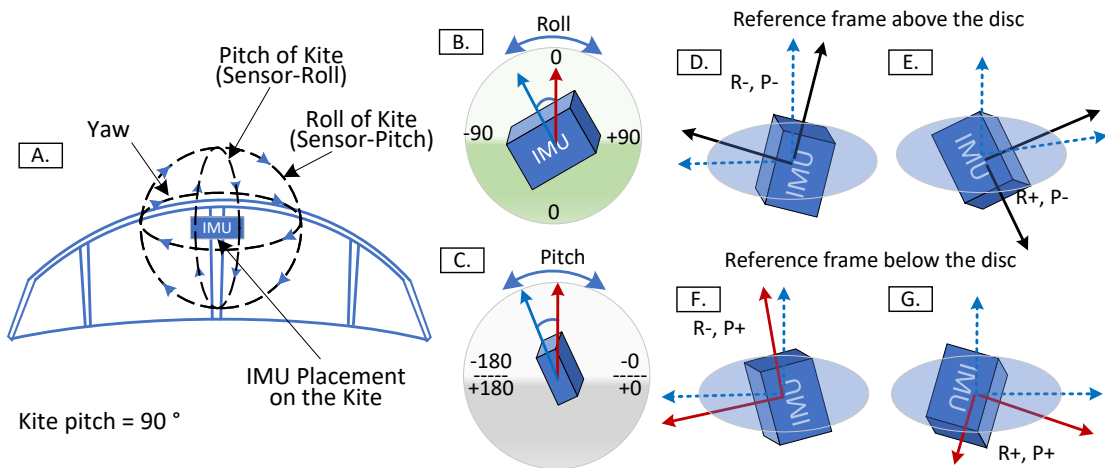


Figure 4.6: Range of YPR angles and the orientation of the kite and IMU

The orientation values tend to get inaccurate when the IMU sensor is oriented upright (nose up) or in straight down (nose down) conditions. To solve this issue, the sensor is oriented in such a way that the sensor pitch represents roll of the kite and the sensor roll represents pitch of the kite as shown in figure 4.6. This reduces the occurrence of 'nose up' and 'nose down' condition in the figure-eight trajectory. The IMU is positioned in such orientating that the sensor pitch varies from -90 degree to -180 degree when the kite position varies from the launch position to the zenith respectively. In figure 4.6, sub-figure A shows the

IMU placement position on the kite, sub-figure B and C shows the range of roll and pitch angles. sub-figure D through G shows the sign changes of the angles when the IMU orientation crosses the centre reference disc.

4.3.1 Roll Pitch Zone (RPZ) Control Method

Figure 4.7 shows the figure-of-eight loop with respect to time. Figure 4.8 shows a plot of roll, pitch, and movement of the kite in terms of latitude with respect to time axis for the same cycle shown in figure 4.7. From both figures, we can observe that when the kite turns left, the sign of pitch angle changes, and also when the kite turns right, the sign of pitch angle changes again. From the several field tests, we observed that by using the orientation data of the kite in terms of YPR, we can estimate the position of the kite in a figure-of-eight trajectory.

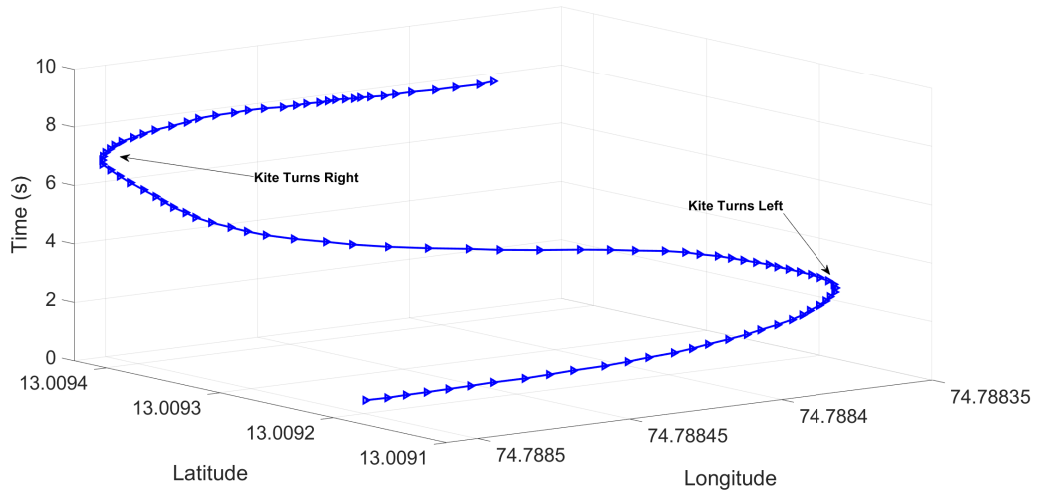


Figure 4.7: Visualization of figure-of-eight trajectory of kite using GPS data

The patterns of roll and pitch changes according to the path of the kite in the trajectory is shown in figure 4.8. While turning the kite, we can observe the sign changes in the roll and pitch value and depending on the logic of the sign changes in roll and pitch values, we have divided the figure-of-eight trajectory into six zones. The transition from one zone to another can be easily tracked using the proposed approach.

Figure 4.9 shows the proposed RPZ method which consists of six zones in which kite can operate. For representation, the zones are equally divided as a two-dimensional figure, the actual area of the zones will vary depending on the trajectory of the kite. The proposed RPZ method uses the feedback from the sensors on the kite and controls the kite. The RPZ method needs the roll, pitch, altitude and GPS coordinates of the kite to steer the kite. The orientation of the kite in the form of Euler angles (YPR) are obtained from the IMU sensor. By the polarity logic of the roll and pitch angles of the kite, the position of the kite

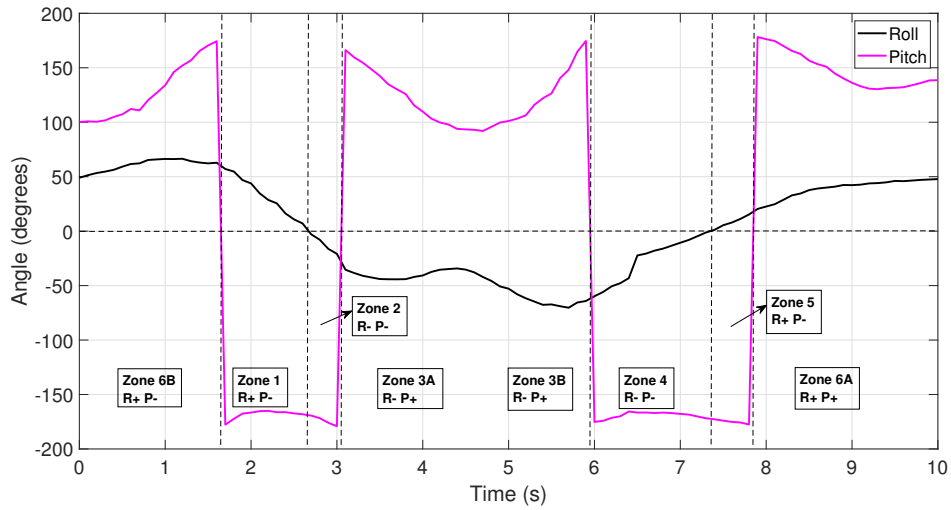


Figure 4.8: Change in the Roll and Pitch values in the figure-of-eight trajectory

in a predefined zone is estimated. The left and right boundary conditions of the figure-of-eight loop are set by the GPS coordinates (latitude & longitude) and the upper and lower boundaries are set by the altitude value.

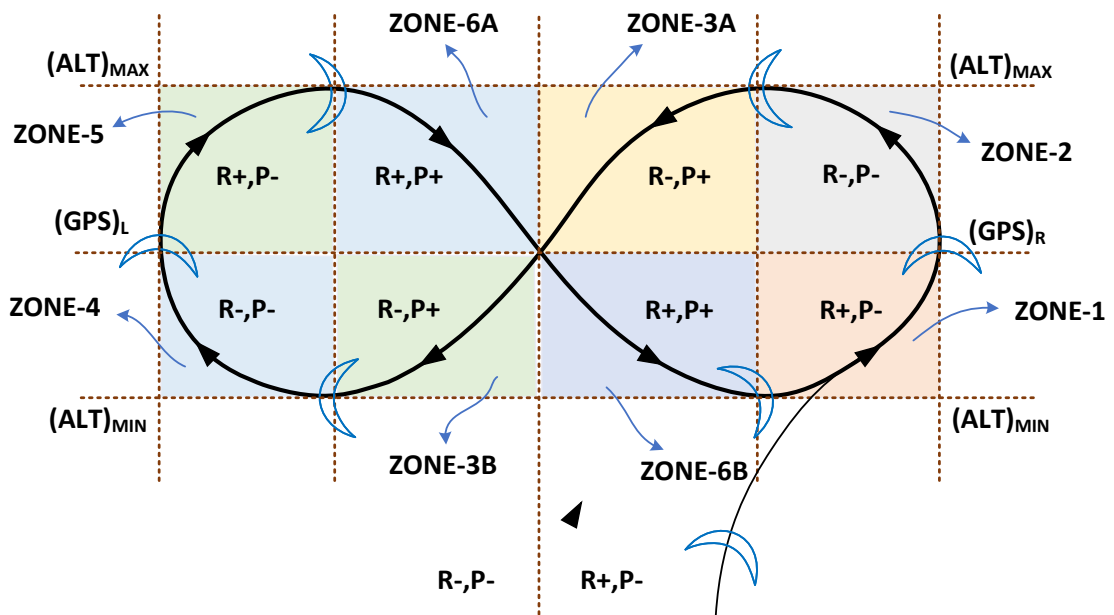


Figure 4.9: Operational diagram of the proposed Roll-Pitch-Zone control method

Figure 4.10 shows the flowchart of the RPZ method. As shown in the flowchart, the kite is launched and the based on the polarity of the roll and pitch the zones are allotted. The flowchart is further divided into four parts, first part consists of kite launching sequence and the second part shows the half cycle of control of the kite. The third part of the flowchart shows the operation of the another half of the figure-eight cycle. The fourth block in the flowchart shows the safety control

of the motor driver and the motor. In the launch sequence, the sensor data is obtained from the sensors mounted on the kite. The kite is launched manually and while the kite achieves the required altitude, the controller algorithm actuates the control lines to keep the kite in upright orientation. Once the kite attains the minimum altitude, the kite is turned slightly to reach the zone 1 in which the sign of roll is positive and pitch is negative, which concludes the launching sequence.

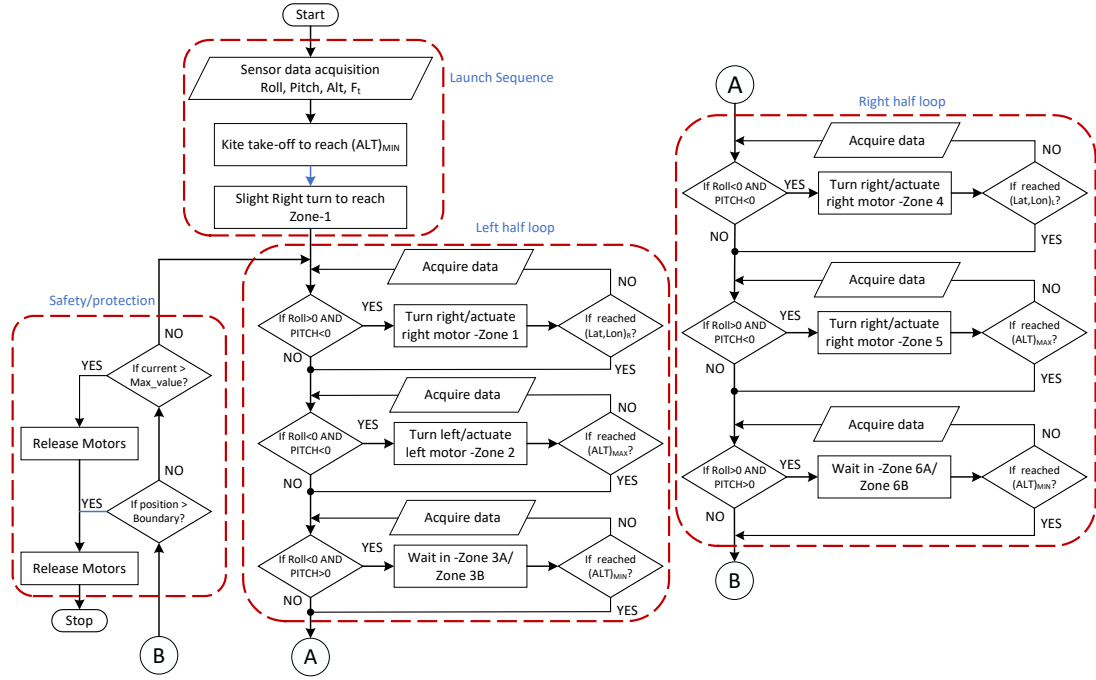


Figure 4.10: Flowchart of Roll-Pitch-Zone control method

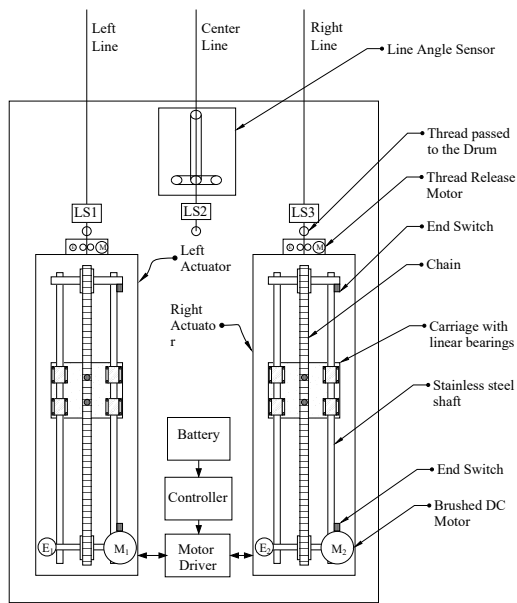
Once the kite is in the zone 1, the kite tends to move to the right side where the right side boundary condition $(Lat, Lon)_R$ is reached. The kite is steered to the left to achieve both signs of roll and pitch to be negative (zone 2). The kite turns left and the program makes sure not to exceed $(ALT)_{MAX}$ condition. When the sign of the pitch changes from negative to positive, the kite transition from zone-2 to zone 3A & zone 3B where the kite experiences maximum aerodynamic force. The kite steering inputs are maintained until it reaches the $(ALT)_{MIN}$ condition. The sign of pitch changes to negative again while the kite makes the transition from Zone 3B to zone 4. The kite is steered to the right to reach the $(Lat, Lon)_L$ condition, the kite transitions from zone-4 to zone-5 in which the sign of roll becomes positive and the sign of pitch remains negative. The kite is steered to turn right and the condition $(ALT)_{MAX}$ is compared with the orientation data received from the kite. Once the polarity of both roll and pitch becomes positive, the kite transitions from zone-5 to zone-6A & zone-6B in which the kite experiences maximum aerodynamic force. The sequence repeats for achieving the figure-of-eight trajectories continuously.

4.3.2 Implementation of the KSC

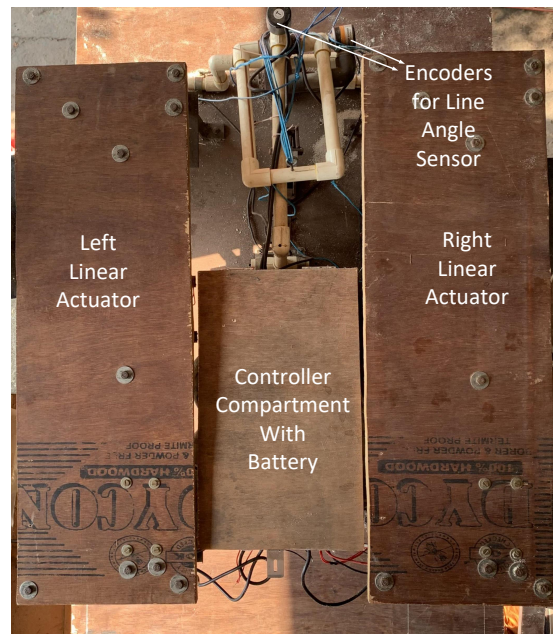
Figure 4.11a shows the design of the kite steering unit which consists of two linear actuators. The left and right control lines of the kite is controlled by each of the linear actuators. The force of the power line, left and right control line is measured by the load cells. The angle made by the line with respect to ground and with respect to the polar angle is measured by a line angle sensor setup. The line angle sensor gives additional feedback to the system for the optimum control of the kite. In the case of RF link disconnection, the kite can be steered using the line angle sensor feedback. Figure 4.11b shows the top view of the developed setup of the kite steering mechanism. The control circuit, data logger, and the batteries are enclosed inside a compartment as shown in the figure to protect against the sand/dust during the field tests.

Figure 4.11c shows the front view of the hardware setup which shows the arrangement of the load-cells to measure the tether tension and line angle sensor arrangement. Figure 4.11d shows the linear actuator mechanism with a carriage which consists of a reel which pulls one of the control lines to steer the kite. The carriage assembly slides smoothly on a stainless steel linear shaft with the help of linear bearings. The DC motor pulls/releases the chain and the chain is attached to the carriage which gets pulled or pushed when the motor rotates clockwise or counter clockwise respectively.

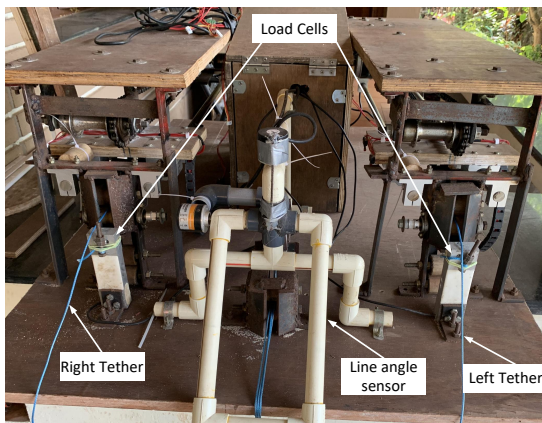
Figure 4.12a shows the side view of the proposed design and figure 4.12b shows the actual implementation of the design. In figure 4.12a, a set of roller arrangement is shown which facilitates the pull and release of the tether when the carriage moves back and forward respectively. When the carriage reaches the end of each side, a mechanical switch is provided for the detection and calibration of the actuator when it is started for the first time. The movement of the carriage is detected by the optical encoder near the motor and the closed loop position controlled motor drive ensures the position is set to the reference position. The tension in the control line is also measured using a load cell arrangement and the line is fixed to a point in case of fixed line operation, and the line is connected to the drum for operating in power generation mode. The technical specifications of the linear actuator is shown in table 4.1.



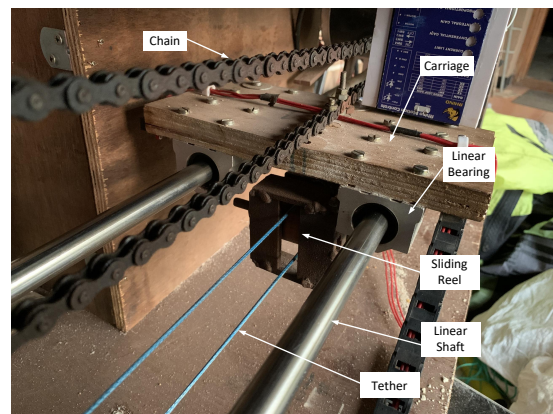
(a)



(b)



(c)



(d)

Figure 4.11: (a) Pictorial representation of the controller (Top view) (b) Top view of the implemented Kite Steering Mechanism (c) Front view of the mechanism (d) Close view of the carriage mechanism

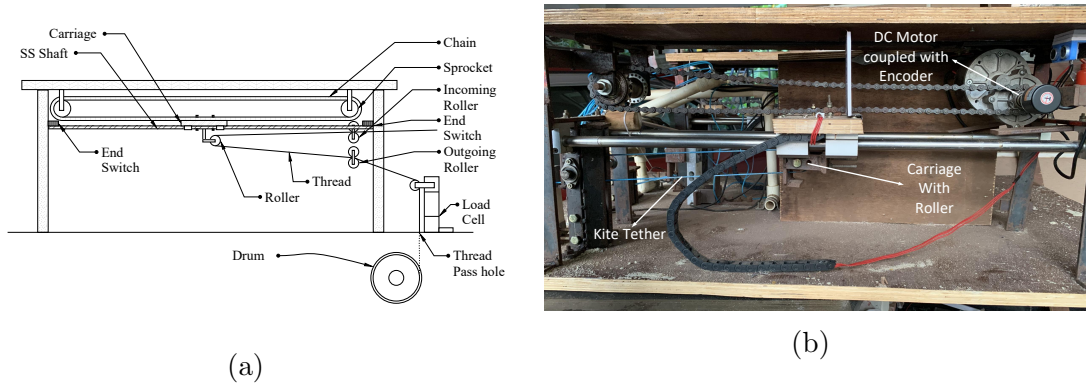


Figure 4.12: (a) Pictorial representation of the controller (Side View) (b) Side view of the developed kite controller

Table 4.1: Specifications of the proposed kite steer controller

Description	Specifications
Kite	Area = 12 m ² , 4 lines
Motor Controller	50V, 30A, H-bridge with position control
Brushed DC Motor	24 V, 250 W, 300 RPM
Optical encoder	5V, 360 PPR
Actuation Length	90cm
Actuation speed	45 cm/s
Battery	24 V, 15 Ah, Lead acid battery

4.3.3 Field Test and Data Analysis

Experimental tests were conducted to record the kite characteristics and the data is analysed for the implementation of the control method. Multiple field tests were conducted at a wind speed range of 3 m/s to 5 m/s with a fixed tether length of 24m. The data logged during the test includes on-air data which is transmitted to the ground and the sensor data at the ground. The on-air data include kite's position, orientation and altitude as shown in table 4.2. The data received at every 100ms time interval which is a rate of 10 samples/second. The orientation data consists of three Euler angles- Yaw, Pitch, and Roll in degrees. The altitude is measured using an altimeter which is given in meters and the position of the kite is represented by latitude and longitude values obtained by the Global Positioning System (GPS) module. A radio frequency (RF) module sends the on-air data to the ground station where the data is appended with the data at the ground station.

The ground level data includes wind speed, wind direction, tether tension of left , center , and right lines, power consumption of left and right motors, and

Table 4.2: Data received from the on-air device

Time (ms)	Yaw (degrees)	Pitch (degrees)	Roll (degrees)	Altitude (m)	Latitude (degrees)	Longitude (degrees)
0	52.70	-130.47	35.37	0.96	13.0091263	74.7885311
100	50.69	-131.77	48.04	1.95	13.0091232	74.7885259
200	48.37	-135.88	52.04	2.41	13.0091214	74.7885219
300	45.95	-143.91	54.69	4.98	13.0091167	74.7885097
400	47.21	-147.43	54.79	5.93	13.0091147	74.7885017
500	48.22	-149.27	46.20	7.14	13.0091131	74.7884937
600	52.37	-151.15	35.23	8.16	13.0091119	74.7884748
700	54.88	-155.89	29.09	10.05	13.0091119	74.7884655
800	56.08	-156.77	25.47	10.66	13.0091148	74.7884473
900	54.80	-160.41	25.39	12.23	13.0091164	74.7884386

Table 4.3: Data measured at the ground station and appended with the on-air data

W_s (m/s)	W_d (degrees)	F_{Centre} (N)	F_{Left} (N)	F_{Right} (N)	P_{Left} (W)	P_{Right} (W)	Act_{Left} (cm)	Act_{Right} (cm)
3.58	20	367.23	45.90	40.80	29.25	26.00	14.97	75.03
3.58	20	481.83	60.23	53.54	38.37	34.11	19.65	70.35
3.53	20	485.60	60.70	53.96	38.67	34.38	19.80	70.20
3.55	20	453.72	56.72	50.41	36.13	32.12	18.50	71.50
3.6	20	464.03	58.00	51.56	36.95	32.85	18.92	71.08
3.6	20	467.97	58.50	52.00	37.27	33.13	19.08	70.92
3.63	20	450.07	56.26	50.01	35.84	31.86	18.35	71.65
3.63	20	372.10	46.51	41.34	29.63	26.34	15.17	74.83
3.68	20	283.08	35.39	31.45	22.54	20.04	11.54	78.46
3.7	20	255.44	31.93	28.38	20.34	18.08	10.42	79.58

the actuation input of the left and the right control lines as shown in table 4.3. The wind speed is in m/s and the wind direction is represented in degrees with respect to East direction. The tether tension of the three lines is measured using individual load-cells. The three lines include- left control line, right control line and the center power line composed of two power lines which are joined together. The tether tension measured using load-cells are pre-calibrated using known tension value using weights. The left and the right actuator mechanism consumes power while steering the kite, and the power consumption of each actuator is measured and recorded. The actuation inputs given to the actuators is also recorded in the data logger.

4.4 Results and discussions

In this section, the results of field tests are discussed with manual control and the proposed RPZ control. The detailed analysis shows the various parameters

which affects the total aerodynamic force of the kite while controlling the kite. The performance of the control methods under steady wind and turbulent winds is also explained.

4.4.1 Manual Kite Control Test

The proposed ground-based controller is tested in various wind conditions for the study of the kite control characteristics. The kite used for the field tests is a Leading Edge Inflatable (LEI) kite with an area of 12 m^2 and the KSC consists of two linear actuators which are controlled through a wireless joystick controller as shown in figure 4.13. The tests were conducted near the university beach with the ground actuator assembly held by the sand bags to overcome the tether force. The sensor unit is mounted on the kite and held in place by using Velcro material. The test results of five field tests are tabulated in table 4.4 and the parameters in the figure-of-eight trajectory for the same five tests are tabulated in table 4.5.



Figure 4.13: (a) Kite used for the field tests (b) Kite steering controller

Table 4.4 shows five test cases of figure-of-eight trajectories, each with different boundary conditions and the corresponding figure-of-eight parameters are tabulated in table 4.5. Table 4.4 lists the boundary parameters using GPS and altitude data, the cycle time, and the average value of wind speed, power consumed to control the kite, power line force, and the total force from the three lines. In the table 4.4, we can observe, the case 1 & 2 have similar performances but the force in case 2 is increased by about 80 N due to the minimum altitude reached by the kite in case 2 is 8.95 m which is less than the case 1. The lower the altitude value, the greater the force from the kite as the kite achieves higher crosswind power in lower polar angles. In the test case 3, the average tether force is maximum even-though the average wind speed is low. The reason for the high tether force is due to the higher average kite velocity of 7.79 m/s as shown in case 3 of table 4.5. The case 4 has slightly less average tether force as the minimum altitude of the kite is 10.71 m as compared to 5.61 m in case 3. Also, the power consumed

by the actuator is more in case 4 at 73.89 W with less average total force of 490 N due to the short cycle time with higher kite velocity as shown in table 4.5. In the case 5, the average tether force is 399.36 N with an altitude change of 7.5m in the lower side to 16.14 in the higher side. From the above analysis we can infer that the tether force mainly depends on wind speed, kite speed, polar angle of the figure-of-eight trajectory which depends on the altitude of operation.

Table 4.4: Field test results for the manual control of the kite.

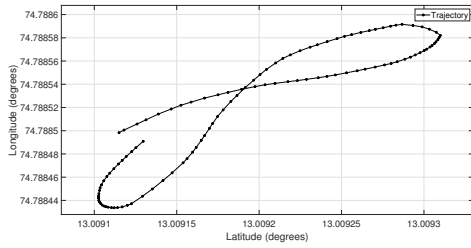
Case	Alt Min (m)	Alt Max (m)	GPS_left (degrees)	GPS_right (degrees)	cycle time (s)	Average Wind Speed (m/s)	Average Power Consumed per cycle (W)	Average Power Line Force (N)	Average Total Force (N)
1	12.34	22.27	13.0090977 74.7884159	13.0093365 74.7884958	9.1	3.49	43.11	222.34	290.01
2	8.95	20.15	13.0091642 74.7884265	13.0092229 74.7883342	9.9	3.29	54.71	284.38	370.26
3	5.61	18.79	13.0091500 74.7883795	13.0094292 74.7884968	10.0	2.79	73.33	388.79	503.89
4	10.71	22.38	13.0092322 74.7883272	13.0094317 74.7885093	8.0	2.86	73.89	374.02	490.01
5	7.5	16.14	13.0090919 74.7884766	13.0092599 74.7885688	9.5	3.3	60.26	304.77	399.36

Table 4.5 shows the parameters of figure-of-eight trajectories. The cycle time represents the time required to finish one figure-eight cycle. The perimeter of the loop denotes the distance travelled by the kite in a loop with the kite speed denoting the velocity of the kite in the loop.

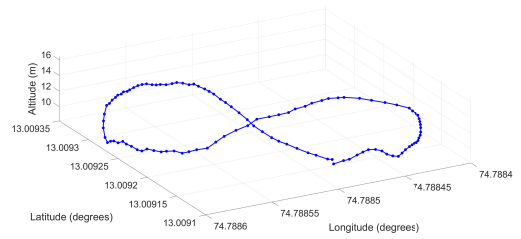
Table 4.5: The speed of the kite in the figure-of-eight maneuvers

Case	Cycle Time	Average Wind Speed (m/s)	Perimeter of loop (m)	Average Kite Speed (m/s)	Average Total Force (N)
1	9.1	3.49	67.46	7.41	290.01
2	9.9	3.29	70.99	7.02	370.26
3	10.0	2.79	78.72	7.79	503.89
4	8.0	2.86	69.12	8.53	490.01
5	9.5	3.30	51.13	5.38	399.36

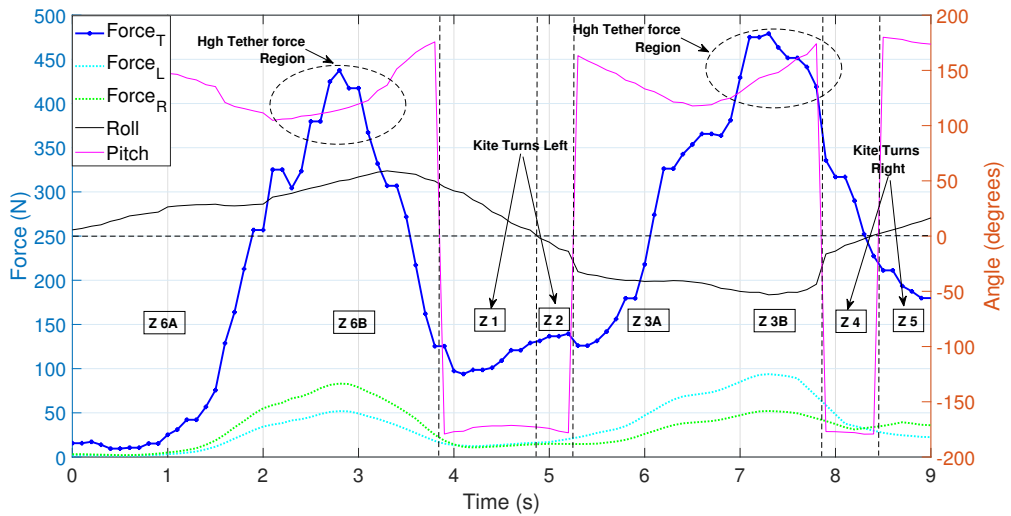
Figure 4.14 shows the field test results of the manual control of kite using ground-based KSC. Figure 4.14a shows the path followed by the kite using the GPS data (Lat & Lon). Figure 4.14b shows the 3D plot which includes altitude data with the GPS data. The GPS and altitude data provides the position of the kite and the data is used to detect the boundaries of the figure-of-eight trajectories. Figure 4.14c shows the tether force in a figure-of-eight trajectory with respect to time.



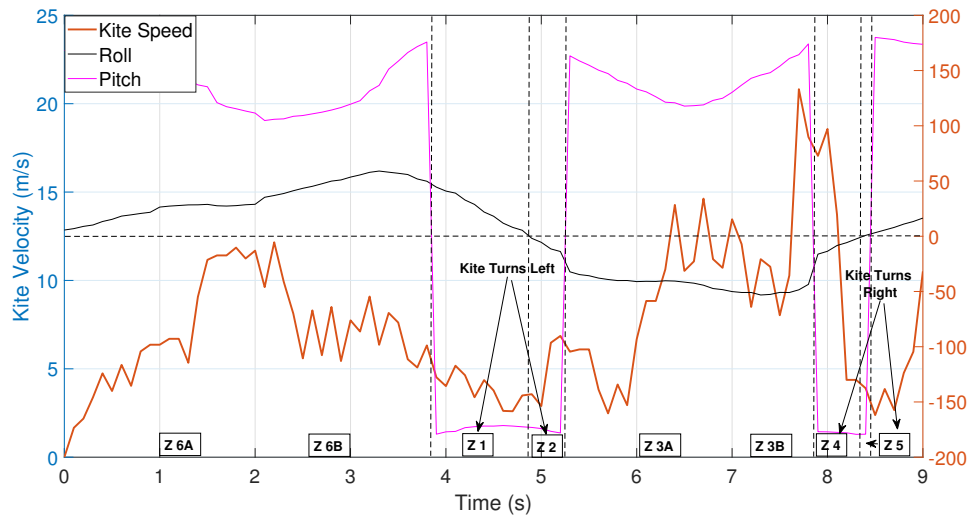
(a) Figure-of-eight trajectory



(b) 3D trajectory of th kite



(c) Forces in the trajectory



(d) Kite speed in the trajectory

Figure 4.14: (a) The figure-of-eight trajectory followed by the kite using latitude and longitude values (b) 3D visualization of the path followed by the kite using the altitude data (c) Tether force, left and right line force with respect to the trajectory of the kite (d) The speed of the kite in the given trajectory.

The position of the kite in the figure-eight trajectory is shown using zones as discussed in section 3.1. The control line forces are shown in dotted lines which are less in magnitude. From figure 4.14c we can observe that the tether force increases when the kite travels from higher side (zone 6A) of the trajectory to the lower side (zone 6B). The tether force reduces drastically while the kite makes a turn in the zone 1 & zone 2 of the figure-eight loop. The control line forces are less than 20% of the power line force as shown in the figure 4.14c. Figure 4.14d shows the kite velocity in the figure-of-eight loops for the same loops shown in figure 4.14c. The speed of the kite is obtained with the GPS data which is plotted with respect to roll and pitch of the kite which depicts the position of the kite. The kite velocity decreases drastically while it turns on the corners of the figure-eight loops.

4.4.2 RPZ Control Experimental Validation

The proposed RPZ control technique is tested with several cycles of figure-of-eight trajectories. Table 4.6 shows five cycles of operation with the corresponding boundary values, cycle time and the average value of wind speed, power consumed, power line force, and the total force from the three lines. The five different boundary values are taken as reference and the corresponding data is shown in the table. The case 2 and case 5 has similar performance with a slightly higher average wind speed, case 2 has higher total power of 491.45 N of force with power consumption of 72.31W. The case 1 has the least average total force value as the loop is in higher altitude with lower boundary of 16 m and higher boundary of 20 m. In a low wind condition such as in case 4, the force is increased by lowering the boundaries of altitude as shown in the table 4.6, the lower and upper limits of altitude are 6 and 14 respectively.

Table 4.6: RPZ controller field test data

Case	Alt Min (m)	Alt Max (m)	GPS.left (degrees)	GPS.right (degrees)	cycle time (s)	Average Wind Speed (m/s)	Average Power Consumed per cycle (W)	Average Power Line Force (N)	Average Total Force (N)
1	16	20	13.0090945 74.7883672	13.009170 74.7884896	7.8	2.79	31.98	156.81	207.01
2	9	17	13.0090750 74.7884645	13.0092965 74.7886033	11.0	2.64	72.31	377.96	491.45
3	10	18	13.0090835 74.7884551	13.0092710 74.7885650	11.0	2.77	57.57	282.67	373.04
4	6	14	13.0091010 74.7884613	13.0092540 74.7885500	7.8	2.06	64.08	328.77	429.35
5	6	19	13.0090775 74.7884679	13.0093110 74.7885847	10.6	2.54	71.31	350.97	462.91

Table 4.7 shows the corresponding parameters of the figure-of-eight loops listed in table 4.6. The perimeter of the a figure-eight cycle is the total distance travelled by the kite in the trajectory. In the case 1, the cycle time is less and the path

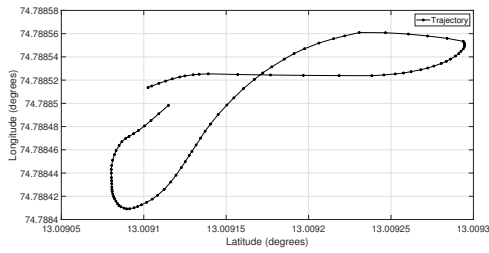
travelled by the kite is less and therefore the average total force is 207 N which is lesser than the other cases. The case 2 has the highest kite travel over a period of 11 seconds with an average kite velocity of 5.74 m/s. case 4 has almost double the force than case 1 in the exact same time of 7.8 seconds due to the increased average kite speed and the path travelled by the kite.

Table 4.7: The speed of the kite in the figure-of-eight maneuvers in RPZ method

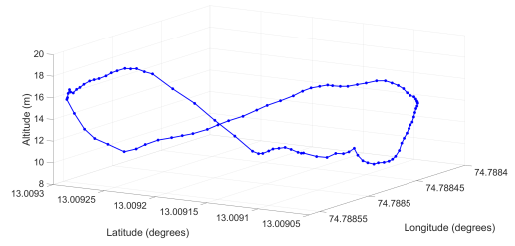
Case	Cycle Time	Average Wind Speed (m/s)	Perimeter of loop (m)	Average Kite Speed (m/s)	Average Total Force (N)
1	7.8	2.79	34.76	5.43	207.01
2	11.0	2.64	63.71	5.74	491.45
3	11.0	2.77	48.35	5.31	373.04
4	7.8	2.06	45.51	5.76	429.35
5	10.6	2.54	57.89	5.43	462.91

Figure 4.15 shows the control performance of the proposed RPZ method in a Steady Wind Condition (SWC). Figure 4.15a shows the figure-of-eight trajectory using GPS data and figure 4.15b shows the 3D trajectory of the kite with the help of altitude data of the kite. The tether force for one cycle of operation is shown in figure 4.15c with the position of the kite represented by zones using roll and pitch of the kite. We can observe that, in SWC, the tether force gradually reduces while the kite turns in the corners of the figure-eight. The force exerted by the left & right control lines is also shown using dotted lines. Figure 4.15d shows the kite velocity in the figure-eight trajectory. The kite velocity increases while the kite transitions from higher side (zone3A) of the loop to the bottom side of the loop (zone 3B) and the kite velocity decreases while kite turns left/right in the trajectory which we can observe in the plot.

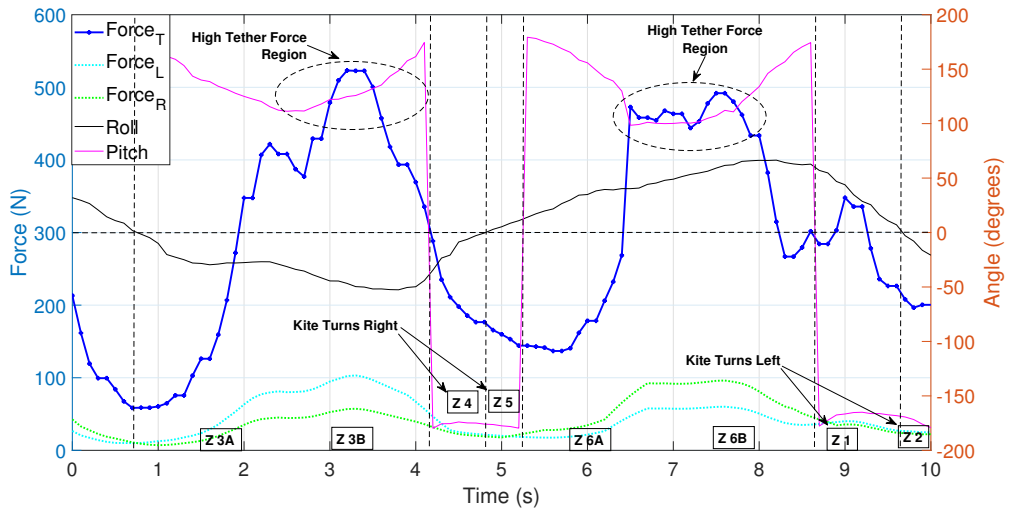
Figure 4.16 shows the results of RPZ controller in a Turbulent Wind Condition (TWC). The experimental data of the system from field tests during turbulent winds is plotted, which is termed as TWC. From the figure 4.16a and figure 4.16b we can observe the figure-of-eight shape has sudden changes in the kite path due to the turbulence in the wind. However, the KSC is able to control the kite which confines it within the boundary conditions. Figure 4.16c shows the tether force with respect to the trajectory of the kite in a loop. The spikes in the force value is due to the turbulence in the wind condition. The kite experiences a larger force even in the turns (zone 4 & zone 5). We can also observe the sudden changes in the kite velocity in figure 4.16d. The turbulent winds exerts sudden forces on the kite which we can clearly observe in the plots.



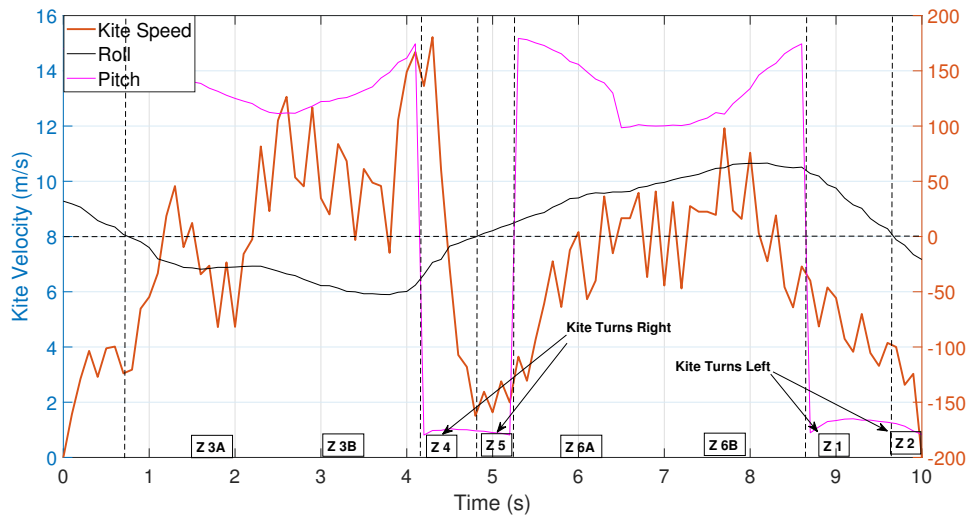
(a) Figure-of-eight trajectory



(b) 3D trajectory of th kite

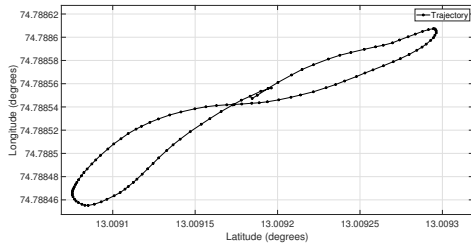


(c) Forces in the trajectory

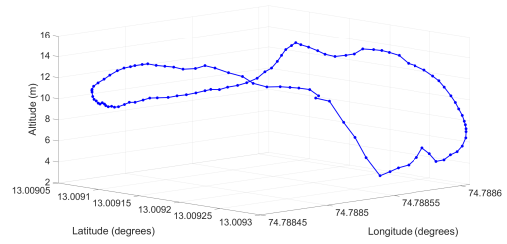


(d) Kite speed in the trajectory

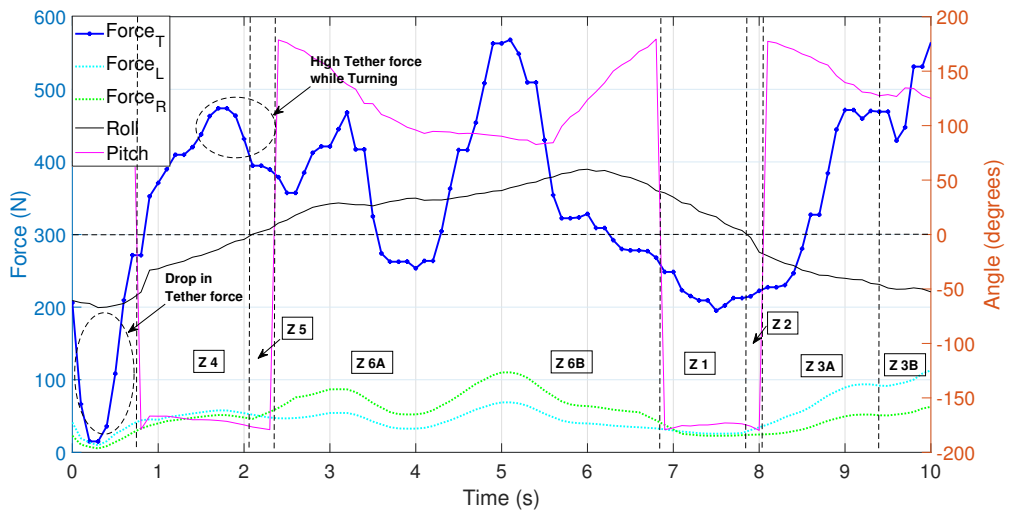
Figure 4.15: Kite data in SWC -(a) The figure-of-eight trajectory followed by the kite using GPS data (b) 3D view of the path followed by the kite using GPS & altitude data (c) Tether force, left and right line force with respect to the trajectory of the kite (d) The speed of the kite in the given trajectory.



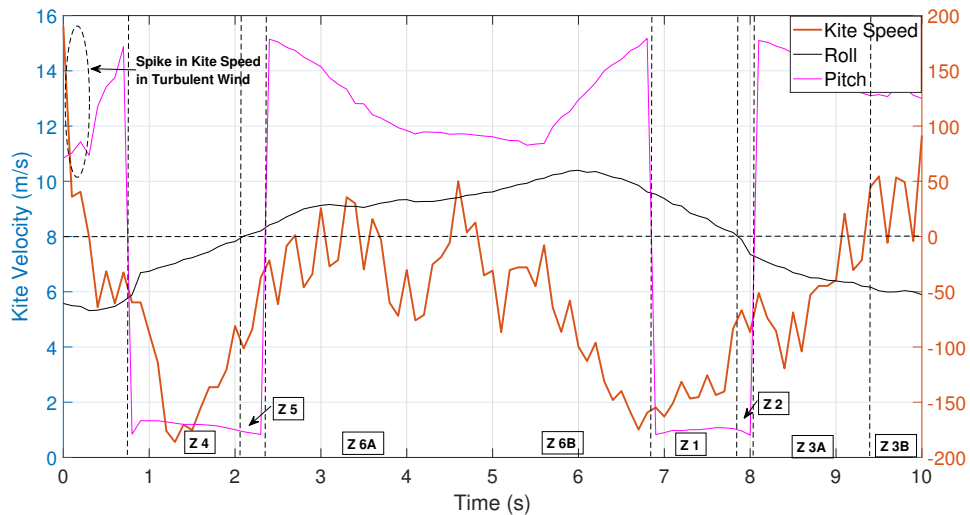
(a) Figure-of-eight trajectory



(b) 3D trajectory of th kite



(c) Forces in the trajectory

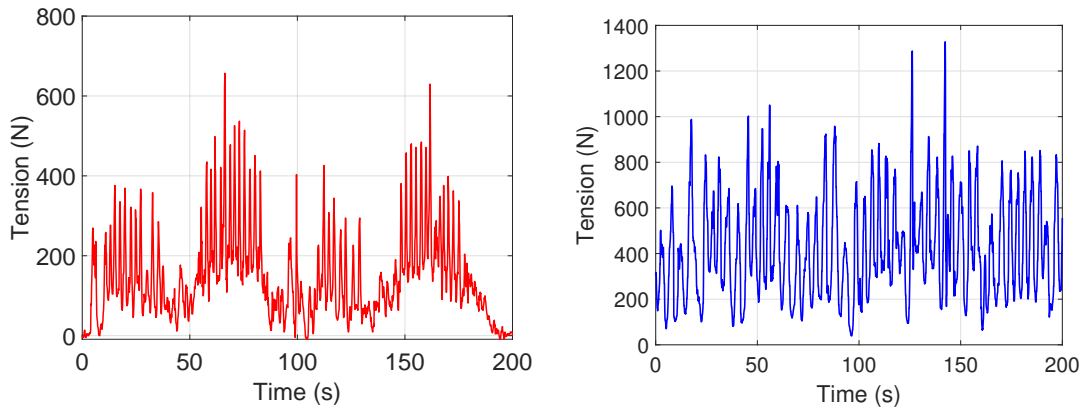


(d) Kite speed in the trajectory

Figure 4.16: Kite data in TWC -(a) The figure-of-eight trajectory followed by the kite using GPS data (b) 3D view of the path followed by the kite using GPS & altitude data (c) Tether force, left and right line force with respect to the trajectory of the kite (d) The speed of the kite in the given trajectory.

4.4.3 Comparative Analysis

The experimental result from our tests is compared with the kite power system developed by Kyushu University, Japan [Rushdi et al., 2020a]. The kite used for test given in the reference [Rushdi et al., 2020a] is a leading edge inflatable 6 m^2 kite and the tests were conducted by towing the kite to truck. The tether force in the figure-of-eight trajectory is compared with our field test results of tether force in the figure-eight trajectory. Figure 4.17 shows the comparison of tether force from the reference [Rushdi et al., 2020a] shown in figure 4.17a with the data from the proposed method shown in figure 4.17b. In the proposed manuscript, we have used a 12 m^2 kite in the steady wind condition. The variation in the tether tension is due to the variation of aerodynamic force in the figure-eight trajectory as discussed in the above section. The plot in figure 4.17b shows 20 cycles of figure eight with average time for each cycle is about 10 seconds. The proposed method has a steady variation in tether force which is observed in figure 4.17b.



(a) Tether Tension data taken from [Rushdi et al., 2020a] (b) Tether Tension from the proposed method

Figure 4.17: Comparison of tether tension (a) Data from the methods using in the reference [Rushdi et al., 2020a] & (b) Data from the proposed method.

4.4.4 Power simulation results

The power generation from the kite is simulated using the field test data. As discussed in section 2.1, the kite aerodynamic model is used to simulate the power generation using MATLAB coding environment. Figure 4.18 shows the force data of centre line (F_{centre}), total force (F_{total}) which sum of centre line and control line forces, and control line force ($F_{control}$) from the field tests. Figure 4.18a and figure 4.18b show Steady Wind Condition (SWC) and Turbulent Wind Condition (TWC) respectively. The force data plot of one complete figure-eight cycle is plotted, and from the data, the average total force is 506 N, average centre line force is 388 N, and the average force from control lines is 115 N in SWC. The average wind speed in the loop is 3.1 m/s and an average kite velocity of 7.8 m/s. The control line force is the sum of both left and right control lines. The control

lines are also connected to the drum and therefore, the control lines also contribute to the power generation. In the TWC, the average total force is 449 N , average centre line force is 346 N, and the average force from control lines is 103 N with an average wind speed of 2.8 m/s and kite speed of 5.4 m/s. The average force from the both the control line is about 23 % of average total force for the particular kite used in this experiment for both SWC & TWC.

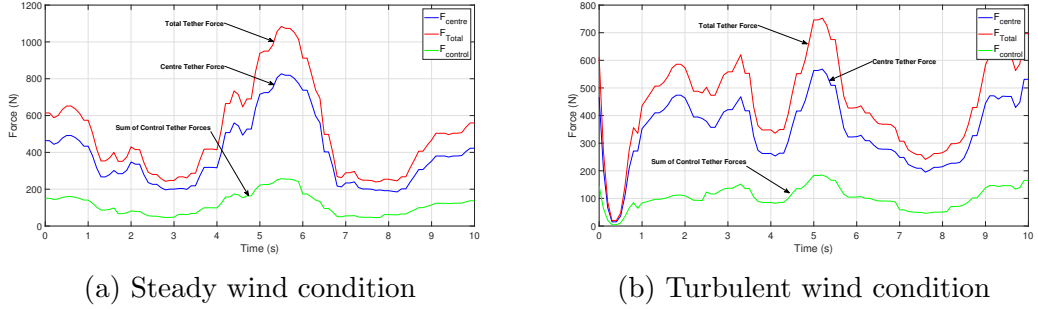


Figure 4.18: Comparison of centre line force with control line forces and total aerodynamic force. (a) Steady wind & (b) Turbulent wind conditions

Figure 4.19 shows the simulation results of electric power generated in the figure-of-eight cycle discussed in figure 4.18 by considering the generator efficiency of 90%. Figure 4.19a shows the power plots for SWC and figure 4.19b shows the power plots for TWC. The generator power shown in the plot is the power measured at the terminal of the generator and the net power is the amount of power after deducting the power spent for controlling the kite. In the SWC, the average total power generated in the cycle is 422 W, the average power consumed by the KSC is 85 W, and average net power generated in the cycle is 337 W. In TWC, the average power generated on the generator terminal is 382 W, the average power consumed by the KSC is 79 W, and the net power generated in the cycle is 303 W. The power consumption is about 20 % of the generated power in the cycle for both SWC and TWC.

Figure 4.20 shows the power consumed by the linear actuators to steer the kite in the figure-eight trajectory in SWC and TWC. The power consumed by the actuator is simulated in MATLAB method described in the section 4.3 and compared with the actual power measured in the field test. In SWC, the KPS consumes an average power of 85 W and the peak power is 187 W at an average wind speed of 3.1 m/s in a cycle. In TWC, the KPS consumes 79 W with a peak power of 185 W is consumed at an average wind speed of 2.8 m/s. The simulation results rely on the feedback from the kite orientation and position sensors, and in the TWC, a sudden movement introduces a spike. The power variation in SWC is gradual and in the TWC, we can observe the spikes in the power levels and also, the kite experiences a larger force while turning in TWC as compared to SWC.

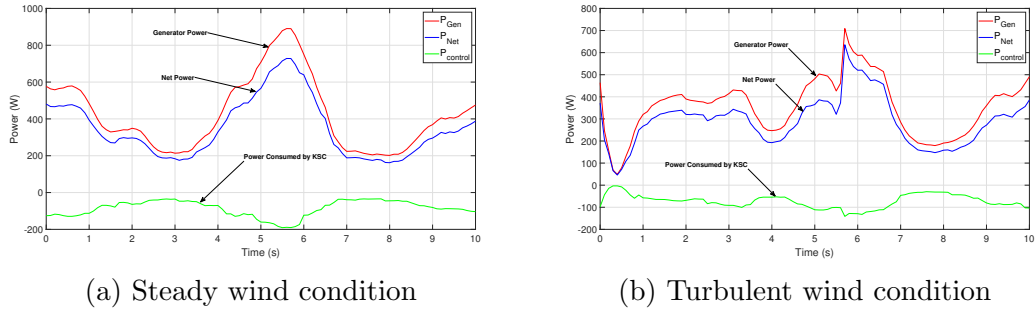


Figure 4.19: Comparison of power generated by centre line only with the total power generated. (a) Steady wind & (b) Turbulent wind conditions

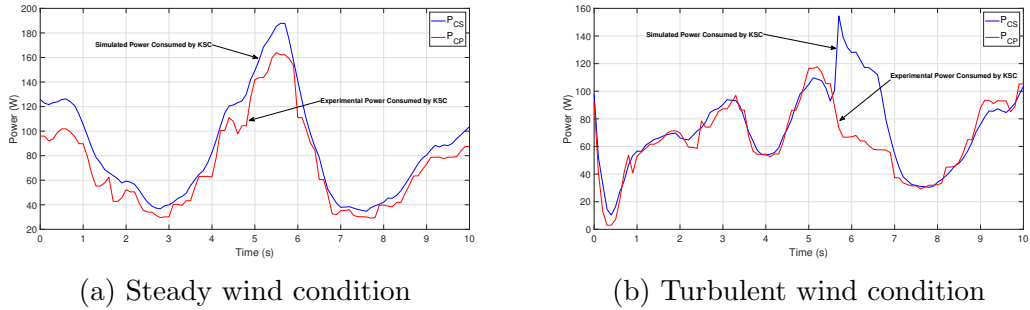


Figure 4.20: Power consumed to control the kite: Simulated and experimental value. (a) Steady wind & (b) Turbulent wind conditions

4.5 Summary

The kite steering mechanism is critical to controlling and steering the kite in defined crosswind trajectories. The kite steering mechanism imitates the human control method of the kite and steers the kite autonomously. The proposed RPZ method is tested with multiple experimental tests with a 12 m^2 Leading Edge inflatable kite. The proposed actuation mechanism consists of two linear actuators with a maximum of 90 cm displacement in each control line. From the field tests, the controller performance is evaluated by using a Leading Edge Inflatable kite and the following observations was made.

- There is a sudden movement to the kite for a given control input for the turbulent wind profile. The controller should be able to actuate rapidly under the load condition. The proposed controller design can actuate the kite rapidly with a speed of 45 cm/s and pull 90 cm of tether length in 2 seconds.
- The RPZ controller is tested with multiple operation cycles and at different times of the day. The controller is tested with various boundary conditions of the figure-eight loops. From the field tests, the force exerted by the control lines is about 23 % of the total force.

- On average, the linear actuators consume about 20 % of the total power generated in a cycle for controlling the kite in a figure-eight trajectory. Therefore, the power consumed by the controller must be considered while calculating the average power production.
- The kite's speed in the figure-of-eight loop plays a major role in the net aerodynamic force from the kite. As the kite speed increases, the net aerodynamic force and the force on the control lines increase. The increase in kite speed introduces additional load on the KSC actuators.
- The power generation in a figure-eight trajectory is analyzed. The power increases as the kite speed increases when the kite travels from higher to lower elevations.

The study on the proposed ground-based KSC is presented with a novel RPZ control approach with the power consumption analysis in the figure-eight loops. The results provide critical aspects and significance of figure-of-eight loops on the net power generation from the kite-based wind power generation systems. This study considers the force analysis of the kite's control lines to calculate the net power production in a cycle. The effects of tether length on the controller's performance must be investigated to optimize the controller further.

Chapter 5

Conclusion and Future Scope

We are witnessing a global transition towards using renewable energy sources to reduce the effects of global warming. The demand for clean and green energy is growing exponentially. Significantly, the transportation industry is moving towards electric vehicles, increasing energy demand tremendously. There is a need to ramp up the throughput from the renewable energy sector to move towards sustainability. Researchers worldwide are focusing on alternative ways to produce green energy. Collective efforts are required from various types of renewable energy sources to contribute to a sustainable future. Kite Power System (KPS) is one of the solutions which can fill the gap in the renewable energy mixture. The proposed work solves some of the challenges KPS poses and promotes the system's more straightforward implementation on a commercial scale.

5.1 Conclusion

Kite Power System (KPS) is an innovative technology which can contribute to the renewable energy sector by overcoming the drawbacks of conventional wind turbines. KPS is a highly mobile and efficient technology which can be deployed in regions where conventional turbines cannot be installed. A reliable and fully autonomous system must be developed for a commercial-scale KPS. Attention must be given to the challenges involved in the system in order to make the system reliable. The presented research work provides attention to the challenges posed by KPS by developing a model from the kite's aerodynamics to the kite's power generation aspects. The design and simulation methodologies are meticulously explained with experimental validation. A small-scale experimental setup is developed to investigate the kite's characteristics in various wind profiles. The data from multiple field tests and under varying wind conditions is collected, analysed, and presented in this research work. A MATLAB-Simulink model is developed to simulate the power generation capability of the system with various power ratings to investigate the characteristics and performance of the system. A ground-based kite steer unit is also developed with novel control topology to control the kite in

various wind conditions. The consolidated conclusions from each of the chapters are as follows:

Chapter 1 The background of the kite-based airborne wind power conversion system with the working of the system is briefly introduced. A detailed literature survey explains the prominent advantages of KPS over conventional wind turbines and the challenges involved in the system. The KPS fills the gaps present in conventional wind turbine technology. The research gaps in the literature must be addressed for their adoption as a reliable product.

Chapter 2 The extraction of power from the kite depends on the aerodynamic force of the kite. A methodology to estimate the tether force of the kite using a physical model (PM) is explained. The designed experimental setup is tested in the field, and the data collected is utilised for predicting the tether force from the Machine Learning (ML) methods. Two machine learning algorithms - Artificial Neural Network (ANN) and Long Short Term Memory (LSTM)- are developed and experimentally validated. The ML methods provide promising results in both steady and turbulent wind conditions.

Chapter 3 The potential of KPS is investigated with an emulation-based approach. A simulation model of the KPS is developed using a Field Orientation Control (FOC) based Permanent Magnet Synchronous Machine (PMSM) to emulate the power generation aspects of the system in various power ratings. The results of the study reveal insights into the scalability of the system. The system's behaviour with varying wind conditions is analysed using satellite data and experimental data from the field tests.

Chapter 4 A design and development methodology of a ground-based Kite Steer Controller is presented in the research work. The kite's characteristics in the figure-eight trajectory is studied with the variation of tether force with respect to the force on the control lines. The designed actuator is tested using a novel control method under steady and turbulent wind conditions. The power consumed by the kite steering unit is significant and must be considered while calculating the net power generation from the KPS. The significance of the orientation of the kite with respect to the figure-eight trajectory is analysed, and the power curve for a figure-of-eight loop is explained in detail for both steady and turbulent wind conditions.

5.2 Contributions

This dissertation presents a design, simulation, and development of experimental models to investigate the power and control aspects of the kite in various wind

profiles. The key contributions of this research work are listed below:

- The design and development of an experimental setup to measure the tether force of the airborne kite is presented with a systematic approach for the prediction of tether force is presented in this research work.
- The tether force estimation methods are developed based on field test data using a physical model of the kite and machine learning methods. The proposed methods are experimentally validated, which indicates that the proposed LSTM method performs better in both steady and turbulent wind conditions.
- The potential of a kite-based airborne wind energy conversion system is investigated with an emulation-based approach using field-oriented control of PMSM. The simulation shows promising results for developing and deploying KPS under varying wind profiles.
- A design and research methodology for developing a ground-based kite steer controller is described in this research work. The rapid actuation of the kite steer controller using the proposed design is tested in turbulent wind conditions.
- The research unfolds the crucial design aspects of the kite steering controller, which depends on the force of the control lines of the kite. The kite steering performance in the figure-eight trajectory is analysed, and the data collection and analysis are systematically described.
- The power consumption of the kite steer controller in steady and turbulent conditions in the figure-eight trajectory is presented and experimentally validated. The results of this study promote the development of kite-based power generation systems and their adoption in the wind power industry.

5.3 Future Scope of Work

The research work presented in this thesis needs further improvements, which are listed as follows:

- The modelling of the aerodynamic force of the kite is an essential aspect of the KPS. The accuracy of the tether force estimation methods can be improved by using three-dimensional ultrasonic wind measurement devices on the kite. This research is significant in forecasting the power generation capabilities of airborne wind energy systems.
- Development of lab-scale, hardware-in-loop, real-time simulation of the KPS with the emulation of real-time kite controller, which can provide system dynamics of an actual system.
- The experimental setup to evaluate the power generation using PMSM and

optimization of power generation methods for off-grid and grid-connected systems.

- The study of vertical take-off and landing techniques in high wind velocity conditions such as storms for increasing the reliability of the KPS.

Bibliography

- [Afanaseva and Ilyushin, 2018] Afanaseva, O. and Ilyushin, Y. (2018). Analysis and synthesis of distributed icedrill heating control system of mountain reconnaissance drilling rig. *International Multidisciplinary Scientific GeoConference: SGEM*, 18(2.2):41–47.
- [Ahmad et al., 2014] Ahmad, A. S., Hassan, M. Y., Abdullah, M. P., Rahman, H. A., Hussin, F., Abdullah, H., and Saidur, R. (2014). A review on applications of ann and svm for building electrical energy consumption forecasting. *Renewable and Sustainable Energy Reviews*, 33:102–109.
- [Ahmed, 2014] Ahmed, M. (2014). *Optimisation de contrôle commande des systèmes de génération d’électricité à cycle de relaxation*. PhD thesis, Université de Grenoble.
- [Ahmed et al., 2011] Ahmed, M., Hably, A., and Bacha, S. (2011). Power maximization of a closed-orbit kite generator system. In *2011 50th IEEE Conference on Decision and Control and European Control Conference*, pages 7717–7722. IEEE.
- [Ahmed et al., 2014] Ahmed, M., Hably, A., Bacha, S., and Ovalle, A. (2014). Kite generator system: Grid integration and validation. In *IECON 2014-40th Annual Conference of the IEEE Industrial Electronics Society*, pages 2139–2145. IEEE.
- [Ahmed et al., 2013] Ahmed, M. S., Hably, A., and Bacha, S. (2013). Kite generator system modeling and grid integration. *IEEE Transactions on Sustainable Energy*, 4(4):968–976.
- [Ahrens et al., 2013] Ahrens, U., Diehl, M., and Schmehl, R. (2013). *Airborne wind energy*. Springer Science & Business Media.
- [Akberali et al., 2021] Akberali, A. F. K., Kheiri, M., and Bourgault, F. (2021). Generalized aerodynamic models for crosswind kite power systems. *Journal of Wind Engineering and Industrial Aerodynamics*, 215:104664.
- [Alaimo et al., 2013] Alaimo, A., Artale, V., Milazzo, C., and Ricciardello, A. (2013). Comparison between euler and quaternion parametrization in uav dy-

- namics. In *AIP Conference Proceedings*, volume 1, pages 1228–1231. American Institute of Physics.
- [Argatov et al., 2011] Argatov, I., Rautakorpi, P., and Silvennoinen, R. (2011). Apparent wind load effects on the tether of a kite power generator. *Journal of Wind Engineering and Industrial Aerodynamics*, 99(10):1079–1088.
- [Ba et al., 2022] Ba, X., Gong, Z., Guo, Y., Zhang, C., and Zhu, J. (2022). Development of equivalent circuit models of permanent magnet synchronous motors considering core loss. *Energies*, 15(6):1995.
- [Baayen and Ockels, 2012] Baayen, J. H. and Ockels, W. J. (2012). Tracking control with adaption of kites. *IET control theory & applications*, 6(2):182–191.
- [Bagaber et al., 2022] Bagaber, B., Heide, D., Ponick, B., and Mertens, A. (2022). Efficiency and lifetime analysis of several airborne wind energy electrical drive concepts. In *2022 24th European Conference on Power Electronics and Applications (EPE'22 ECCE Europe)*, pages 1–11. IEEE.
- [Bagaber et al., 2020] Bagaber, B., Junge, P., and Mertens, A. (2020). Lifetime estimation and dimensioning of the machine-side converter for pumping-cycle airborne wind energy system. In *2020 22nd European Conference on Power Electronics and Applications (EPE'20 ECCE Europe)*, pages P–1. IEEE.
- [Bagaber and Mertens, 2021] Bagaber, B. and Mertens, A. (2021). A parallel voltage source converter and diode rectifier pmsm drive concept for decoupling the thermal cycles in the machine-side converter of an airborne wind energy generator. In *2021 23rd European Conference on Power Electronics and Applications (EPE'21 ECCE Europe)*, pages P–1. IEEE.
- [Baheri and Vermillion, 2017] Baheri, A. and Vermillion, C. (2017). Altitude optimization of airborne wind energy systems: A bayesian optimization approach. In *2017 American Control Conference (ACC)*, pages 1365–1370. IEEE.
- [Bansal et al., 2002] Bansal, R., Bhatti, T., and Kothari, D. (2002). On some of the design aspects of wind energy conversion systems. *Energy conversion and management*, 43(16):2175–2187.
- [Battaiotto et al., 1996] Battaiotto, P., Mantz, R., and Puleston, P. (1996). A wind turbine emulator based on a dual dsp processor system. *Control Engineering Practice*, 4(9):1261–1266.
- [Bauer et al., 2016] Bauer, F., Hackl, C. M., Smedley, K., and Kennel, R. M. (2016). ” virtual”-power-hardware-in-the-loop simulations for crosswind kite power with ground generation. In *2016 American Control Conference (ACC)*, pages 4071–4076. IEEE.
- [Bauer et al., 2018] Bauer, F., Kennel, R. M., Hackl, C. M., Campagnolo, F., Patt, M., and Schmehl, R. (2018). Drag power kite with very high lift coefficient.

- Renewable energy*, 118:290–305.
- [Borobia-Moreno et al., 2021] Borobia-Moreno, R., Ramiro-Rebollo, D., Schmehl, R., and Sánchez-Arriaga, G. (2021). Identification of kite aerodynamic characteristics using the estimation before modeling technique. *Wind Energy*, 24(6):596–608.
- [Breukels, 2011] Breukels, J. (2011). An engineering methodology for kite design.
- [Burgin and Wilson, 1985] Burgin, N. and Wilson, P. (1985). The influence of cable forces on the efficiency of kite devices as a means of alternative propulsion. *Journal of wind engineering and industrial aerodynamics*, 20(1-3):349–367.
- [Caduff et al., 2012] Caduff, M., Huijbregts, M. A., Althaus, H.-J., Koehler, A., and Hellweg, S. (2012). Wind power electricity: the bigger the turbine, the greener the electricity? *Environmental science & technology*, 46(9):4725–4733.
- [Canale et al., 2009] Canale, M., Fagiano, L., and Milanese, M. (2009). High altitude wind energy generation using controlled power kites. *IEEE Transactions on Control Systems Technology*, 18(2):279–293.
- [Castelino and Kashyap, 2021] Castelino, R. V. and Kashyap, Y. (2021). Airborne manoeuvre tracking device for kite-based wind power generation. In *Control Applications in Modern Power System*, pages 497–507. Springer.
- [Castelino et al., 2022] Castelino, R. V., Kashyap, Y., and Kosmopoulos, P. (2022). Airborne kite tether force estimation and experimental validation using analytical and machine learning models for coastal regions. *Remote Sensing*, 14(23):6111.
- [Castro-Fernández et al., 2023] Castro-Fernández, I., DeLosRíos-Navarrete, F., Borobia-Moreno, R., Fernández-Jiménez, M., García-Cousillas, H., Zastustingorri, M., Ghobaissi, A., López-Vega, F., Best, K., Cavallaro, R., et al. (2023). Automatic testbed with a visual motion tracking system for airborne wind energy applications. *Wind Energy*, 26(4):388–401.
- [Cayon et al., 2023] Cayon, O., Gaunaa, M., and Schmehl, R. (2023). Fast aerostuctural model of a leading-edge inflatable kite. *Energies*, 16(7):3061.
- [Center, 2005] Center, N. G. R. (2005). Kite inclination effects. <https://www.grc.nasa.gov/www/k-12/VirtualAero/BottleRocket/airplane/kiteincl.html>. Accessed: 2022-01-20.
- [Cherubini et al., 2015] Cherubini, A., Papini, A., Vertechy, R., and Fontana, M. (2015). Airborne wind energy systems: A review of the technologies. *Renewable and Sustainable Energy Reviews*, 51:1461–1476.
- [Coleman et al., 2014] Coleman, J., Ahmad, H., Pican, E., and Toal, D. (2014). Modelling of a synchronous offshore pumping mode airborne wind energy farm.

- Energy*, 71:569–578.
- [Costello et al., 2017] Costello, S., François, G., and Bonvin, D. (2017). Real-time optimizing control of an experimental crosswind power kite. *IEEE Transactions on control systems technology*, 26(2):507–522.
- [Dadd et al., 2011] Dadd, G. M., Hudson, D. A., and Shenoi, R. (2011). Determination of kite forces using three-dimensional flight trajectories for ship propulsion. *Renewable Energy*, 36(10):2667–2678.
- [De Lellis et al., 2016] De Lellis, M., Mendonça, A., Saraiva, R., Trofino, A., and Lezana, A. (2016). Electric power generation in wind farms with pumping kites: An economical analysis. *Renewable energy*, 86:163–172.
- [De Lellis et al., 2013] De Lellis, M., Saraiva, R., and Trofino, A. (2013). Turning angle control of power kites for wind energy. In *52nd IEEE Conference on Decision and Control*, pages 3493–3498. IEEE.
- [DeCarolis and Keith, 2006] DeCarolis, J. F. and Keith, D. W. (2006). The economics of large-scale wind power in a carbon constrained world. *Energy Policy*, 34(4):395–410.
- [Dief et al., 2018] Dief, T. N., Fechner, U., Schmehl, R., Yoshida, S., Ismaiel, A. M., and Halawa, A. M. (2018). System identification, fuzzy control and simulation of a kite power system with fixed tether length. *Wind Energy Science*, 3(1):275–291.
- [Dief et al., 2020a] Dief, T. N., Fechner, U., Schmehl, R., Yoshida, S., and Rushdi, M. A. (2020a). Adaptive flight path control of airborne wind energy systems. *Energies*, 13(3):667.
- [Dief et al., 2020b] Dief, T. N., Rushdi, M., Halawa, A., and Yoshida, S. (2020b). Hardware-in-the-loop (hil) and experimental findings for the 7 kw pumping kite power system. In *AIAA Scitech 2020 Forum*, page 1244.
- [Duckworth, 1985] Duckworth, R. (1985). The application of elevated sails (kites) for fuel saving auxiliary propulsion of commercial vessels. *Journal of wind engineering and industrial aerodynamics*, 20(1-3):297–315.
- [Eijkelhof et al., 2023] Eijkelhof, D., Buendía, G., and Schmehl, R. (2023). Low- and high-fidelity aerodynamic simulations of box wing kites for airborne wind energy applications. *Energies*, 16(7):3008.
- [Erhard and Strauch, 2012] Erhard, M. and Strauch, H. (2012). Control of towing kites for seagoing vessels. *IEEE Transactions on Control Systems Technology*, 21(5):1629–1640.
- [Erhard and Strauch, 2013] Erhard, M. and Strauch, H. (2013). Theory and experimental validation of a simple comprehensible model of tethered kite dy-

- namics used for controller design. In *Airborne wind energy*, pages 141–165. Springer.
- [Erhard and Strauch, 2015] Erhard, M. and Strauch, H. (2015). Flight control of tethered kites in autonomous pumping cycles for airborne wind energy. *Control Engineering Practice*, 40:13–26.
- [Eric Tseng et al., 2007] Eric Tseng, H., Xu, L., and Hrovat, D. (2007). Estimation of land vehicle roll and pitch angles. *Vehicle System Dynamics*, 45(5):433–443.
- [Fagiano, 2009] Fagiano, L. (2009). Control of tethered airfoils for high-altitude wind energy generation. *Politecnico di Torino*.
- [Fagiano et al., 2010] Fagiano, L., Milanese, M., Razza, V., and Gerlero, I. (2010). Offshore high-altitude wind energy using controlled airfoils. In *European Wind Energy Conference (EWEC) 2010*.
- [Fagiano et al., 2017] Fagiano, L., Nguyen-Van, E., Rager, F., Schnez, S., and Ohler, C. (2017). Autonomous takeoff and flight of a tethered aircraft for airborne wind energy. *IEEE transactions on control systems technology*, 26(1):151–166.
- [Fechner, 2016] Fechner, U. (2016). A methodology for the design of kite-power control systems. *Unpublished PhD Thesis, Delft University of Technology, Delft, the Netherlands*.
- [Fechner and Schmehl, 2012] Fechner, U. and Schmehl, R. (2012). Design of a distributed kite power control system. In *2012 IEEE International Conference on Control Applications*, pages 800–805. IEEE.
- [Fechner and Schmehl, 2013] Fechner, U. and Schmehl, R. (2013). Model-based efficiency analysis of wind power conversion by a pumping kite power system. *Airborne wind energy*, pages 249–269.
- [Fechner and Schmehl, 2014] Fechner, U. and Schmehl, R. (2014). Feed-forward control of kite power systems. In *Journal of Physics: Conference Series*, volume 524, page 012081. IOP Publishing.
- [Fechner and Schmehl, 2016] Fechner, U. and Schmehl, R. (2016). Flight path control of kite power systems in a turbulent wind environment. In *2016 American Control Conference (ACC)*, pages 4083–4088. IEEE.
- [Fechner et al., 2015] Fechner, U., van der Vlugt, R., Schreuder, E., and Schmehl, R. (2015). Dynamic model of a pumping kite power system. *Renewable Energy*, 83:705–716.
- [Fisscher, 2020] Fisscher, W. (2020). Optimisation of control for an airborne wind turbine: with maximum power point tracking.

- [Fritz, 2013] Fritz, F. (2013). Application of an automated kite system for ship propulsion and power generation. In *Airborne wind energy*, pages 359–372. Springer.
- [Furey and Harvey, 2007] Furey, A. and Harvey, I. (2007). Evolution of neural networks for active control of tethered airfoils. *Lecture Notes in Computer Science*, 4648:746.
- [Greff et al., 2016] Greff, K., Srivastava, R. K., Koutník, J., Steunebrink, B. R., and Schmidhuber, J. (2016). Lstm: A search space odyssey. *IEEE transactions on neural networks and learning systems*, 28(10):2222–2232.
- [Hagen et al., 2023] Hagen, L. v., Petrick, K., Wilhelm, S., and Schmehl, R. (2023). Life-cycle assessment of a multi-megawatt airborne wind energy system. *Energies*, 16(4):1750.
- [Hobbs, 1986] Hobbs, S. (1986). *A quantitative study of kite performance in natural wind with application to kite anemometry*. PhD thesis, Cranfield University.
- [Houska and Diehl, 2007] Houska, B. and Diehl, M. (2007). Optimal control for power generating kites. In *2007 European Control Conference (ECC)*, pages 3560–3567. IEEE.
- [Hummel et al., 2019] Hummel, J., Göhlich, D., and Schmehl, R. (2019). Automatic measurement and characterization of the dynamic properties of tethered membrane wings. *Wind Energy Science*, 4(1):41–55.
- [Ilyushin and Afanaseva, 2019] Ilyushin, Y. V. and Afanaseva, O. V. (2019). Development of scada-model for trunk gas pipeline’s compressor station. *Journal of mining institute*, 240:686–693.
- [Ilzhöfer et al., 2007] Ilzhöfer, A., Houska, B., and Diehl, M. (2007). Nonlinear mpc of kites under varying wind conditions for a new class of large-scale wind power generators. *International Journal of Robust and Nonlinear Control: IFAC-Affiliated Journal*, 17(17):1590–1599.
- [Jehle and Schmehl, 2014] Jehle, C. and Schmehl, R. (2014). Applied tracking control for kite power systems. *Journal of Guidance, Control, and Dynamics*, 37(4):1211–1222.
- [Johansen, 2021] Johansen, K. (2021). Blowing in the wind: A brief history of wind energy and wind power technologies in denmark. *Energy Policy*, 152:112139.
- [Karduna et al., 2000] Karduna, A. R., McClure, P. W., and Michener, L. A. (2000). Scapular kinematics: effects of altering the euler angle sequence of rotations. *Journal of Biomechanics*, 33(9):1063–1068.
- [Khan and Rehan, 2016] Khan, Z. and Rehan, M. (2016). Harnessing airborne

- wind energy: Prospects and challenges. *Journal of Control, Automation and Electrical Systems*, 27(6):728–740.
- [Kim et al., 2012] Kim, K.-H., Van, T. L., Lee, D.-C., Song, S.-H., and Kim, E.-H. (2012). Maximum output power tracking control in variable-speed wind turbine systems considering rotor inertial power. *IEEE transactions on industrial electronics*, 60(8):3207–3217.
- [Kolar et al., 2013] Kolar, J. W., Friedli, T., Krismer, F., Looser, A., Schweizer, M., Friedemann, R. A., Steimer, P. K., and Bevirt, J. B. (2013). Conceptualization and multiobjective optimization of the electric system of an airborne wind turbine. *IEEE Journal of Emerging and Selected Topics in Power Electronics*, 1(2):73–103.
- [Lansdorp et al., 2007] Lansdorp, B., Ruiterkamp, R., and Ockels, W. (2007). Towards flight testing of remotely controlled surfkites for wind energy generation. In *AIAA Atmospheric Flight Mechanics Conference and Exhibit*, page 6643.
- [LeCun et al., 2015] LeCun, Y., Bengio, Y., and Hinton, G. (2015). Deep learning. *nature*, 521(7553):436–444.
- [Licitra et al., 2017] Licitra, G., Bürger, A., Williams, P., Ruiterkamp, R., and Diehl, M. (2017). System identification of a rigid wing airborne wind energy system. *arXiv preprint arXiv:1711.10010*.
- [Licitra et al., 2019] Licitra, G., Koenemann, J., Bürger, A., Williams, P., Ruiterkamp, R., and Diehl, M. (2019). Performance assessment of a rigid wing airborne wind energy pumping system. *Energy*, 173:569–585.
- [Long et al., 2022] Long, X., Sun, M., Chen, Z., and Wang, Y. (2022). Coupled trajectory optimization and tuning of tracking controllers for parafoil generator. *International Journal of Green Energy*, pages 1–13.
- [Loyd, 1980a] Loyd, M. (1980a). crosswind kite power for large-scale wind power production. *Energy*, 4:106–111.
- [Loyd, 1980b] Loyd, M. L. (1980b). Crosswind kite power (for large-scale wind power production). *Journal of energy*, 4(3):106–111.
- [Luchsinger, 2013] Luchsinger, R. H. (2013). Pumping cycle kite power. In *Airborne wind energy*, pages 47–64. Springer.
- [Lunney et al., 2017] Lunney, E., Ban, M., Duic, N., and Foley, A. (2017). A state-of-the-art review and feasibility analysis of high altitude wind power in northern ireland. *Renewable and Sustainable Energy Reviews*, 68:899–911.
- [Martinez et al., 2014] Martinez, F., Herrero, L. C., and de Pablo, S. (2014). Open loop wind turbine emulator. *Renewable Energy*, 63:212–221.
- [Meghana et al., 2022] Meghana, A., Smitha, B., and Jagwani, S. (2022). Tech-

- nological advances in airborne wind power: A review. *Emerging Research in Computing, Information, Communication and Applications*, pages 349–359.
- [Mittal et al., 2010] Mittal, R., Sandhu, K., and Jain, D. (2010). Battery energy storage system for variable speed driven pmsg for wind energy conversion system. In *2010 Joint International Conference on Power Electronics, Drives and Energy Systems & 2010 Power India*, pages 1–5. IEEE.
- [Noom, 2013] Noom, M. (2013). Theoretical analysis of mechanical power generation by pumping cycle kite power systems. *Master’s Thesis*.
- [Oehler and Schmehl, 2019] Oehler, J. and Schmehl, R. (2019). Aerodynamic characterization of a soft kite by in situ flow measurement. *Wind Energy Science*, 4(1):1–21.
- [Olabi et al., 2021] Olabi, A. G., Wilberforce, T., Elsaid, K., Sayed, E. T., Salameh, T., Abdelkareem, M. A., and Baroutaji, A. (2021). A review on failure modes of wind turbine components. *Energies*, 14(17):5241.
- [Orzan et al., 2022] Orzan, N., Leone, C., Mazzolini, A., Oyero, J., and Celani, A. (2022). Optimizing airborne wind energy with reinforcement learning. *arXiv preprint arXiv:2203.14271*.
- [Paiva and Fontes, 2017] Paiva, L. T. and Fontes, F. A. (2017). Optimal control of underwater kite power systems. In *2017 International conference in energy and sustainability in small developing economies (ES2DE)*, pages 1–6. IEEE.
- [Peçanha et al., 2020] Peçanha, L. B. C., Oliveira, N. d. S. B., and Bretas, W. V. (2020). Generation of wind energy with kites: a review of the airborne wind energy technology. In *2020 IEEE PES Transmission & Distribution Conference and Exhibition-Latin America (T&D LA)*, pages 1–6. IEEE.
- [Pereira and Sousa, 2022] Pereira, A. F. and Sousa, J. M. (2022). A review on crosswind airborne wind energy systems: Key factors for a design choice. *Energies*, 16(1):351.
- [Perumal, 2011] Perumal, L. (2011). Quaternion and its application in rotation using sets of regions. *International Journal of Engineering and Technology Innovation*, 1(1):35.
- [Reuchlin et al., 2023] Reuchlin, S., Joshi, R., and Schmehl, R. (2023). Sizing of hybrid power systems for off-grid applications using airborne wind energy. *Energies*, 16(10):4036.
- [Ruppert, 2012] Ruppert, M. B. (2012). *Development and validation of a real time pumping kite model*. PhD thesis, Delft University of Technology.
- [Rushdi et al., 2018] Rushdi, M., Yoshida, S., Dief, T. N., et al. (2018). Simulation of a tether of a kite power system using a lumped mass model. In *Proceedings*

- of *International Exchange and Innovation Conference on Engineering and Sciences (IEICES)*, pages 42–47. Interdisciplinary Graduate School of Engineering Sciences, Kyushu University.
- [Rushdi et al., 2020a] Rushdi, M. A., Dief, T. N., Yoshida, S., and Schmehl, R. (2020a). Towing test data set of the kyushu university kite system. *Data*, 5(3):69.
- [Rushdi et al., 2020b] Rushdi, M. A., Rushdi, A. A., Dief, T. N., Halawa, A. M., Yoshida, S., and Schmehl, R. (2020b). Power prediction of airborne wind energy systems using multivariate machine learning. *Energies*, 13(9):2367.
- [Saberri and Rezaie, 2022] Saberri, S. and Rezaie, B. (2022). Robust adaptive direct speed control of pmsg-based airborne wind energy system using fcs-mpc method. *ISA transactions*, 131:43–60.
- [Salari et al., 2015] Salari, M. E., Coleman, J., and Toal, D. (2015). Airborne wind energy—a review. In *3rd International Congress on Energy Efficiency and Energy Related Materials (ENEFM2015)*, page 81. Springer.
- [Salma et al., 2020] Salma, V., Friedl, F., and Schmehl, R. (2020). Improving reliability and safety of airborne wind energy systems. *Wind Energy*, 23(2):340–356.
- [Salma and Schmehl, 2023] Salma, V. and Schmehl, R. (2023). Operation approval for commercial airborne wind energy systems. *Energies*, 16(7):3264.
- [Schmehl et al., 2013] Schmehl, R., Noom, M., and Vlugt, R. v. d. (2013). Traction power generation with tethered wings. In *Airborne Wind Energy*, pages 23–45. Springer.
- [Schmidhuber et al., 1997] Schmidhuber, J., Hochreiter, S., et al. (1997). Long short-term memory. *Neural Comput*, 9(8):1735–1780.
- [Singla et al., 2020] Singla, M. K., Gupta, J., Nijhawan, P., Ganguli, S., and Rajest, S. S. (2020). Development of an efficient, cheap, and flexible iot-based wind turbine emulator. *Business Intelligence for Enterprise Internet of Things*, pages 225–231.
- [Spooner and Williamson, 1996] Spooner, E. and Williamson, A. (1996). Direct coupled, permanent magnet generators for wind turbine applications. *IEE Proceedings-Electric Power Applications*, 143(1):1–8.
- [Suman and Mathew, 2018] Suman, K. and Mathew, A. T. (2018). Speed control of permanent magnet synchronous motor drive system using pi, pid, smc and smc plus pid controller. In *2018 international conference on advances in computing, communications and informatics (ICACCI)*, pages 543–549. IEEE.
- [Terink et al., 2011] Terink, E., Breukels, J., Schmehl, R., and Ockels, W. (2011).

- Flight dynamics and stability of a tethered inflatable kiteplane. *Journal of Aircraft*, 48(2):503–513.
- [Thedens and Schmehl, 2023] Thedens, P. and Schmehl, R. (2023). An aerostuctural model for ram-air kite simulations. *Energies*, 16(6):2603.
- [Tulloch et al., 2023] Tulloch, O., Yue, H., Kazemi Amiri, A. M., and Read, R. (2023). A tensile rotary airborne wind energy system—modelling, analysis and improved design. *Energies*, 16(6):2610.
- [van der Vlugt et al., 2019] van der Vlugt, R., Bley, A., Noom, M., and Schmehl, R. (2019). Quasi-steady model of a pumping kite power system. *Renewable Energy*, 131:83–99.
- [Van Der Vlugt et al., 2013] Van Der Vlugt, R., Peschel, J., and Schmehl, R. (2013). Design and experimental characterization of a pumping kite power system. *Airborne wind energy*, pages 403–425.
- [von den Hoff et al., 2019] von den Hoff, D., Haberschusz, D., Rotering, N., and De Doncker, R. (2019). Design and evaluation of a battery-supported electric drivetrain for kite-based high-altitude wind energy conversion. In *2019 Conference for Wind Power Drives (CWD)*, pages 1–10. IEEE.
- [Wang, 2003] Wang, S.-C. (2003). Artificial neural network. In *Interdisciplinary computing in java programming*, pages 81–100. Springer.
- [Williams et al., 2008a] Williams, P., Lansdorp, B., and Ockels, W. (2008a). Non-linear control and estimation of a tethered kite in changing wind conditions. *Journal of guidance, control, and dynamics*, 31(3):793–799.
- [Williams et al., 2008b] Williams, P., Lansdorp, B., and Ockesl, W. (2008b). Optimal crosswind towing and power generation with tethered kites. *Journal of guidance, control, and dynamics*, 31(1):81–93.
- [Yan et al., 2013] Yan, J., Lin, H., Feng, Y., Guo, X., Huang, Y., and Zhu, Z. (2013). Improved sliding mode model reference adaptive system speed observer for fuzzy control of direct-drive permanent magnet synchronous generator wind power generation system. *IET Renewable Power Generation*, 7(1):28–35.
- [Zanon et al., 2013] Zanon, M., Gros, S., Andersson, J., and Diehl, M. (2013). Airborne wind energy based on dual airfoils. *IEEE Transactions on Control Systems Technology*, 21(4):1215–1222.
- [Zillmann and Bechtle, 2018] Zillmann, U. and Bechtle, P. (2018). Emergence and economic dimension of airborne wind energy. *Airborne wind energy: Advances in technology development and research*, pages 1–25.
- [Zolfaghari et al., 2020] Zolfaghari, M., Azarsina, F., and Kani, A. (2020). Feasibility analysis of airborne wind energy system (awes) pumping kite (pk). *Journal*

of Advanced Research in Fluid Mechanics and Thermal Sciences, 74(1):133–143.

Publications based on the thesis

Papers published in refereed journals

1. **Castelino, R. V.**, Kashyap, Y, and Kosmopoulos, P. “Airborne Kite Tether Force Estimation and Experimental Validation Using Analytical and Machine Learning Models for Coastal Regions.” *Remote Sensing*, 14(23): 6111, 2022.
<https://doi.org/10.3390/rs14236111>
2. **Castelino, R. V.**, Kashyap, Y. Et al. “Exploring the potential of kite-based wind power generation: an emulation-based approach.” *-under revision*
3. **Castelino, R. V.**, Kashyap, Y. Et al. “Design and Development of a Ground-based Kite Steer Controller for Kite-based Wind Power Generation.”” *-under review*

Papers published in conference proceedings

1. **Castelino, R. V.** and Kashyap, Y. Airborne Manoeuvre Tracking Device for Kite-based Wind Power Generation. *Control Applications in Modern Power System: Select Proceedings of EPREC 2020, Springer Singapore, 2021.*
https://doi.org/10.1007/978-981-15-8815-0_44

Patent publications

1. **System and Device for Swapping Battery in Kite Power Generation** -*Indian Patent Application No - 202341029597 – Filed - 24/04/2023, published - 26/05/2023*
2. **Ground-Based Power Kite Controller** -*Indian Patent Application No -202341017600 –Filed - 16/03/2023, published - 14/04/2023*
3. **Dynamic Kite Area-based Take-off and Landing Device for Power Kites ”** -*Indian Patent Application No - 202341014270 - Filed - 03/03/2023, published - 31/03/2023, First Examination Report - 05/06/2023*
4. **Kite Power Emulator** – *Indian Patent Application No – 202341039959, Filed - 12-06-2023*

Bio-Data

Name : Roystan Vijay Castelino
Date of birth: 25-05-1994
Marital status: single
E-mail: roystan.187ee007@nitk.edu.in
Mobile: +91-9844090375

Address:
Research Scholar
Department of Electrical and Electronics Engineering
National Institute of Technology Karnataka
Surathkal, Mangaluru, India-575025, India.

Education:

- **M.Tech.**, Power Electronics and Drives, National Institute of Technology Karnataka, Surathkal CGPA - 8.14, 2018.
- **B.Tech**, Electrical & Electronics Engineering, Srinivas Institute of Technology, Valachil, Mangaluru, Karnataka, Percentage - 74.48, 2015.

